

## Upper slope Site U1413<sup>1</sup>

R.N. Harris, A. Sakaguchi, K. Petronotis, A.T. Baxter, R. Berg, A. Burkett, D. Charpentier, J. Choi, P. Diz Ferreiro, M. Hamahashi, Y. Hashimoto, K. Heydolph, L. Jovane, M. Kastner, W. Kurz, S.O. Kutterolf, Y. Li, A. Malinverno, K.M. Martin, C. Millan, D.B. Nascimento, S. Saito, M.I. Sandoval Gutierrez, E.J. Screaton, C.E. Smith-Duque, E.A. Solomon, S.M. Straub, W. Tanikawa, M.E. Torres, H. Uchimura, P. Vannucchi, Y. Yamamoto, Q. Yan, and X. Zhao<sup>2</sup>

### Chapter contents

Background and objectives	1
Operations	1
Lithostratigraphy and petrology	2
Paleontology and biostratigraphy	5
Structural geology	6
Geochemistry	6
Physical properties	9
Paleomagnetism	10
Downhole logging	11
References	14
Figures	15
Tables	58

### Background and objectives

Integrated Ocean Drilling Program (IODP) Site U1413 (proposed Site CRIS-13B) targeted the upper slope of the Costa Rica margin, 30 km from the trench. This site is within the 3-D seismic data set along Line 2466 and crossing Line 4882 (Figs. F1, F2). Interplate earthquake relocations and interpretation of geodetic measurements show that this site is located above the seismogenic zone (S.L. Bilek, pers. comm., 2003; LaFemina et al., 2009).

The margin consists of slope sediment with a minimum thickness >1425 m. The primary purpose of drilling Site U1413 was to determine the nature, composition, and physical properties of the slope sediments. This site is also designed as a “pilot hole” in preparation for a proposed deeper CRISP Program B drilling. The location of this site represents a trade-off between being in the >500 m of water depth necessary for D/V *Chikyu* riser drilling and being over the seaward edge of the seismogenic zone so that drilling depths are a minimum. Additionally, it was important to locate the site within the 3-D seismic data volume.

In preparation for riser operations, engineering objectives included obtaining (1) shallow formation strength data for top hole design, (2) shear strength data to 100 meters below seafloor (mbsf), and (3) material for onshore geotechnical analysis.

Science objectives at Site U1413 included (1) documenting lithology and physical properties, (2) determining the stress orientation of the margin above the seismogenic zone, and (3) estimating the fluid-flow regime and role of slope sediment in fluid flow. Documenting periods of subsidence and uplift provides important information about the process of tectonic erosion that characterizes the Costa Rica margin. Stratigraphic correlation of multiple sites allows for estimating the relative motion of the margin.

### Operations

#### Transit to Site U1413

After a 15.0 nmi transit from Site U1412, the vessel stabilized over Site U1413 (proposed Site CRIS-13B) at 2330 h on 23 November 2012. The position reference used for dynamic positioning was a combination of GPS signals and an acoustic beacon, which was deployed at 2345 h on 23 November and retrieved at 0037 h on 1 December.

<sup>1</sup>Harris, R.N., Sakaguchi, A., Petronotis, K., Baxter, A.T., Berg, R., Burkett, A., Charpentier, D., Choi, J., Diz Ferreiro, P., Hamahashi, M., Hashimoto, Y., Heydolph, K., Jovane, L., Kastner, M., Kurz, W., Kutterolf, S.O., Li, Y., Malinverno, A., Martin, K.M., Millan, C., Nascimento, D.B., Saito, S., Sandoval Gutierrez, M.I., Screaton, E.J., Smith-Duque, C.E., Solomon, E.A., Straub, S.M., Tanikawa, W., Torres, M.E., Uchimura, H., Vannucchi, P., Yamamoto, Y., Yan, Q., and Zhao, X., 2013. Upper slope Site U1413. In Harris, R.N., Sakaguchi, A., Petronotis, K., and the Expedition 344 Scientists, *Proc. IODP*, 344: College Station, TX (Integrated Ocean Drilling Program).

doi:10.2204/iodp.proc.344.107.2013

<sup>2</sup>Expedition 344 Scientists' addresses.



### Hole U1413A

As soon as the vessel stabilized over the site coordinates, an advanced piston corer (APC)/extended core barrel (XCB) bottom-hole assembly (BHA) was assembled and lowered to just above the seafloor. Hole U1413A (8°44.4593'N, 84°6.8095'W; 540 m water depth) was spudded at 0635 h on 24 November 2012. Nonmagnetic core barrels and the FlexIT orientation tool were used for Cores 344-U1413-1H through 18H (Table T1). Advanced piston corer temperature tool (APCT-3) formation temperature measurements were taken with Cores 3H and 5H-8H. Coring continued through Core 18H at 140.6 mbsf with the APC system and through Core 26X at 189.1 mbsf with the XCB system. Because of the slow coring rate, the decision was made to pull out of the hole and change coring systems to the rotary core barrel (RCB) system. In Hole U1413A, 18 APC cores were taken over a 140.6 m interval with 143.6 m recovered (102%) and 8 XCB cores were taken over a 48.5 m interval with 43.7 m recovered (90%). Overall recovery for Hole U1413A was 187.3 m over the 189.1 m cored (99%). Hole U1413A ended when the bit cleared the seafloor at 2355 h on 25 November. Total time spent on Hole U1413A was 48.5 h.

### Hole U1413B

A shallow hole was cored for geochemical analyses. The vessel was offset 20 m east, and Hole U1413B (8°44.4593'N, 84°6.7992'W; 540 m water depth) was spudded at 0055 h on 26 November 2012. The seafloor depth was established at 540 m based on the mudline core recovery. Nonmagnetic core barrels were used, but orientation was not recorded. Three APC cores were taken over a 25.6 m interval with 27.4 m recovered (107%) (Table T1). The bit cleared the rotary table at 0550 h on 26 November, ending Hole U1413B. Total time spent on Hole U1413B was 5.75 h.

### Hole U1413C

After offsetting the vessel 20 m south, an RCB BHA with a new 9 $\frac{7}{8}$  inch bit was made up and run in the hole to just above the seafloor. Hole U1413C (8°44.4482'N, 84°6.7993'W; 540 m water depth) was spudded at 0940 h on 26 November 2012. The seafloor depth was assumed to be 540 m based on nearby Hole U1413B. Drilling without recovery continued for 11.75 h and reached a depth of 178.0 mbsf (Table T1). A nonmagnetic RCB core barrel was dropped, and coring began. Coring continued with Cores 344-U1413C-2R through 43R to a total depth of 582.2 mbsf, which was reached at 1300 h on 29 November. Coring was terminated to allow time to complete other expedition objectives. Forty-two RCB

cores were taken over a 404.2 m interval with 313.9 m recovered (78%).

In preparation for logging, the hole was swept clean with a 50 bbl high-viscosity mud sweep. A wiper trip was made from bottom to 88.4 mbsf. On the way back into the hole, we ran into an obstruction at 250.6 mbsf. The hole had to be washed and reamed down to the total depth of 582.2 mbsf. Another 30 bbl high-viscosity mud sweep was pumped, followed by a 50 bbl sweep. The RCB bit was released at 572.2 mbsf, and the hole was displaced with heavy mud. The drill string was pulled out of the hole so that the end of the pipe was set at 103 mbsf. Because hole conditions were poor, the decision was made not to run the nuclear source on the first logging run. The logging tools were rigged up, and the triple combination (triple combo) tool string was run into the hole at 1200 h, reaching 181.9 mbsf. The next logging run was with the Ultrasonic Borehole Imager (UBI) tool string. This run started at 1600 h and reached 189.9 mbsf. The final logging run was with the Formation MicroScanner (FMS) tool string. The run started at 1955 h and also reached 189.9 mbsf. The logging tools were rigged down, and the rig floor was secured for transit back to Site U1412 at 0145 h on 1 December. Total time spent on Hole U1413C was 116 h. Total time spent on Site U1413 was 170.25 h or 7.1 days.

## Lithostratigraphy and petrology

Site U1413 was drilled to investigate the lithostratigraphy and structural geology of the upper slope sequence as a preliminary study for future deep riser drilling. Three holes were drilled to recover sediment and sedimentary rocks. From the seafloor to 578.84 mbsf, sediment was drilled with the APC (0–140.60 mbsf; Cores 344-U1413A-1H through 18H and 344-U1413B-1H through 3H), the XCB (140.60–186.91 mbsf; Cores 344-U1413A-19X through 26X), and the RCB (0–578.84 mbsf; Cores 344-U1413C-1R through 43R). Core recovery was excellent for Holes U1413A and U1413B, with 99% and 107% average recovery, respectively. Good recovery was achieved for Hole U1413C, with 78% recovered. Hole U1413B was drilled primarily to determine chemical pore water gradients in the uppermost sediment.

Three lithostratigraphic units were distinguished in the sediment at this site, with an overall abundance of silty clay to clay (32.1%), clayey silt to sandy silt (53.3%), silty sand to sand (14.4%), and tephra (0.2%). Unit I, recovered in Holes U1413A and U1413B, is 44.60 m thick and is dominated by dark greenish gray silty clay with multiple centimeter-sized turbidite sequences of fine-sand laminae. A

slump/slide event was identified in the uppermost ~3.5 m of this unit. The lithology changes into a brownish green chaotic mixture of silty clay and dark gray sand in the lowermost part of Core 344-U1413A-5H. Ten tephra layers were identified throughout Unit I. Lithostratigraphic Unit II, starting at 44.60 mbsf, is characterized by a well-consolidated light greenish gray calcareous clayey silt(stone) with occasional variations to silty clay and minor sand(stone) layers. Unit II exhibits moderate variability in the amount and extent of calcareous cementation with depth. In addition, this unit contains several horizons of lithified and reworked rounded carbonate mud clasts. Fourteen tephra layers were identified in Unit II. Near the bottom of Hole U1413A (Section 344-U1413A-20X-1), a chaotic layer of intermixed sand and calcareous clayey silt, not associated with a lithology change, most likely represents an interval composed of mass transport deposits (MTDs). Unit II continues in Hole U1413C to 366.45 mbsf with the same lithology, but heavy minerals, shell fragments, and occasional sandstone layers with sapropel and leaf fragments become more abundant with depth. The boundary between Units II and III (Section 344-U1413C-21R-3, 117 cm) is conspicuous because of the first appearance of an 18 m thick package of alternating sandstone and siltstone with common to abundant organic matter (sapropel), shell, and gastropod fragments. The matrix of the silt- and sandstone is characterized by abundant magmatic and sedimentary lithic fragments, common feldspar, and volcanic glass fragments. Foraminifers are the most abundant component of the biogenic material. After a relatively thin siltstone interval (~42 m), the remainder of the hole (426.83–578.84 mbsf) consists of massive fine- to medium-grained sandstones that contain three tephra layers. The sandstones are normally graded and range from decimeter- to meter-thick layers with occasional internal laminations, particularly in the uppermost part of the section. Some cores in Unit III are particularly rich in gastropods and reworked, well-rounded carbonate clasts. Lithostratigraphic units at Site U1413 can be well correlated to some of the units found at Sites U1378 and U1379 during Expedition 334.

### Description of units

Cores recovered at Site U1413 were divided into three lithostratigraphic units (Fig. F3; Table T2).

#### Unit I (Holes U1413A and U1413B)

Interval: Sections 344-U1413A-1H-1 to 6H-1, 0 cm, and 344-U1413B-1H-1 to 3H-CC, 27 cm

Thickness: 44.60 m

Depth: 0–44.60 mbsf

Age: late Pleistocene to Holocene

Lithology: silty clay with centimeter-sized normally graded fine sand

Unit I is 44.60 m thick and consists mainly of dark greenish gray soft silty clay. The clay is punctuated by a series of several centimeter-thick, turbiditic fining-upward sequences with millimeter-thick laminae, as well as 10 white to pinkish gray and dark gray clayey tephra layers (Fig. F4). The turbiditic fine-grained sand has sharp lower contacts, characterized by laminae composed of well-rounded sand grains that grade into the background sediment at the top. Tephra layers range in thickness from 1 to 15 cm and commonly are extremely fine grained with a clayey appearance. Only a few tephra layers exhibit sharp lower and gradational upper contacts.

The main components of Unit I are terrigenous and dominated by clay. Smear slide analyses indicate that feldspar and lithic (sedimentary and magmatic) fragments are the most abundant accessory grains. Additional components include chert, opaque minerals, volcanic glass fragments, amphiboles, and rare pyroxene. Biogenic components such as nanofossils, foraminifers, and diatoms are rare.

The two MTDs identified in Unit I are characterized by intermixed silty clay with sand, abrupt color change, lithology, and consolidation relative to the underlying undisturbed sediment. The first MTD is identified by color change and chaotic mixing and occurs in Sections 344-U1413A-1H-3, 34 cm, and 344-U1413B-1H-3, 34 cm (at 3.34 mbsf in both) (Fig. F5). Evidence for this MTD also appears in the pore water chemistry profiles (see “Geochemistry”). The second MTD in the lowermost part of Section 344-U1413A-5H-7 is identified by a gradational brownish green chaotic mixture of silty clay and dark gray sand (Fig. F6) before an abrupt change at 44.60 mbsf that marks the lithologic transition into Unit II.

#### Unit II (Holes U1413A and U1413C)

Intervals: Sections 344-U1413A-6H-1, 0 cm, to 26X-CC, 14 cm, and 344-U1413C-2R-1, 0 cm, to 21R-3, 117 cm

Thickness: 321.85 m

Depth: 44.60–366.45 mbsf

Age: mid- to late Pleistocene

Lithology: calcareous clayey silt(stone) and minor sand(stone)

Unit II is dominated by light greenish gray calcareous clayey silt(stone), with smaller variations in grain size to silty clay(stone) and minor sand(stone) layers. The sediment is well consolidated to lithified in the lower part of the unit and contains 14 tephra layers that remain unlithified down to 188 mbsf

(Section 344-U1413C-3R-1) (Fig. F7). The lithology of Unit II shows variable amounts of calcareous cementation, as well as occasional horizons where lithified and reworked rounded carbonate mud clasts are common.

In general, Unit II is massive, with minor changes in the proportions of clay, silt, and sand. Grain sizes and abundances gradually change over several meter-long intervals. Sandstone layers become more abundant toward the base of the unit and contain increasing amounts of organic matter (sapropel and leaf fragments) and shell fragments.

Framboidal pyrite was observed macroscopically and in many smear slides from Unit II. Bimodal distribution in organic material is evident by the sparse presence of shell fragments, diatoms, and nanofossils throughout the unit, whereas foraminifers are a major constituent of the sand-sized fraction of the sediment. The main component of Unit II is terrigenous clay. Smear slides indicate that the most abundant accessory grains in the silt(stone) and clay(stone) include feldspar and lithic (sedimentary and magmatic) fragments. Components present only in trace abundances include amphibole, calcite, biotite, chlorite, and glass shards.

A horizon of chaotically mixed sand and calcareous clayey silt near the bottom of Hole U1413A at 151 mbsf (Section 344-U1413A-20X-1) is not associated with a lithologic boundary but instead may represent an MTD interface (see “[Paleontology and biostratigraphy](#),” “[Geochemistry](#),” and “[Physical properties](#)”).

### Unit III (Hole U1413C)

Interval: Sections 344-U1413C-21R-3, 117 cm, to 43R-CC, 20 cm

Thickness: 212.39 m

Depth: 366.45–578.84 mbsf

Age: early to mid-Pleistocene

Lithology: fine- to medium-grained sandstone and siltstone

Unit III consists of olive-green, meter-scale silty sand and sandstone sequences with erosive lower contacts. The two packages of predominantly sandy deposits are separated by a ~42 m thick siltstone sequence and represent ~80% of the total unit thickness. The two sandy intervals are between 366.45 and 384.61 mbsf (interval 344-U1413C-21R-3, 117 cm, to 23R-3, 9 cm) and between 426.83 and 578.84 mbsf (interval 27R-5, 55 cm, to 43R-CC, 20 cm).

The sandstone to conglomerate beds are mostly decimeter thick but can reach up to a meter in thickness and are normally graded (Fig. F8). Relatively large shell fragments (as much as 2 cm in diameter) and

millimeter- to centimeter-sized, well-rounded to sub-rounded sedimentary lithic clasts make up the coarser fractions of the sandstone and the matrix-supported conglomerates (Fig. F9). Rip-up clasts, millimeter-scale laminations at the top of the fining-upward sequences, and chaotic mixing are also observed throughout the coarser sequences.

Tephra layers are rare in this unit, with only three horizons found within the upper part of Unit III. Framboidal pyrite occurs throughout the unit. Bioturbation is variable throughout the unit but generally decreases with depth. Foraminifers, shells, and shell fragments are conspicuous within the sandstone, along with disseminated sapropel and plant debris that is also recognized throughout the coarser horizons (Figs. F9, F10) of Unit III.

Smear slide observations indicate that the sandstone is dominated by terrigenous lithic clasts that are primarily composed of magmatic rock fragments and feldspar minerals. Glauconite commonly appears in discrete enriched horizons (Fig. F11). Chlorite is the most abundant accessory mineral, followed by volcanic glass, opaque minerals, and amphibole. Trace components include calcite, pyroxene, and quartz. Biogenic components observed from smear slides are rare but include nanofossils and diatoms and foraminifer fragments.

### X-ray diffraction analyses

Preliminary X-ray diffraction analyses of Site U1413 sediment suggest that there is little compositional variation in lithostratigraphic Units I–III. X-ray diffractograms indicate that the major mineral components are phyllosilicates, including smectite and chlorite, as well as plagioclase, quartz, and calcite (Fig. F12).

Zeolites are ubiquitous in Unit I as heulandite and laumontite, but in Unit II, the peak intensity of laumontite decreases, whereas the peak intensity of heulandite increases. The only zeolite present in Unit III is heulandite. Amphibole (hornblende) and analcime peaks are also recognized in Unit I, Unit II, and, at a weaker intensity, in the shallower part of Unit III. Pyrite peaks are present in all units.

### Depositional environment and correlation to Sites U1379 and U1378 (Expedition 334)

The cover sequence recovered from Site U1413 is a terrestrially sourced upper slope sequence consistent with high sediment accumulation rates throughout the depositional interval (see “[Paleontology and biostratigraphy](#)”). Recognition of organic debris and thin (<5 cm) normally graded sand beds with sharp erosional bases within Unit I of Holes U1413A

and U1413B is consistent with depositional features of a distal clastic turbidite facies and correlates well with Hole U1378B. The clay-rich deposits of Unit II at Site U1413 are probably lithostratigraphically similar to those observed in Unit II in Hole U1379C but lack the carbonate-rich Subunit IIB. A large proportion of the sandy Subunit IIC at Site U1379 was not recovered at Site U1413. Finally, Unit III of Site U1413 can also be well correlated with Unit III of Site U1379. In summary, our observations indicate that the drilled interval at Site U1413 is a condensed section of Site U1379.

## Paleontology and biostratigraphy

We examined the microfossil content of core catcher samples from Holes U1413A–U1413C. Biostratigraphy was primarily based on calcareous nannofossils, except for the uppermost section of Hole U1413A, where radiolarians were present. Benthic foraminifers were used to characterize the paleoenvironmental changes at this site.

### Calcareous nannofossils

Calcareous nannofossil abundance and preservation varied from common and good in Hole U1413A to rare and moderate in Hole U1413C. Samples 344-U1413A-1H-CC through 14H-CC are assigned to Zone NN21, based on the presence of *Emiliania huxleyi*. For Samples 344-U1413A-15H-CC through 19X-CC, the age is less well constrained and is assigned to Zones NN20–NN21 (1.89 Ma to present). The first appearance of *Pseudoemiliania lacunosa*, which defines the top of Zone NN19, is found in Sample 344-U1413A-20X-CC.

Nannofossil assemblages from the top of Hole U1413C overlap with those from the base of Hole U1413A and are assigned to Zone NN19. The last occurrence (LO) of *Helicosphaera sellii* is observed in Sample 344-U1413C-15R-CC (Table T3). Raffi et al. (2006) assigned this event to 1.34 Ma, although this biohorizon has a moderate to low degree of reliability. Sedimentation rates for this horizon were calculated using the lower limit of Zone NN19 (1.89 Ma), the LO of *H. sellii* (1.34 Ma), and the first occurrence of *P. lacunosa* (0.44 Ma). The sediment accumulation rate of the uppermost interval (Cores 344-U1413A-20X through 344-U1413C-14R, with a thickness of 149.67 m) is estimated to be 166 m/m.y., although this estimate is preliminary and should be considered conservative.

For the lower interval, between Samples 344-U1413C-15R-CC and 43R-CC (a thickness of ~274.74 m) the

estimated sediment accumulation rate is 590 m/m.y. The average sediment accumulation rate from Sample 344-U1413A-20X-CC to the bottom of the hole is 383 m/m.y.

### Radiolarians

The abundance of radiolarians at Site U1413 varied between few in the upper sections of Hole U1413A (Samples 344-U1413A-1H-CC through 10H-CC) (Table T4) to rare and barren at the bottom of Hole U1413A and the top of Hole U1413C. Preservation ranged from moderate to poor. Spicules were more abundant than radiolarians but were also characterized as few.

Biostratigraphic markers were not abundant in the upper sections of Hole U1413A, with only a few species present, including *Anthocyrtidium ophirensis*, *Acrosphaera trepanata*, and *Sphaerozoum punctatum* aff. The presence of *S. punctatum* aff. in Samples 344-U1413A-2H-CC and 3H-CC can be used to refine this age to <0.2 Ma (Goll, 1980). However, the definitive taxonomic assignment of this species will be confirmed by scanning electron microscopy.

### Benthic foraminifers

Benthic foraminifers were observed in 48 core catcher samples (25 from Hole U1413A and 23 from Hole U1413C). An additional sample was taken from interval 344-U1413A-1H-1W, 115–124 cm (Table T5; Fig. F13).

Benthic foraminifer abundances and preservation are dominant and good in Samples 344-U1413A-1H-1W through 19X-CC. However, they range from common to few in the lower part of Hole U1413A (Samples 344-U1413A-20X-CC through 25X-CC) and throughout Hole U1413C, with preservation decreasing from good to moderate. Most of the foraminifer samples show signs of mechanical breakage.

Planktonic benthic ratios display large ranges that generally decrease downhole (Table T5). Benthic foraminifer assemblage changes downhole are remarkable for the presence of only some species in particular intervals. *Brizalina bicostata*, *Cassidulina tumida*, *Cancris inflatus*, and *Uvigerina* cf. *juncea* are only present in the uppermost 149 m of sediment (between Samples 344-U1413A-1H-1W and 19X-CC). Other species such as *Brizalina spissa*, *Epistominella smithi*, *Uvigerina* cf. *excellens*, and *Hansenisca altiformis* characterize the assemblages between 160 mbsf (Sample 344-U1413A-20X-CC) and 478 mbsf (Sample 344-U1413C-32X-CC). Further downhole (Samples 344-U1413C-36R-CC through 42R-CC), another substantial change in the benthic assemblages is marked by the appearance of *Brizalina* cf. *dilatata*.

Two intervals are characterized by the dominance (>40%) of a few species of benthic foraminifers. The first interval, between Samples 344-U1413A-13H-CC and 19X-CC, is dominated by *B. bicostata* and *U. cf. juncea*, comprising 70%–90% of the benthic foraminifer assemblage. The second interval is at the bottom of Hole U1413C (between Samples 344-U1413C-32R-CC and 42R-CC) and is characterized by large relative abundances of *Uvigerina peregrina* and *B. cf. dilatata*, which comprise 70%–90% of the assemblage. The high abundance and dominance of these species is rather unusual in the fossil record.

## Structural geology

Site U1413 is located on the upper slope of the Costa Rica forearc, offshore Osa Peninsula. Hole U1413A was drilled to a depth of 189.1 mbsf. Hole U1413B was drilled to a depth of 25.6 mbsf and was devoted to geochemistry sampling. Hole U1413C has a total depth of 582.2 mbsf, with a cored interval of 404.2 m.

We divided the entire section into two structural domains (Figs. F14, F15): (1) Domain I, from 0 to 180 mbsf, is characterized by subhorizontal to gently northeast-dipping bedding with few fault structures, and (2) Domain II, from 180 to 582.2 mbsf, shows an increase of bedding dip angles and abundance of fault structures with depth. In Domain II, the few measurements that were oriented to the geographic coordinates show a general northeast-dipping attitude.

Faulting-related deformation is abundant from ~180 mbsf to the bottom of the drilled section (Fig. F14). Normal faulting is more abundant than reverse faulting. Dip angles of normal faults and reverse faults vary from subhorizontal to subvertical with some dips >75°. The frequency of normal and reverse faults varies along the entire hole. Bedding planes are more abundant in intervals of less pronounced faulting. The deeper parts of Hole U1413C, starting with Core 344-U1413C-21R, are characterized by high-angle reverse faults with unusually steep dip angles >75° (Fig. F16). Because of these unusually high dip angles of reverse faults and the variation in fault frequency related to depth (especially the reverse faults), selected cores were double-checked for consistency. Structural data on faults were then ranked in terms of reliability as A (reliable) or B (less reliable) (see the structural data set in STRUCTURE in “Supplementary material”). B-faults comprise ~25% of the checked structures.

The measurements oriented in true geographic coordinates show a complex distribution that is indicative of multiple fault sets (Fig. F17). Future spatial analysis on faults will be carried out on the B-faults to further determine their reliability.

Brittle shear deformation is localized along brecciated fault zones at 181, 230, 237–239, 365, 529–532, and 567 mbsf.

## Geochemistry

### Inorganic geochemistry

We collected 30 APC whole-round samples (12–24 cm long) and 9 XCB whole-round samples (25–36 cm) from Hole U1413A at a frequency of two samples per core through Core 344-U1413A-13H and one to two samples per core in the rest of the hole. Most XCB cores were of high enough quality for interstitial water processing. Hole U1413B consisted of only three APC cores, devoted to high-resolution biogeochemical processes studies at and in the vicinity of the sulfate–methane transition zone (SMTZ). A total of 26 whole-round samples (5–10 cm) were collected on the catwalk in the three cores from Hole U1413B: five samples from Core 344-U1413B-1H, twelve from Core 2H, and nine from Core 3H. All samples from Hole U1413B were processed in a glove bag under a nitrogen atmosphere. Real-time sulfate concentration analyses were used to accurately delineate the SMTZ depth at 16 mbsf. A 2 cm slice from each of the cleaned interstitial water sediment samples was collected for shore-based microbiological analyses in Hole U1413A to ~100 mbsf and in Hole U1413B. These microbiological samples were vacuum-sealed and stored at –80°C. In Hole U1413C, we collected 41 (30–32 cm long) whole-round samples at a frequency of one to two per core.

All samples were thoroughly cleaned for drill water contamination. The cleaned samples from all three holes were placed in Ti squeezers and squeezed at gauge forces of <30,000 lb. The inner diameter of the Ti squeezers is 9 cm; thus, the maximum squeezing pressure was 3043 psi (~21 MPa). The pore fluid was collected in syringes and passed through a 0.2 μm filter prior to analysis. The volume of pore fluid recovered varied with lithology and coring technique: 31–72 mL from the APC samples, 11–38 mL from the XCB samples, and 5.5–34 mL from the RCB samples. Specific aliquots of pore fluids were used for ship-board analyses, and the remaining fluid was sampled for shore-based analyses (see “Geochemistry” in the “Methods” chapter [Harris et al., 2013]). One sample from Section 344-U1413C-15R-1 was collected for shore-based He isotope ratio analysis.

Samples recovered from below the SMTZ should not contain sulfate. We used the sulfate concentrations reported in Table T6 as a tracer for drilling contamination with surface seawater and corrected the pore fluid concentrations in Hole U1413A and U1413C samples, as described in “Geochemistry” in the “Methods” chapter (Harris et al., 2013).

The uncorrected data for the major element concentrations are listed in Table T6, and in Table T7 we list the sulfate-corrected concentration data. Table T8 lists the uncorrected minor element concentrations, and Table T9 presents the sulfate-corrected data. Figures F18, F19, F20, and F21 illustrate only the sulfate-corrected data.

### Salinity, chloride, and alkalis (sodium and potassium)

Downhole profiles of salinity, chloride, potassium, and sodium from Site U1413 are shown in Figure F18. Salinity values slightly decrease with depth from a seawater value at the seafloor to ~32.5 below the SMTZ at ~16 mbsf. Between the SMTZ and ~150 mbsf, which corresponds to a probable MTD (see “[Lithostratigraphy and petrology](#)”), salinity values range from 32.5 to 33.0. Below 150 mbsf, salinity slightly decreases to ~30 at ~200 mbsf and remains constant at ~30 to the bottom of Hole U1413C. The drop of ~1.5 salinity units below the SMTZ is most likely related to authigenic carbonate precipitation in the vicinity of this transition zone. At this site, Cl concentrations are on average lower than modern seawater by 3–10 mM. Cl concentrations increase with depth to ~150 mbsf, where an MTD is observed (see “[Lithostratigraphy and petrology](#)”). Interestingly, the Cl concentration at this depth is that of modern seawater, 559 mM. From ~150 to ~500 mbsf, Cl concentrations decrease, with minimum concentrations of 522–526 mM observed at 475–510 mbsf, suggesting minor lateral fluid flow of fresher fluid in the more sandy section in lithostratigraphic Unit III (see “[Lithostratigraphy and petrology](#)”). Slightly elevated Li concentrations (Fig. F21) support the interpretation of slightly fresher and Li-rich fluid flow from a higher temperature source; the in situ temperature is only ~32°C. This observation is especially intriguing because a similar decrease in Cl concentrations and a corresponding increase in Li concentrations were observed at Site U1379, ~100 m deeper in the sediment section.

The cause for lower than modern seawater Cl values (98.5%–99% modern seawater Cl) in the uppermost ~150 m, where several MTDs were observed, is unclear.

Sodium concentrations decrease with depth from about the seawater value of 480 mM at ~3 mbsf to 435–440 mM at 45 mbsf, the depth of the lithostratigraphic Unit I/II boundary (see “[Lithostratigraphy and petrology](#)”). The decrease in sodium may be driven by volcanic tephra alteration to zeolites; in this depth interval, Cl concentrations do not increase. Below this depth, sodium concentrations remain approximately constant, varying between 445 and 460 mM to the bottom of Hole U1413C.

Similar to the other Expedition 344 drill sites, at and below the seawater/sediment interface, K concentrations are slightly higher by 1–2 mM than the modern seawater value of 10.4 mM. This elevated concentration most likely relates to clay ion exchange reactions. K concentrations gradually decrease from the seafloor and reach ~8.5 mM (Fig. F18) at the base of Unit I (see “[Lithostratigraphy and petrology](#)”); this decrease may be caused by volcanic tephra alteration to clays. The decrease in K concentrations steepens in the lowermost 80 m of Hole U1413A and reaches a minimum of ~7 mM. Deeper in Hole U1413C, K concentrations are approximately constant to ~380 mbsf in lithostratigraphic Unit II (see “[Lithostratigraphy and petrology](#)”). Below 380 mbsf, K concentrations slightly decrease to a minimum of ~5 mM (~50% modern seawater value) at the bottom of this site. The uptake of K may be related to zeolite formation and/or to smectite/illite transformation at greater depth.

### Alkalinity, sulfate, ammonium, calcium, and magnesium

Sulfate, alkalinity, and ammonium (Figs. F19, F20) have characteristic organic matter remineralization concentration-depth profiles in the uppermost ~150 m, which are impacted by MTDs at ~45 and ~150 mbsf (see “[Lithostratigraphy and petrology](#)”). Sulfate concentrations decrease from ~26 mM to zero between the seafloor and the SMTZ at 16 mbsf. Alkalinity increases from seawater value at the seafloor to a maximum of ~36 mM at ~42 mbsf. Below the MTD at ~45 mbsf, concentrations gradually decrease to ~27 mM at 68 mbsf, increase again to ~34 mM at 92 mbsf, and following this secondary maxima, alkalinity steadily decreases to a minimum of 2.7 mM at the bottom of Hole U1413C. Alkalinity is involved in carbonate diagenesis in the upper ~150 m, as suggested by the concomitant decrease in Ca and Mg concentrations. Similar to alkalinity, ammonium concentrations increase steeply from the seafloor, where concentrations are zero, to a maximum of ~8 mM just above the first slump at ~45 mbsf. Below this MTD, concentrations first increase and then decrease slightly to ~4.7 mM at the MTD at ~151 mbsf (see “[Lithostratigraphy and petrology](#)”). After increasing to 7 mM at ~200 mbsf, concentrations decrease to the bottom of Hole U1413C, as in typical ammonium concentration-depth profiles.

High-resolution sulfate, alkalinity, and methane data from the uppermost 30 m of Site U1413 are shown in Figure F19. The SMTZ is clearly observed at 16 mbsf; at this depth, alkalinity reaches a maximum of 26.4 mM. Below the SMTZ, alkalinity slightly decreases to 23 mM and then increases with depth. Sulfate has an atypical concentration-depth profile that suggests

another small MTD in the uppermost 8–10 m; this is also supported by the alkalinity depth profile.

Ca and Mg concentrations decrease from seawater values at the seafloor to minima of 1.1 and 39.8 mM, respectively, at the lithostratigraphic Unit I/II boundary, where an MTD is observed (see “[Lithostratigraphy and petrology](#)”). This pattern reflects precipitation of authigenic carbonates. There are marked increases in Ca concentrations below this depth, in particular below the second MTD at ~150 mbsf to the bottom of Hole U1413C, where Ca concentration is ~15 mM (~50% higher than modern seawater value). Mg concentrations increase below the first and second MTDs, most likely driven by clay ion exchange with ammonium. However, below ~150 mbsf, the Mg concentration-depth profile is a mirror image of the Ca profile. Mg concentration at the bottom of Hole U1413C is ~19 mM (~53% seawater value). The inverse concentration-depth profiles of Ca and Mg in Hole U1413C suggest diffusional interaction with a higher temperature reaction zone at depth.

### Strontium, lithium, manganese, boron, silica, and barium

Downhole distributions of Sr, Li, Mn, B, Si, and Ba are shown in Figure [F21](#). Sr concentrations decrease steeply from seawater concentration at ~3 mbsf to ~60  $\mu\text{M}$  at the SMTZ (16 mbsf), indicating diagenetic carbonate precipitation. From the SMTZ to ~150 mbsf, Sr concentrations remain low, with values between 41 and 60  $\mu\text{M}$ . This depth interval is associated with high alkalinity and carbonate diagenesis. Below ~200 mbsf, Sr concentrations slightly increase to a maximum of ~75  $\mu\text{M}$ . Several diagenetic reactions may be responsible for this slight increase in Sr concentrations. However, it is difficult to uniquely identify the controlling reaction based on the data available.

Li concentrations rapidly decrease from the seafloor to ~10  $\mu\text{M}$  just below the SMTZ and fluctuate between 10 and 16  $\mu\text{M}$  to the large slump at ~150 mbsf. Li values increase irregularly with depth and peak at ~80  $\mu\text{M}$  below ~400 mbsf in lithostratigraphic Unit III (see “[Lithostratigraphy and petrology](#)”) (Fig. [F21](#)). This unit is somewhat sandier, and the increase in Li and decrease in Cl concentrations within this zone may indicate transport of slightly fresher fluid originating at a higher temperature. However, besides Li and Cl concentrations, other solute concentration profiles do not indicate that the lower sandier lithostratigraphic Unit III acts as a fluid conduit. Below this depth to the bottom of the Hole U1413C, Li concentrations decrease to a minimum value of ~54  $\mu\text{M}$ . Mn concentrations are very low, mostly below 4  $\mu\text{M}$ , throughout the section cored.

B concentrations are slightly higher than the bottom seawater value of ~450 nM in the shallowmost samples and steadily decrease in lithostratigraphic Unit I to ~140  $\mu\text{M}$  at the 150 mbsf MTD. From ~180 mbsf, B concentrations vary and decrease slightly. In lithostratigraphic Unit III (below ~360 mbsf), concentrations fluctuate between 90 and 110  $\mu\text{M}$  (Fig. [F21](#)). These lower B concentrations may be either lithologically or diagenetically controlled.

In the uppermost ~40 m, above the first slump (see “[Lithostratigraphy and petrology](#)”), Si concentrations are above bottom water concentrations and vary between 300 and 500  $\mu\text{M}$ . Below this depth, Si concentrations decrease sharply in the upper ~150 m and then more gradually to a minimum of 65  $\mu\text{M}$  at the bottom of Hole U1413C (Fig. [F21](#)).

Dissolved Ba concentrations are extremely low in the uppermost ~150 m. They increase in Hole U1413C and are variable, ranging between 1 and 5  $\mu\text{M}$ . The concentration maxima at ~300 and 450 mbsf may reflect paleoredox boundaries.

### Organic geochemistry

The organic geochemistry data for Site U1413 are listed in Tables [T10](#) and [T11](#) and plotted in Figures [F22](#) and [F23](#). In the headspace gases, methane concentrations range from 3 to 42,600 ppmv, ethane concentrations are 0.4 to 106 ppmv, and propane concentrations do not exceed 24.1 ppmv.  $\text{C}_{4+}$  was detected below 290 mbsf. *N*-butane concentrations range between 0.8 and 9.3 ppmv, and *iso*-pentane values range from 0.7 to 8.4 ppmv. In the void gases, methane concentrations range from 792,000 to 841,000 ppmv, ethane concentrations range between 4 and 11 ppmv, and propane concentrations are below 8 ppmv.

In general, methane concentrations increase rapidly below 15.5 mbsf, consistent with the depth of the SMTZ at this site (Fig. [F19](#)). From the top of the sediment section to 333 mbsf, headspace and void gas compositions indicate a biogenic hydrocarbon source. Below 333 mbsf, profiles of  $\text{C}_2$  to  $\text{C}_5$  and  $\text{C}_1/\text{C}_{2+}$  ratios of headspace gas as low as ~25 indicate the presence of thermogenic gases. The geothermal gradient at Site U1413 is 40°C/km (see “[Physical properties](#)”); thus, the temperature between 350 mbsf and the bottom of the cored section ranges from 25° to 33°C. This temperature range is too low for in situ production of thermogenic hydrocarbons, suggesting that the gases sampled here migrated from deeper, warmer sediments. This inference will be confirmed by isotopic analyses of the gases postexpedition.

Organic and inorganic carbon distributions are illustrated in Figure [F24](#), and the data are listed in

Table T12. Inorganic carbon fluctuates from ~0.6 to <1.6 wt%, and CaCO<sub>3</sub> ranges from 5.2 to 13.5 wt%. Total nitrogen concentrations do not exceed 0.2 wt%. The total carbon and total organic carbon concentrations in lithostratigraphic Unit II decrease slightly to ~1.5 and ~0.5 wt%, respectively. The calculated C/N ratio is ~10 throughout lithostratigraphic Unit I, and the C/N ratio decreases from 14.9 to 4.9 in lithostratigraphic Unit II, though with high data scatter. The organic carbon source and degree of degradation will be further characterized postcruise through carbon, hydrogen, and nitrogen isotopic ratio analyses.

## Physical properties

At Site U1413, physical properties measurements were made to help characterize lithostratigraphic units. After sediment cores reached thermal equilibrium with ambient temperature at ~20°C, gamma ray attenuation (GRA) density, magnetic susceptibility, and *P*-wave velocity were measured using the Whole-Round Multisensor Logger (WRMSL). After WRMSL scanning, the whole-round sections were logged for natural gamma radiation (NGR). For soft-sediment cores, thermal conductivity was measured using the full-space method prior to core splitting. Following core splitting, color reflectance and magnetic susceptibility were measured on the archive-half cores using the Section Half Multisensor Logger (SHMSL). Moisture and density were measured on discrete samples collected from the working halves of the split sediment cores, generally once per section. For indurated sediments, thermal conductivity was measured on the split cores using the half space method. *P*-wave velocity and strength were measured on the working halves of split cores. Physical properties data are compared to Site U1379, which was drilled during Expedition 334 and is located 11 km from Site U1413 (Expedition 334 Scientists, 2012).

### Density and porosity

Bulk density values at Site U1413 were determined from both GRA measurements on whole-round cores and mass/volume measurements on discrete samples from the working halves of split cores (see “[Physical properties](#)” in the “Methods” chapter [Harris et al., 2013]). In general, wet bulk density values determined from discrete samples agree with the whole-round GRA measurements for APC cores (0–140.6 mbsf) and are higher than the whole-round GRA measurements for XCB and RCB cores (>140.6 mbsf) (Figs. F25, F26). Grain density measurements were determined from mass/volume measurements on dry discrete samples within the sedimentary sequence (Fig. F26).

Site U1413 grain density values average 2.72 g/cm<sup>3</sup> and are similar to those from Site U1379 in the upper 150 m. From 150 to 450 mbsf, grain density values exceed those of Site U1379 for similar depths; below 450 mbsf, they are similar to the highest grain densities observed at Site U1379. Between 0 and 180 mbsf, Site U1413 porosity values decrease rapidly from 70% to 50% and more gradually below 180 mbsf to 40% at the bottom of Site U1413. Both trends observed in Site U1413 data have different slopes than those found in porosity data from Site U1379.

### Magnetic susceptibility

Volumetric magnetic susceptibilities were measured using the WRMSL, and point measurements were made on the SHMSL for all core sections longer than ~20 cm (Fig. F27). Magnetic susceptibility values are reported in instrument units (IU). Values measured by these two instruments are in good agreement. Magnetic susceptibility values vary from <20 to ~230 IU in Unit I and from <20 to ~520 IU in Unit II above 200 mbsf. The background value from the seafloor to ~200 mbsf is ~25 IU. Unlike other sites, where magnetic susceptibility excursions are often associated with tephra layers, peaks at Site U1413 appear to coincide with sand-rich layers that contain detrital magnetite (see “[Lithostratigraphy and petrology](#)”). In the lower portion of Unit II (200 to ~366 mbsf), magnetic susceptibility remains generally between ~20 and ~50 IU throughout, with few high excursions. Magnetic susceptibility in Unit III is slightly higher and slightly more variable (~30 to ~93 IU) than in Units I and II but has no excursions above 100 IU.

### Natural gamma radiation

NGR counting periods were 10 min, and measurement spacing was fixed at 20 cm (Fig. F28). In Unit I, Site U1413 NGR values increase within the uppermost 6 m and then decrease slightly with depth. In Unit II, NGR values gradually increase with depth to peak between 180 and 220 mbsf, below which they range between ~14 and ~38 cps. Poor correlation of NGR values between Sites U1413 and U1379 is likely due to mass movement in Unit I and significantly different thicknesses of Units II and III at the two sites (see “[Lithostratigraphy and petrology](#)”).

### *P*-wave velocity

*P*-wave velocity at Site U1413 was measured on the working halves of sediment split cores using the *P*-wave caliper (Fig. F29). From 0 to 20 mbsf, *P*-wave velocities average 1600 m/s. Because of core disturbance, only a few measurements were taken between

20 and 200 mbsf, and values are variable. Below 200 mbsf, *P*-wave velocities average 1960 m/s. Velocities obtained from Site U1379 are slightly lower than those from Site U1413.

### Thermal conductivity

Thermal conductivity measurements were conducted on soft-sediment whole-round cores using the needle-probe method and on lithified split cores using the half-space method (see “[Physical properties](#)” in the “Methods” chapter [Harris et al., 2013]). Above 200 mbsf, thermal conductivity increases with depth from 0.9 to 1.25 W/(m·K) (Fig. [F30A](#)). Low thermal conductivity values are observed from 40 to 50 mbsf and may reflect disturbance caused by gas expansion. Below 200 mbsf, thermal conductivity values slightly increase with depth to 1.35 W/(m·K) at the bottom of Hole U1413C. Best-fit linear relationships for the thermal conductivity values above and below 200 mbsf are shown in Figure [F30A](#). Thermal conductivity values below ~200 mbsf are similar to the higher end of those measured at Site U1379 during Expedition 334.

### Downhole temperature and heat flow

Five downhole temperature measurements were attempted using the APCT-3 between 21 and 65 mbsf in Hole U1413A; however, two of the measurements could not be used because of a calibration problem with the tool. The remaining three measurements, which were taken with a different APCT-3, provide a least-squares gradient of 49°C/km (Fig. [F30B](#)). The mean thermal conductivity of 1.15 W/(m·K) yields a heat flow of 56 mW/m<sup>2</sup>.

We use the measured temperatures and the estimated heat flow value of 56 mW/m<sup>2</sup> to estimate temperatures at greater depths using the Bullard (1939) method (see “[Physical properties](#)” in the “Methods” chapter [Harris et al., 2013]). This method assumes steady-state conductive heat flow in the sediment. We compared two models for the variation of thermal conductivity with depth, *k*(*z*). Model 1 assumes linear increases of thermal conductivity with depth. Model 2 is based on the accurate trace of each thermal conductivity value we measured. Both models yield similar results. Least-squares fits for Models 1 and 2 yielded values of 7.40° and 7.36°C, respectively, for the sediment/water interface and 35.29° and 35.31°C, respectively, at the bottom of Hole U1413C.

### Sediment strength

Sediment strength was measured with both the automated vane shear and penetrometers. To compare the two measurement types, unconfined shear

strength can be estimated as one half of unconfined compressive strength (Blum, 1997). Results are shown in Figure [F31](#). Strength values generally increase with depth. Vane shear strength increases linearly from ~12 kPa near the seafloor to ~44 kPa at 15 mbsf. From 15 to 40 mbsf, values decrease to ~17 kPa. From ~40 to ~140 mbsf, vane shear strength increases again to a maximum of ~173 kPa. Compressive strength from penetrometer measurements shows similar trends, with a linear increase from 0 to 15 mbsf to a maximum value of ~80 kPa. From 15 to ~40 mbsf, values become variable and decrease to a minimum of ~39 kPa. From 40 to 140 mbsf, compressive strength shows an approximately linear increase to ~500 kPa. Below 140 mbsf, compressive strength values measured by the needle penetrometer are highly variable but generally increase with depth to 320 mbsf, with lower values measured between 320 and 370 mbsf. In Unit III, values range between ~674 and >1500 kPa. High values occur within the sand-rich section below 540 mbsf (see “[Lithostratigraphy and petrology](#)”).

### Color spectrophotometry

Reflectance *L*\* values generally range between 23 and 50 throughout the site (Fig. [F32](#)). Reflectance *a*\* and *b*\* values range between -2 and 2 and between -7 and 0, respectively, and are generally more variable within Units I and II than within Unit III.

### Electrical conductivity and formation factor

Formation factor was obtained from electrical conductivity measurements in the *y*- and *z*-directions on the split cores from most of Hole U1413A (0–140 mbsf) and all of Hole U1413B (Fig. [F33](#)). The *y* and *z* measurements are similar to each other in both holes, indicating little anisotropy in the sediments. Values in Hole U1413A and Hole U1413B are consistent. Formation factor values increase from 2 to ~3.5 in the uppermost 20 m of sediments. From 20 to ~100 mbsf, high scatter may reflect core disturbance from gas expansion. Below ~100 mbsf, formation factor shows less scatter, with values ranging between ~4 and ~5, and trends are inversely correlated to variations in porosity, suggesting that data are probably reliable below the zone of gas disturbance.

### Paleomagnetism

Cores 344-U1413A-1H through 18H were cored with the APC using two nonmagnetic core barrels and were oriented with the FlexIT orientation tool. Cores 344-U1413A-19X through 26X were cored with the XCB using a standard core barrel. Cores 344-U1413B-1H through 3H were cored with the APC

without orientation. Cores 344-U1413C-2R through 43R were cored with the RCB. We measured the natural remanent magnetization (NRM) of archive section halves. In order to isolate the characteristic remanent magnetization (ChRM), the archive section halves were demagnetized in an alternating field (AF) up to 40 mT and measured with the pass-through superconducting rock magnetometer (SRM) at 2.5–5 cm intervals. In order to verify the section data, we demagnetized 119 discrete samples using a progressive AF demagnetization technique and measured them in the SRM.

### Natural remanent magnetization of cores

Downhole variations of paleomagnetic data observed at Site U1413 are shown in Figures F34, F35, and F36. In Unit I, cores recovered from 0 to 44.6 mbsf are silty clay and sand layers (see “[Lithostratigraphy and petrology](#)”). The variations in NRM intensity of these sediments are correlated with lithology. For the depth intervals of 0 to ~4 mbsf and ~20 to ~25 mbsf, these sandy sediments have a mean NRM intensity on the order of  $\sim 10^{-1}$  A/m. Sediments between ~5 and 20 mbsf are more silty and turbidite-like and have a lower NRM intensity with a mean of  $10^{-2}$  A/m (Fig. F34). This pattern is also confirmed in paleomagnetic observations in Hole U1413B (Fig. F35), serving as a regional marker for correlation of these two holes. Paleomagnetic measurements on the calcareous clayey silt with minor sandstone in Unit II (44.6–366.45 mbsf) give highly variable NRM intensity values. A significant downhole increase in NRM intensity is present between ~42 and 150 mbsf (Fig. F34), probably reflecting the higher content of sand downhole within this interval. For the depth interval of 150 to ~185 mbsf, low and high NRM intensities vary between  $3.74 \times 10^{-4}$  and  $8.71 \times 10^{-1}$  A/m, with a mean of  $7.23 \times 10^{-3}$  A/m. In Hole U1413C, sediments in Units II and III (~178–578.8 mbsf) have fairly constant NRM intensity values (average of  $3.61 \times 10^{-3}$  A/m; Fig. F36). Variations in magnetic susceptibility are consistent with the variations in NRM intensity (see “[Physical properties](#)”).

Similar to what was observed at Site U1412, the magnetic flux jumps along the  $\gamma$ -axis superconducting quantum interference device produced large magnetic noise anomalies that affected the measurements of core sections, especially in the silty and turbidite layers of Unit I (see circled data in Fig. F35).

### Paleomagnetic demagnetization results

For the sediment sections, we employed AF demagnetization steps up to 40 mT. AF demagnetization to 15 mT seems to be effective in removing the drilling

overprint magnetization (e.g., Fig. F34). ChRM directions of both normal and reversed polarities can generally be isolated from the pass-through measurements (Fig. F37).

The magnetic properties observed from the section halves were confirmed by discrete sample measurements (Fig. F38). We demagnetized 119 discrete samples (57 from Hole U1413A, 8 from Hole U1413B, and 53 from Hole U1413C). AF demagnetization was successful in isolating the ChRM for most of the discrete samples. Some discrete samples, however, displayed more complicated demagnetization paths that do not simply decay toward the origin. Several representative vector plots of discrete samples are shown in Figure F38. ChRM inclinations of discrete samples obtained from principal component analysis (Kirschvink, 1980) are plotted in Figure F39.

### Magnetostratigraphy

As shown in Figure F39, samples from the lower parts of Unit II and Unit III in Hole U1413C are dominated by negative inclinations (reversed polarity). At ~480 mbsf, the stable inclinations switch polarity from reversed to normal and then change back to reversed polarity at ~520 mbsf. The LO of the nanofossil species *Helicosphaera sellii* (1.34 Ma) is also placed around this interval (see “[Paleontology and biostratigraphy](#)”), suggesting the polarity changes in the depth range of 480–520 mbsf may correspond to the Olduvai Subchron (1.778–1.945 Ma). If this is correct, sediments in this depth interval have an average sedimentation accumulation rate of 239.52 m/m.y., similar to those in Hole U1380C. The sedimentation accumulation rate for the uppermost 480 m of sediment in Hole U1413C is 269.97 m/m.y.

Like the magnetic records at other Expedition 344 sites, several relatively well defined polarity intervals were identified in the downhole magnetostratigraphic records of Site U1413. However, it is difficult to reliably correlate these intervals to the geomagnetic polarity timescale because the biostratigraphic data are lacking in the cored interval. We tentatively place the Jaramillo Subchron (0.988–1.072 Ma) between 0.58 and 94.21 mbsf, which would suggest an extremely high sedimentation rate (824 m/m.y.) for this interval. Additional shore-based work is needed to correctly interpret the record.

## Downhole logging

### Logging operations

Coring in Hole U1413C ended with Core 344-U1413C-43R reaching 582.2 mbsf at 1350 h on 29 November 2012 (all times are local Costa Rica time,

UTC – 6). A wiper trip was then started to prepare the hole for logging. The hole was drilled without major problems, but during the wiper trip, high torque was encountered below ~250 mbsf. While the hole was being displaced with heavy mud (10.5 ppg), high standpipe pressures were noted. Moreover, 20,000–30,000 lb of overpull was observed when raising the drill pipe to logging depth. Because of poor hole conditions, it was decided to first deploy a slick triple combo tool string without a radioactive source.

The triple combo tool string included (from top to bottom) the Enhanced Digital Telemetry Cartridge (EDTC), Hostile Environment Natural Gamma Ray Sonde (HNGS), Hostile Environment Litho-Density Sonde (HLDS; no radioactive source, measuring just the caliper), and Dual Induction Tool (Fig. F40). For explanation of the acronyms and details on the wireline tools, see the “[Methods](#)” chapter (Harris et al., 2013). Rig-up of the triple combo started at 1045 h on 30 November, and the tool string started down the hole at 1200 h. After exiting the drill pipe, an obstruction was encountered with the base of the tool string at 187 mbsf (the mbsf unit used here corresponds to the wireline depth below seafloor [WSF] depth scale; see the “[Methods](#)” chapter [Harris et al., 2013]). Repeated attempts to pass the obstruction were unsuccessful, and at 1320 h we started to log the 84 m section of open hole from the obstruction to the base of the drill pipe (observed on the gamma ray log at 103 mbsf). The seafloor was detected from a step on the NGR log at 550 mbrf (the driller’s seafloor depth for this hole was 551.4 mbrf). The triple combo reached the rig floor and was rigged down at 1435 h. In the short hole interval that could be logged, the triple combo caliper showed sections that were nearly in gauge. After consultation with the Co-Chief Scientists, we decided to run two additional short tool strings focused on imaging borehole breakouts, the UBI and the FMS (Fig. F40).

The second tool string included (from top to bottom) the EDTC, HNGS, General Purpose Inclinometry Tool (GPIT), and UBI. Rig-up started at 1435 h on 30 November, and the UBI tool string started down the hole at 1600 h. After reaching the obstruction encountered in the previous run at 187 mbsf, we ran two complete passes. The UBI tool string returned to the rig floor and was rigged down at 1930 h.

The third tool string included (from top to bottom) the EDTC, HNGS, GPIT, and FMS. Rig-up started at 1930 h, and the FMS tool string started down the hole at 2010 h. Again, the tool string encountered an obstruction at 186 mbsf, and we ran two complete passes in the open hole. The FMS images in the first pass looked good up to the base of the drill pipe, and

we asked the drillers to raise the drill pipe to increase the length of open hole available for logging. The second pass encountered the base of the drill pipe at 93.5 mbsf (from the NGR log). The FMS tool string reached the rig floor at 2220 h, and logging operations at Hole U1413C ended when the rig down of the wireline system was completed at 2300 h on 30 November.

### Downhole log data quality

The downhole log data collected in Hole U1413C were processed to convert to depth below seafloor and to match depths between different logging runs. The resulting depth scale is wireline matched depth below seafloor (WMSF; see the “[Methods](#)” chapter [Harris et al., 2013]), and from here on mbsf denotes the WMSF depth scale.

A key factor that influences downhole log data quality is the size and irregularity of the borehole. Measurements of the diameter of Hole U1413C are summarized in Figure F41. The LCAL track in this figure is measured by a single caliper arm on the HLDS and shows a hole that is larger than the RCB bit diameter (9.875 inches) in the two intervals below 169 mbsf and above 148 mbsf, with values that are locally greater than the maximum measurable range (~18 inches). In contrast, the hole size is close to the bit diameter in the 148–169 mbsf interval. The FMS tool measures hole diameter in two orthogonal directions from the aperture of the two pairs of arms that support the microresistivity measurement pads. These orthogonal hole diameter measurements, shown in the C1 and C2 tracks in the figure, show that the borehole is enlarged in both directions below 169 mbsf. In contrast, above 148 mbsf the hole diameter is clearly greater than the bit size in only one direction. The larger borehole diameter in this interval is measured by Caliper C1 in the first FMS pass and by Caliper C2 in the second (see “[Borehole images and breakouts](#)”).

The overall quality of the logging data can be assessed from the repeatability of measurements acquired in different runs or passes. In general, the downhole log data acquired in Hole U1413C show excellent repeatability. Figure F41 compares spectral gamma ray logs acquired by the HNGS tool in the UBI and FMS tool strings. The gamma ray measurement is highly attenuated when the tool is inside the BHA (above 93–103 mbsf in Hole U1413C), and data in this interval should only be used qualitatively.

### Log characterization and logging units

The logging measurements acquired in Hole U1413C are summarized in Figure F42. The total gamma ray data measured by the HNGS tool are generally

comparable to the NGR measurements made on cores. The total gamma ray values measured by the HNGS tool are expressed in an American Petroleum Institute (gAPI) scale based on a standard artificial formation built to simulate about twice the radioactivity of a typical shale and conventionally set to 200 gAPI (Ellis and Singer, 2007). The units of the NGR measurements made on whole core sections are in counts per second (cps; for a detailed description of the NGR apparatus, see Vasiliev et al., 2011). The comparison of log and core NGR measurements in Figure F42 shows that their curves overlap if 1 cps equals  $\sim 2$  gAPI. The general agreement in the trend of the total gamma ray log and core values above 169 mbsf suggests that hole conditions did not impact the gamma ray measurements in this interval.

Figure F42 also shows the abundances of the three naturally radioactive elements (U, Th, and K) measured by the spectral HNGS tool. The measured resistivities are generally between 1 and 2  $\Omega\text{m}$ ; low values  $< 1$   $\Omega\text{m}$  measured at 170–172 mbsf and below 182 mbsf are likely due to a locally enlarged borehole (Fig. F41). Finally, the figure shows the borehole radius image obtained by the UBI. The measured traveltimes of the ultrasonic pulse from the UBI transducer to the borehole wall give a detailed image of the borehole radius as a function of azimuth.

We distinguished three logging units in the interval logged in Hole U1413C. Logging Unit 1 (93–148 mbsf) is characterized by total gamma ray values between 38 and 46 gAPI, by a relatively low U content between 1.4 and 2.7 ppm, and by relatively low resistivities just above 1  $\Omega\text{m}$ . This is the interval where the UBI images show vertical bands with large reflection radiuses and the borehole diameter is large in one of the directions measured by the FMS caliper arms (Fig. F41). In contrast, the borehole is almost circular and nearly in gauge throughout Logging Unit 2 (148–169 mbsf). Compared to Unit 1, Unit 2 displays a higher total gamma ray ( $\sim 60$  gAPI), higher U content ( $\sim 3$  ppm), and higher resistivity. As the resistivity of sedimentary formations is mostly controlled by porosity, the increase in resistivity implies a decrease in porosity in Logging Unit 2. This decrease in porosity and the circular, in gauge borehole of Unit 2 suggest a more consolidated formation than in Unit 1. At the boundary between Logging Units 1 and 2, magnetic susceptibility and NGR data measured on cores also show a significant change around 148 mbsf in Hole U1413A (see “[Physical properties](#)”). The borehole seems to be washed out in all directions in Logging Unit 3 (169–184 mbsf), and the low values of natural radioactivity and resis-

tivity measured at 170–172 mbsf are likely artifacts caused by a pronounced borehole enlargement.

### Borehole images and breakouts

Borehole images collected by the UBI ultrasonic tool and the FMS microresistivity tool are shown in Figure F43. The three images display the UBI amplitude (which is related to the small-scale roughness of the borehole wall), the UBI borehole radius image (which is proportional to the measured traveltime), and the FMS images collected by the four microresistivity pads.

The UBI images show an irregular, large-radius borehole in Logging Unit 3 (below 169 mbsf) and a borehole that is smooth and has a nearly constant radius in Logging Unit 2 (148–169 mbsf). Within Logging Unit 1 (above 148 mbsf), the images show two nearly vertical bands of high rugosity (low amplitude) and large borehole radius (large traveltime). These two bands are on opposite sides of the borehole and span sectors of  $\sim 30^\circ$ – $90^\circ$ . For a nominal 10 inch borehole diameter, the width of these bands is 6.5–20 cm.

The FMS images from Logging Unit 1 show low resistivity values (dark) in the two opposite pads that are in the same direction as the high-rugosity/large-radius bands in the UBI images. The FMS caliper measurements in this interval (Fig. F41) show that the pads measuring low resistivities also measure the larger borehole diameter. As the FMS tool is pulled up, the 6 cm wide microresistivity pads get stuck in these large-diameter borehole sectors, and the measured low resistivity is likely caused by the rough borehole surface that prevents close contact with the pad. The azimuth of the pair of pads measuring the larger borehole diameter in the second pass of the FMS run is also apparent in Figure F43, showing that the UBI and FMS measurements of these large-diameter borehole sectors are entirely consistent.

The nearly vertical bands of large-diameter, rugose borehole in Logging Unit 1 are borehole breakouts. When a vertical borehole is drilled in a region with significant deviatoric (maximum–minimum) horizontal stress, the resulting hoop stress along the borehole wall reaches a maximum compressive value at the azimuth of the minimum horizontal stress. If the hoop stress is greater than the rock strength, the rock fails, giving rise to characteristic borehole breakouts (e.g., Zoback et al., 2003). Borehole breakouts have been imaged with ultrasonic and four-arm caliper logs in many other studies (e.g., Bell and Gough, 1979; Plumb and Hickman, 1985; Zoback et al., 2003; Lin et al., 2010). The minimum horizontal stress in the 148–169 mbsf interval in Hole U1413C is oriented approximately north–south.

## References

- Bell, J.S., and Gough, D.I., 1979. Northeast-southwest compressive stress in Alberta: evidence from oil wells. *Earth Planet. Sci. Lett.*, 45(2):475–482. doi:10.1016/0012-821X(79)90146-8
- Blum, P., 1997. Physical properties handbook: a guide to the shipboard measurement of physical properties of deep-sea cores. *ODP Tech. Note*, 26. doi:10.2973/odp.tn.26.1997
- Bullard, E.C., 1939. Heat flow in South Africa. *Proc. R. Soc. A*, 173(955):474–502. doi:10.1098/rspa.1939.0159
- Ellis, D.V., and Singer, J.M., 2007. *Well Logging for Earth Scientists* (2nd ed.): Dordrecht, The Netherlands (Springer).
- Expedition 334 Scientists, 2012. Site U1379. In Vannucchi, P., Ujiie, K., Stroncik, N., Malinverno, A., and the Expedition 334 Scientists, *Proc. IODP*, 334: Tokyo (Integrated Ocean Drilling Program Management International, Inc.). doi:10.2204/iodp.proc.334.104.2012
- Goll, R.M., 1980. Pliocene–Pleistocene radiolarians from the East Pacific Rise and the Galapagos spreading center, Deep Sea Drilling Project Leg 54. In Rosendahl, B.R., Hekinian, R., et al., *Init. Repts. DSDP*, 54: Washington, DC (U.S. Govt. Printing Office), 425–454. doi:10.2973/dsdp.proc.54.116.1980
- Gradstein, F.M., Ogg, J.G., Schmitz, M.D., and Ogg, G.M. (Eds.), 2012. *The Geological Time Scale 2012*: Amsterdam (Elsevier).
- Harris, R.N., Sakaguchi, A., Petronotis, K., Baxter, A.T., Berg, R., Burkett, A., Charpentier, D., Choi, J., Diz-Ferreiro, P., Hamahashi, M., Hashimoto, Y., Heydolph, K., Jovane, L., Kastner, M., Kurz, W., Kutterolf, S.O., Li, Y., Malinverno, A., Martin, K.M., Millan, C., Nascimento, D.B., Saito, S., Sandoval Gutierrez, M.I., Sreaton, E.J., Smith-Duque, C.E., Solomon, E.A., Straub, S.M., Tanikawa, W., Torres, M.E., Uchimura, H., Vannucchi, P., Yamamoto, Y., Yan, Q., and Zhao, X., 2013. Methods. In Harris, R.N., Sakaguchi, A., Petronotis, K., and the Expedition 344 Scientists, *Proc. IODP*, 344: College Station, TX (Integrated Ocean Drilling Program). doi:10.2204/iodp.proc.344.102.2013
- Kirschvink, J.L., 1980. The least-squares line and plane and the analysis of palaeomagnetic data. *Geophys. J. R. Astron. Soc.*, 62(3):699–718. doi:10.1111/j.1365-246X.1980.tb02601.x
- LaFemina, P., Dixon, T.H., Govers, R., Norabuena, E., Turner, H., Saballos, A., Mattioli, G., Protti, M., and Strauch, W., 2009. Fore-arc motion and Cocos Ridge collision in Central America. *Geochem., Geophys., Geosyst.*, 10(5):Q05S14. doi:10.1029/2008GC002181
- Lin, W., Doan, M.-L., Moore, J.C., McNeill, L., Byrne, T.B., Ito, T., Saffer, D., Conin, M., Kinoshita, M., Sanada, Y., Moe, K.T., Araki, E., Tobin, H., Boutt, D., Kano, Y., Hayman, N.W., Flemings, P., Huftile, G.J., Cukur, D., Buret, C., Schleicher, A.M., Efimenko, N., Kawabata, K., Buchs, D.M., Jiang, S., Kameo, K., Horiguchi, K., Wiersberg, T., Kopf, A., Kitada, K., Eguchi, N., Toczko, S., Takahashi, K., and Kido, Y., 2010. Present-day principal horizontal stress orientations in the Kumano forearc basin of the southwest Japan subduction zone determined from IODP NanTroSEIZE drilling Site C0009. *Geophys. Res. Lett.*, 37:L13303. doi:10.1029/2010GL043158
- Plumb, R.A., and Hickman, S.H., 1985. Stress-induced borehole elongation: a comparison between the four-arm dipmeter and the borehole televiewer in the Auburn geothermal well. *J. Geophys. Res.: Solid Earth*, 90(B7):5513–5521. doi:10.1029/JB090iB07p05513
- Raffi, I., Backman, J., Fornaciari, E., Pälke, H., Rio, D., Lourens, L., and Hilgen, F., 2006. A review of calcareous nannofossil astrobiochronology encompassing the past 25 million years. *Quat. Sci. Rev.*, 25(23–24):3113–3137. doi:10.1016/j.quascirev.2006.07.007
- Vasiliev, M.A., Blum, P., Chubarian, G., Olsen, R., Bennigh, C., Cobine, T., Fackler, D., Hastedt, M., Houpt, D., Mateo, Z., and Vasilieva, Y.B., 2011. A new natural gamma radiation measurement system for marine sediment and rock analysis. *J. Appl. Geophys.*, 75:455–463. doi:10.1016/j.jappgeo.2011.08.008
- Zijderveld, J.D.A., 1967. AC demagnetization of rocks: analysis of results. In Collinson, D.W., Creer, K.M., and Runcorn, S.K. (Eds.), *Methods in Palaeomagnetism*: Amsterdam (Elsevier), 254–286.
- Zoback, M.D., Barton, C.A., Brudy, M., Castillo, D.A., Finkbeiner, T., Grollmund, B.R., Moos, D.B., Peska, P., Ward, C.D., and Wiprut, D.J., 2003. Determination of stress orientation and magnitude in deep wells. *Int. J. Rock Mech. Min. Sci.*, 40(7–8):1049–1076. doi:10.1016/j.ijrmms.2003.07.001

**Publication:** 11 December 2013  
**MS 344-107**



Figure F1. Seismic travelttime section along Line 2466 showing the location of Site U1413.

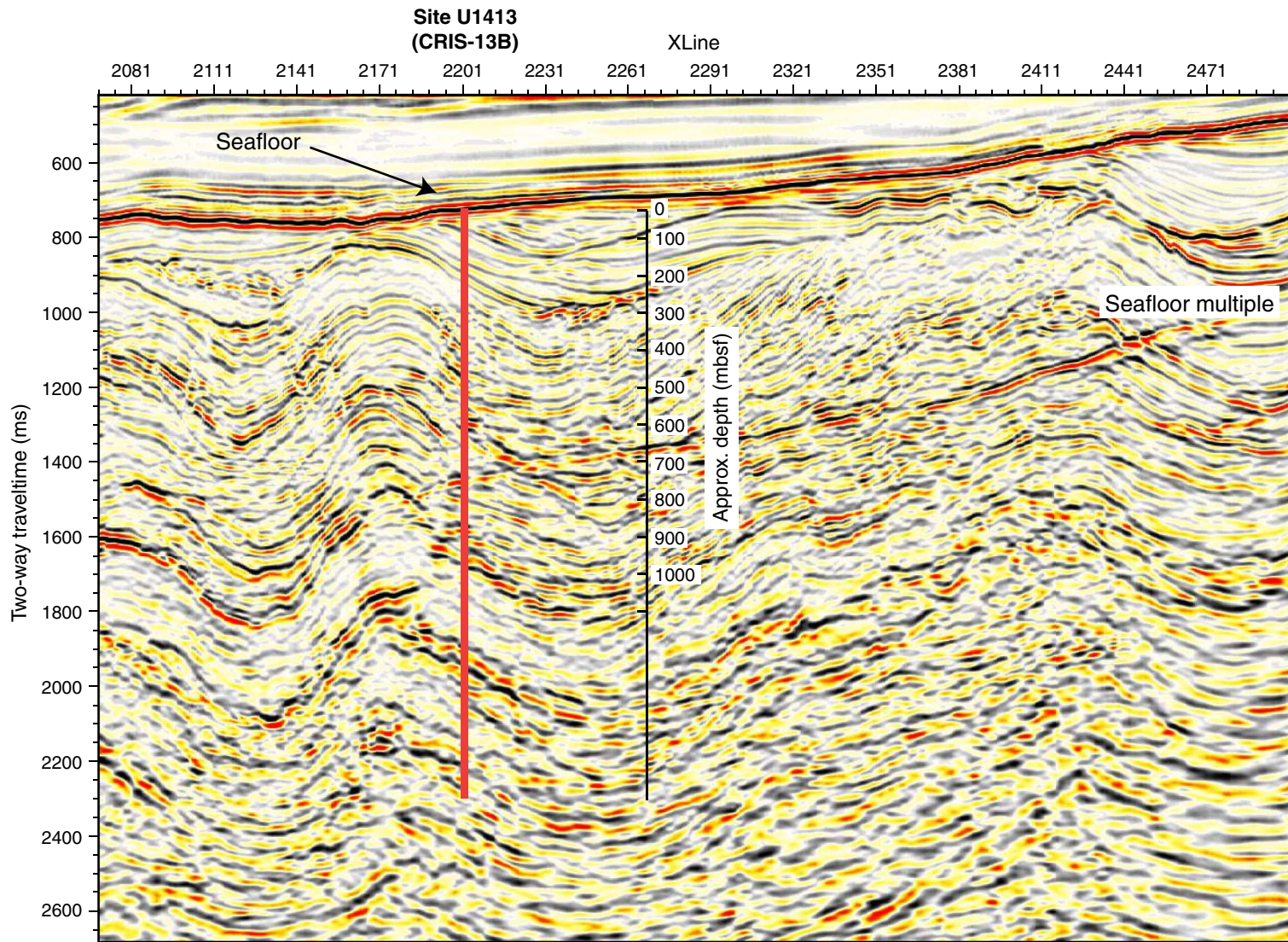


**Figure F2.** Location of Expedition 344 drill sites. Red diamonds denote Expedition 344 sites (U1380, U1381, and U1412–U1414) and yellow diamonds denote Expedition 334 sites not occupied during Expedition 344 (U1378, U1379). Red lines = 3-D seismic survey, black lines = seismic reflection lines. Numbers along the short and long axes of the 3-D survey represent inlines and crosslines, respectively.

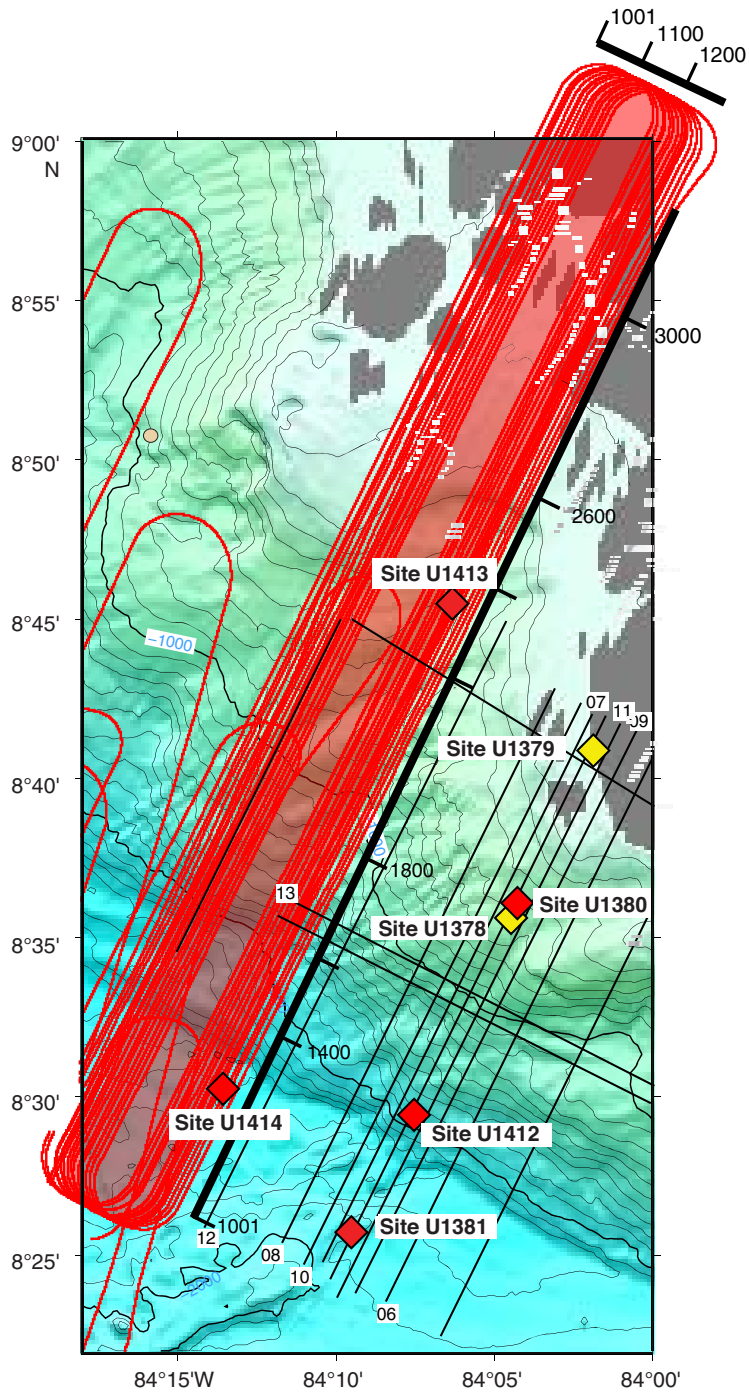
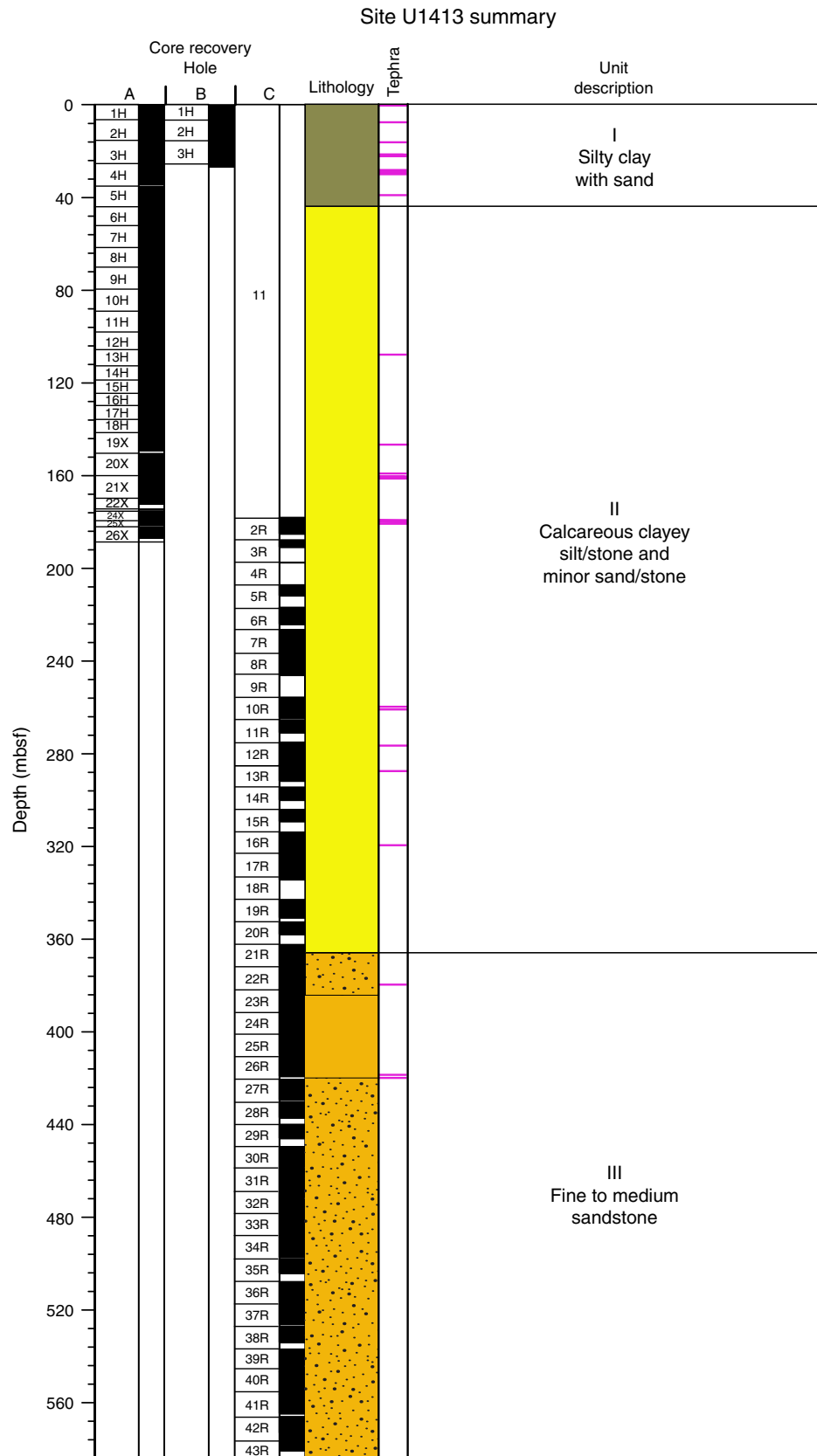
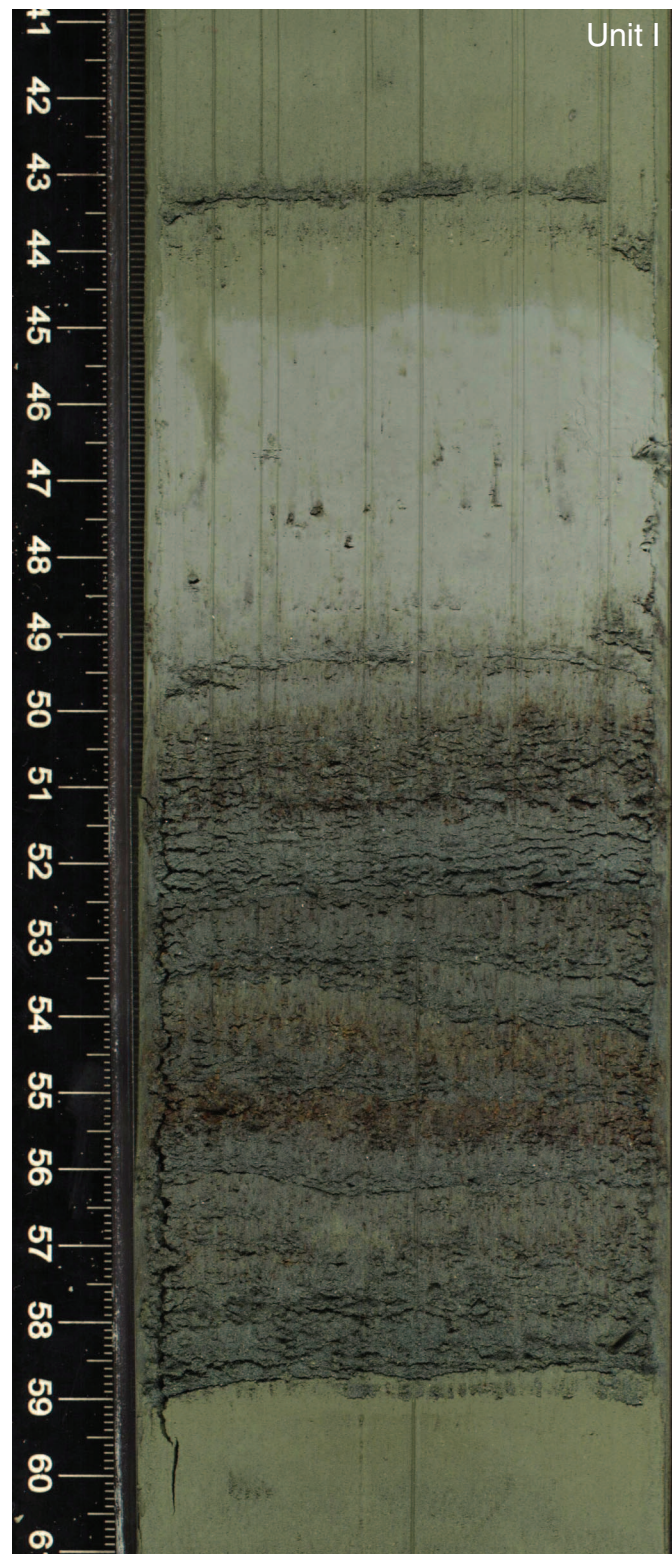


Figure F3. Lithostratigraphic summary of Site U1413.



**Figure F4.** Digital image of typical Unit I sediment showing dark greenish gray silty clay interbedded with turbidite layers, rich in sand of terrigenous origin (interval 344-U1413A-1H-5A, 41–61 cm). Overlying the sand is light-colored extremely fine-grained clay, presumably an altered tephra layer.



**Figure F5.** Digital image of sliding/slumping event in upper Unit I readily characterized by intermixed silty clay and sand and a change in color (interval 344-U1413A-1H-3A, 27–62 cm).



**Figure F6.** Digital image of sliding/slumping event in lower Unit I characterized by brownish green chaotic mixture of silty clay and dark gray sand with occasional large biogenic fragments (interval 344-U1413C-13H-5A, 12–36 cm).

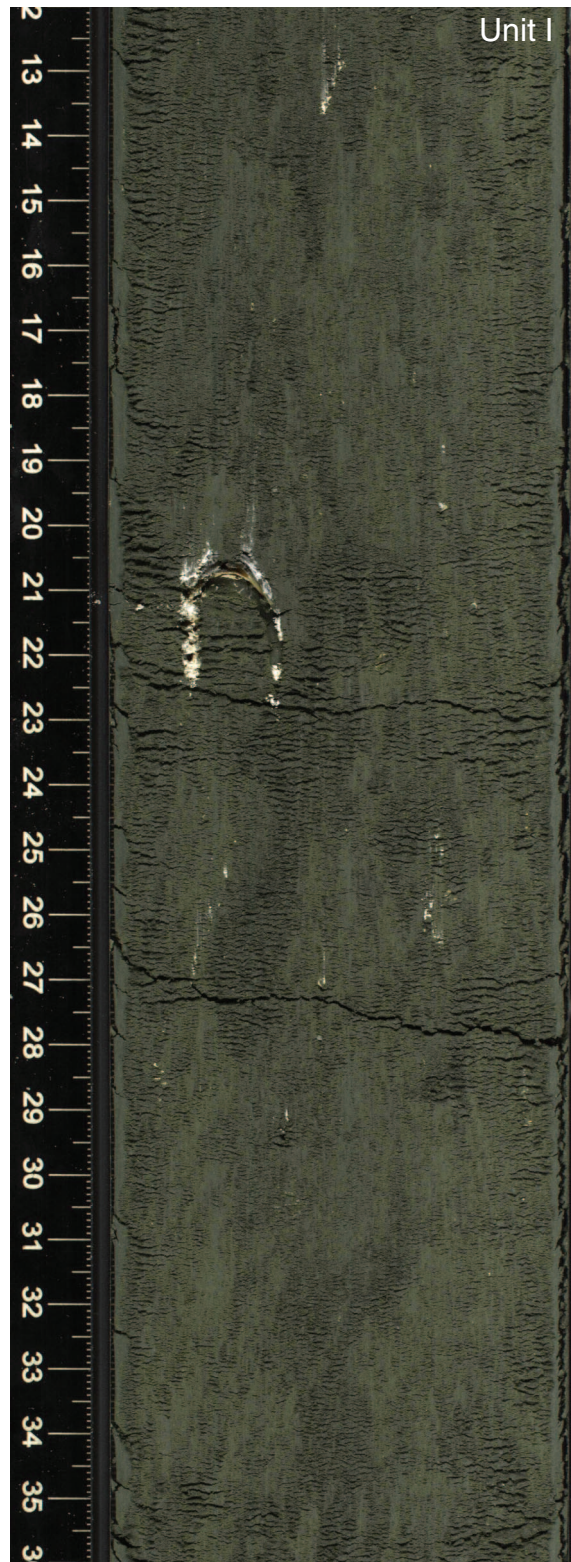


**Figure F7.** Digital image of a light-colored, normally graded, and mostly unlithified tephra layer that underlies a highly bioturbated horizon (interval 344-U1413C-11R-3A, 119–138 cm) and overlies the typical greenish gray calcareous clayey silt of Unit II.



**Figure F8.** Digital image of a massive sandstone bed typical of Unit III (interval 344-U1413C-37R-6A, 116–140 cm).



**Figure F9.** Digital image of a sandstone to conglomerate horizon with large shell and shell fragments and poorly sorted carbonate mud clasts (interval 344-U1413C-33R-3A, 54–80 cm).



**Figure F10.** Digital image of a laminated sandstone sequence with abundant organic debris (interval 344-U1413C-35R-1A, 50–70 cm).



**Figure F11.** Digital image of glauconite grains, which are agglomerated and congregated in conspicuous horizons throughout Unit III (interval 344-U1413C-25R-3A, 40–58 cm).



**Figure F12.** Typical XRD patterns obtained for bulk rock samples, Site U1413. An = analcime, C = calcite, Chl = chlorite (clinochlore), H = heulandite, Ha = halite, Ho = hornblende, L = laumontite, P = plagioclase, Py = pyrite, Q = quartz, S = smectite.

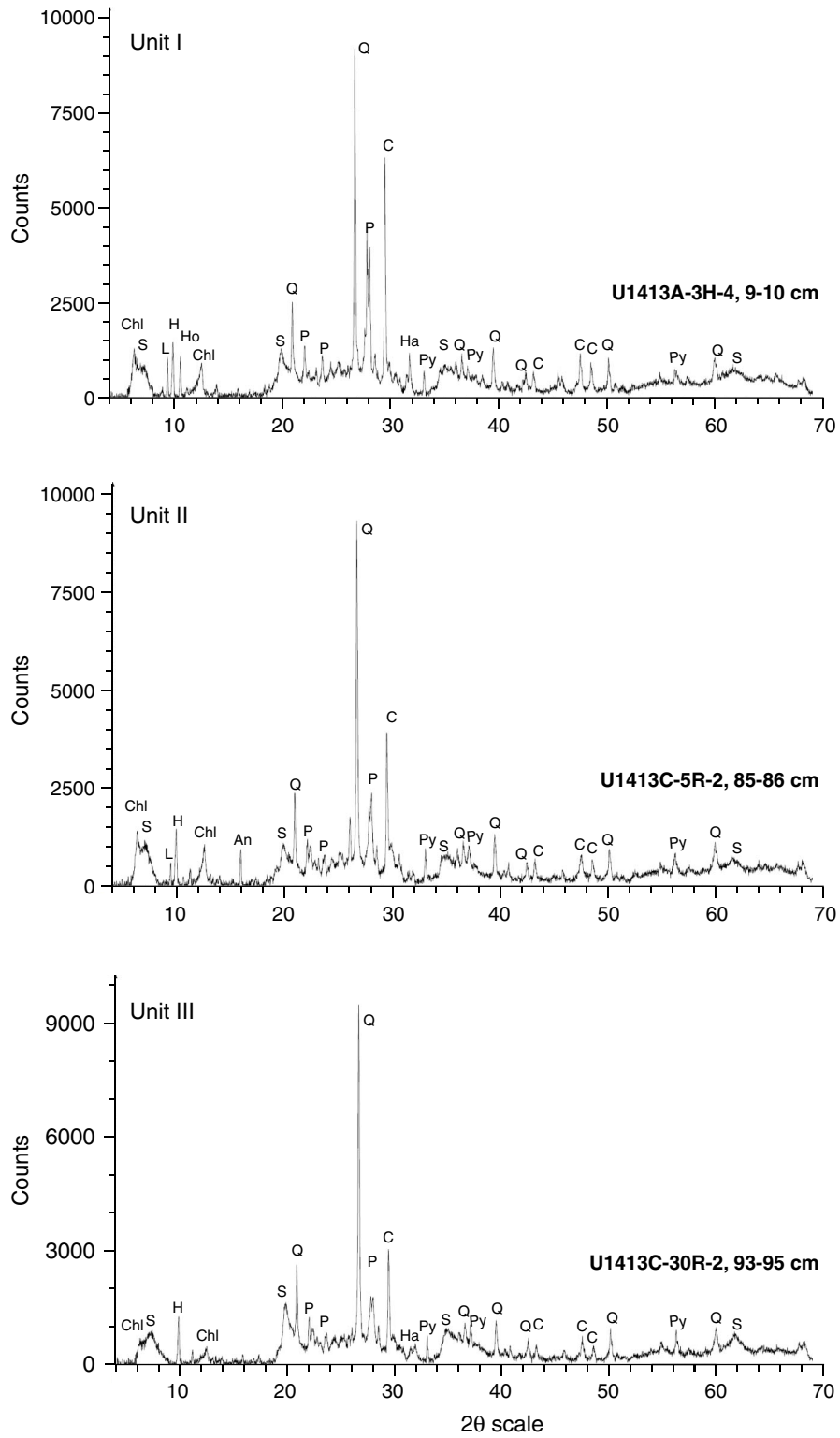




Figure F13. Relative abundance of the most characteristic benthic foraminifer assemblages, Site U1413.

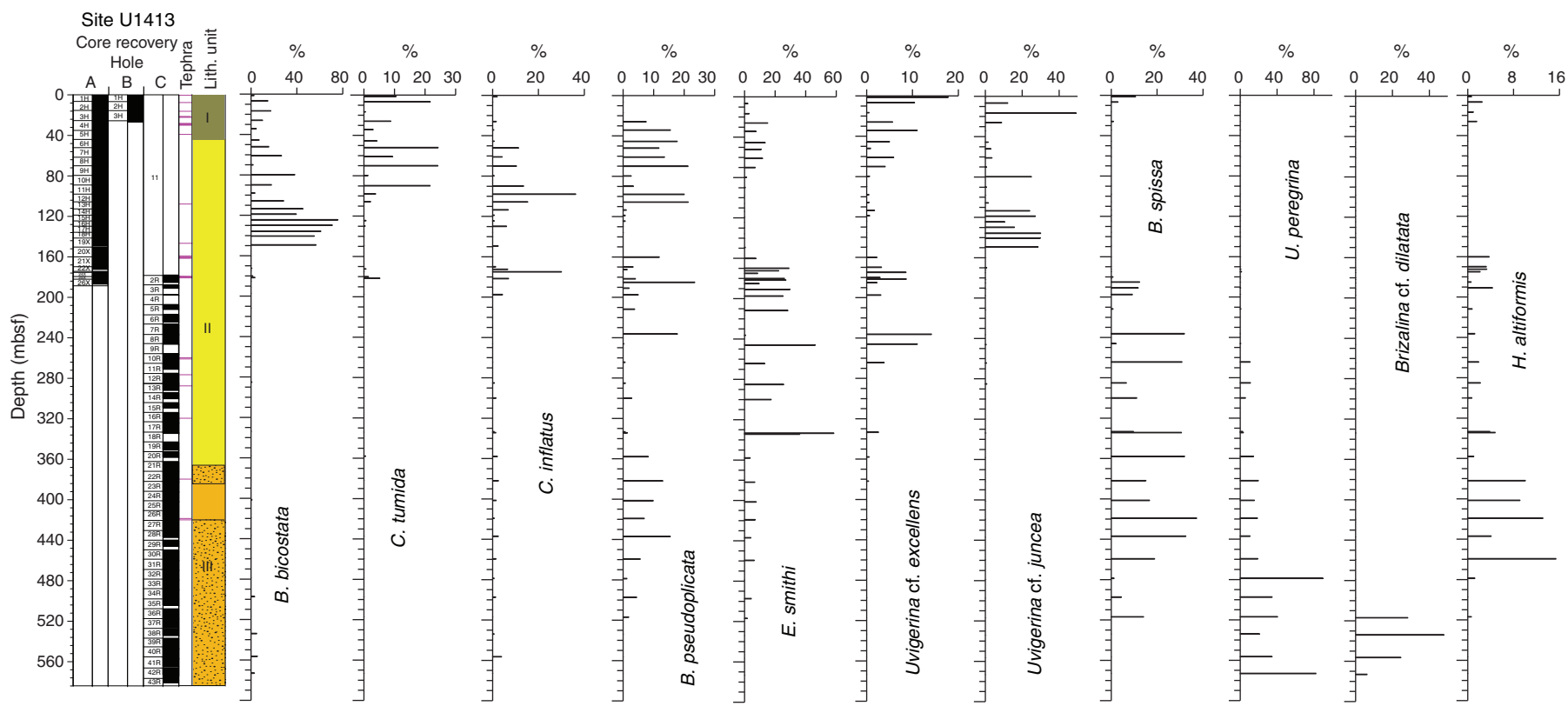


Figure F14. Plot of bedding dip angles, dip angles of faults, and other fractures as a function of depth, Site U1413.

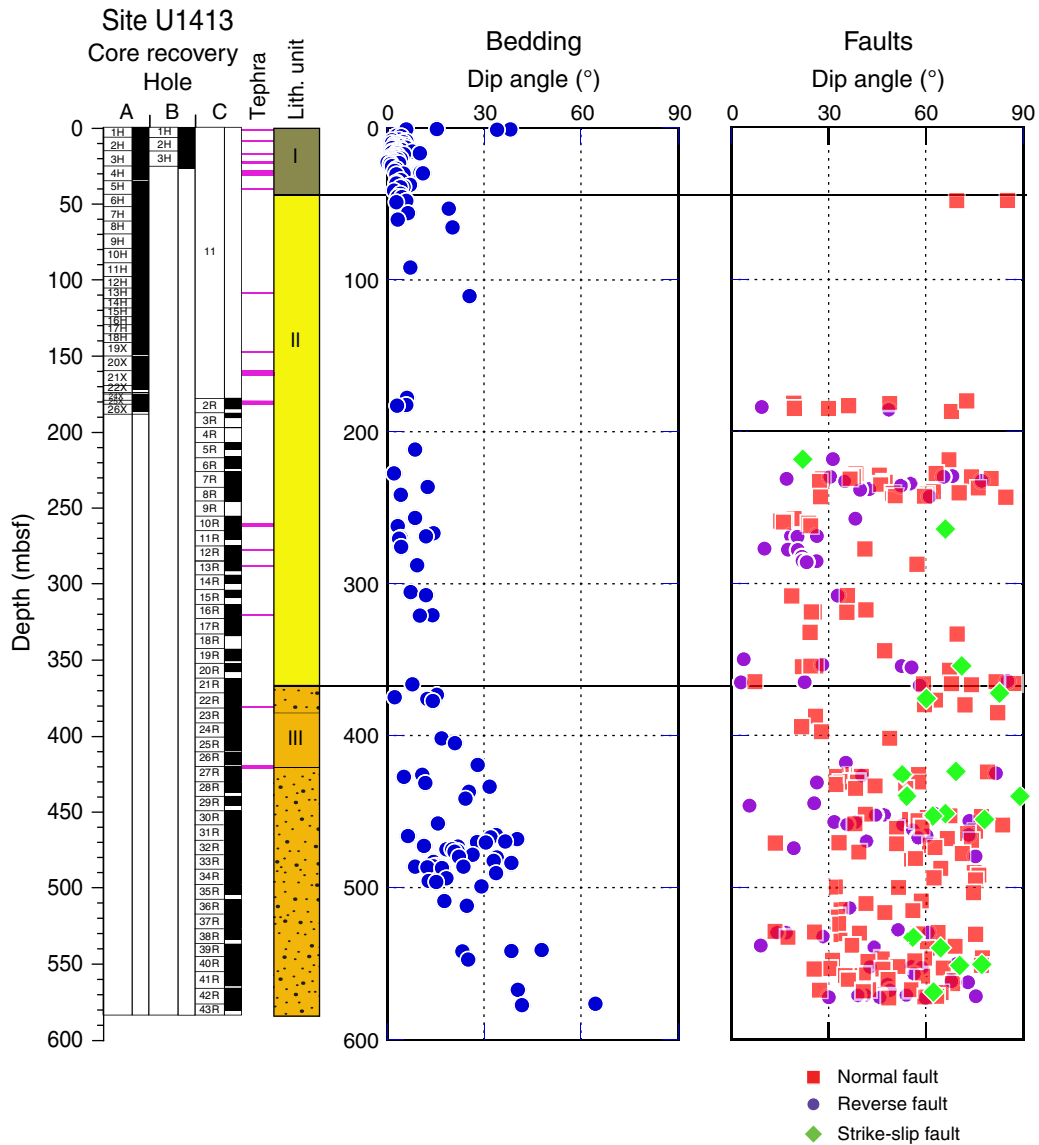


Figure F15. Stereoplots of bedding data for (A) Domain I and (B) Domain II, Site U1413.

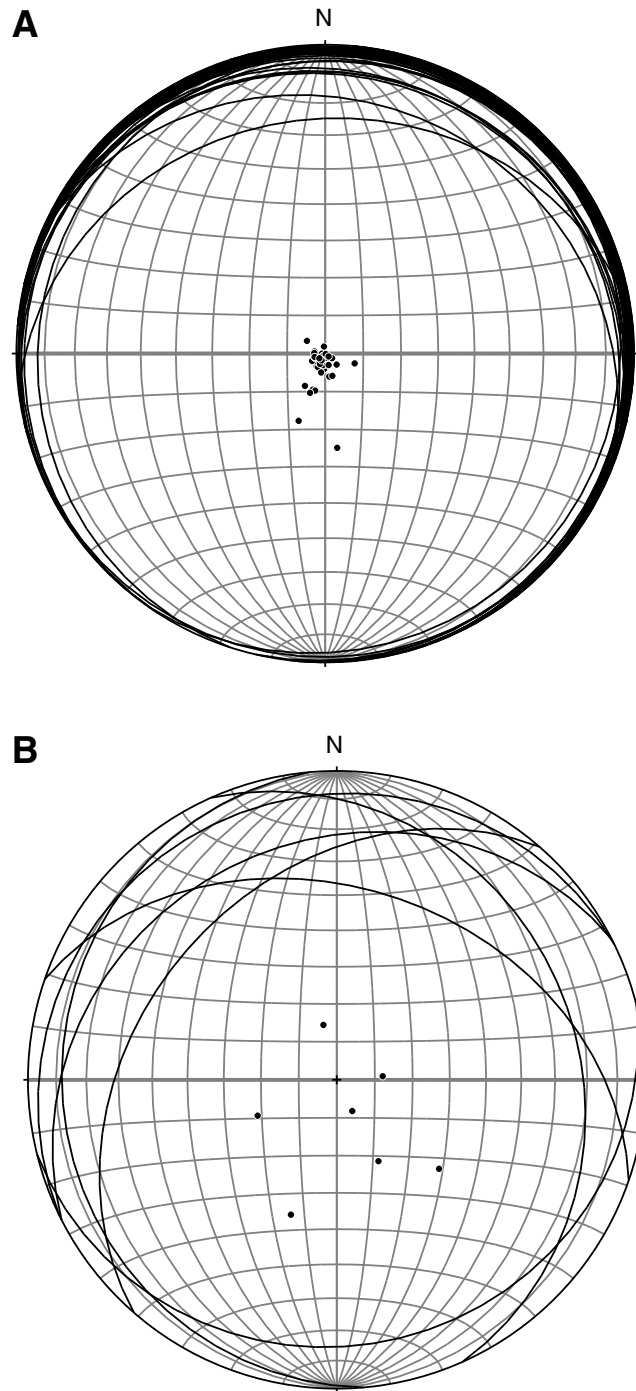
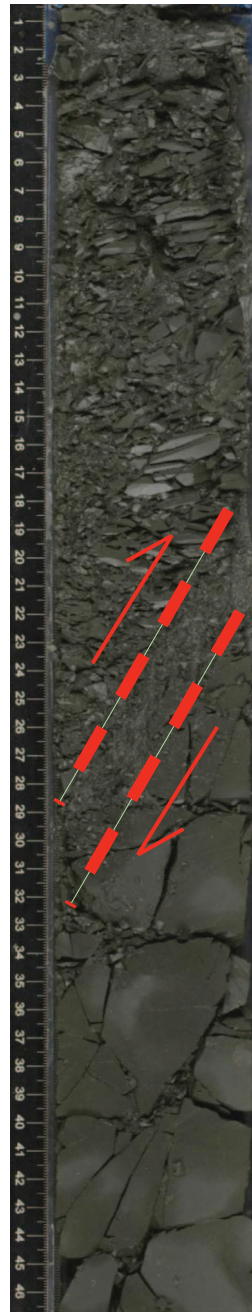
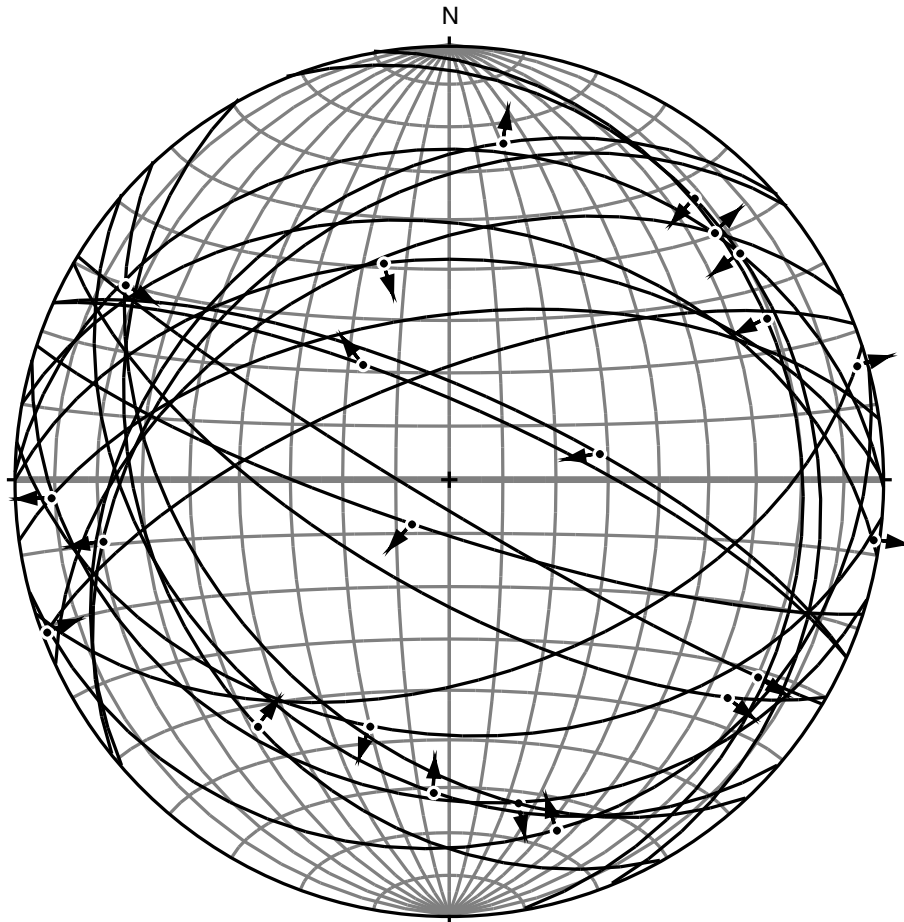


Figure F16. Photograph of high-angle reverse fault in Section 344-U1413B-21R-3.



**Figure F17.** Stereographic diagram showing fault kinematics after paleomagnetic correction, Site U1413. Arrows show direction of hanging wall fault motion. Arrows pointed toward center indicate reverse faults; arrows pointed away from center indicate normal faults.



**Figure F18.** Downhole profiles for salinity, chloride, potassium and sodium, Site U1413. Dashed lines = lithostratigraphic unit boundaries. Solid lines = depths of slumps. Note that the slump at 44.6 mbsf also corresponds to the boundary between lithostratigraphic Units I and II. Blue arrows = bottom seawater values.

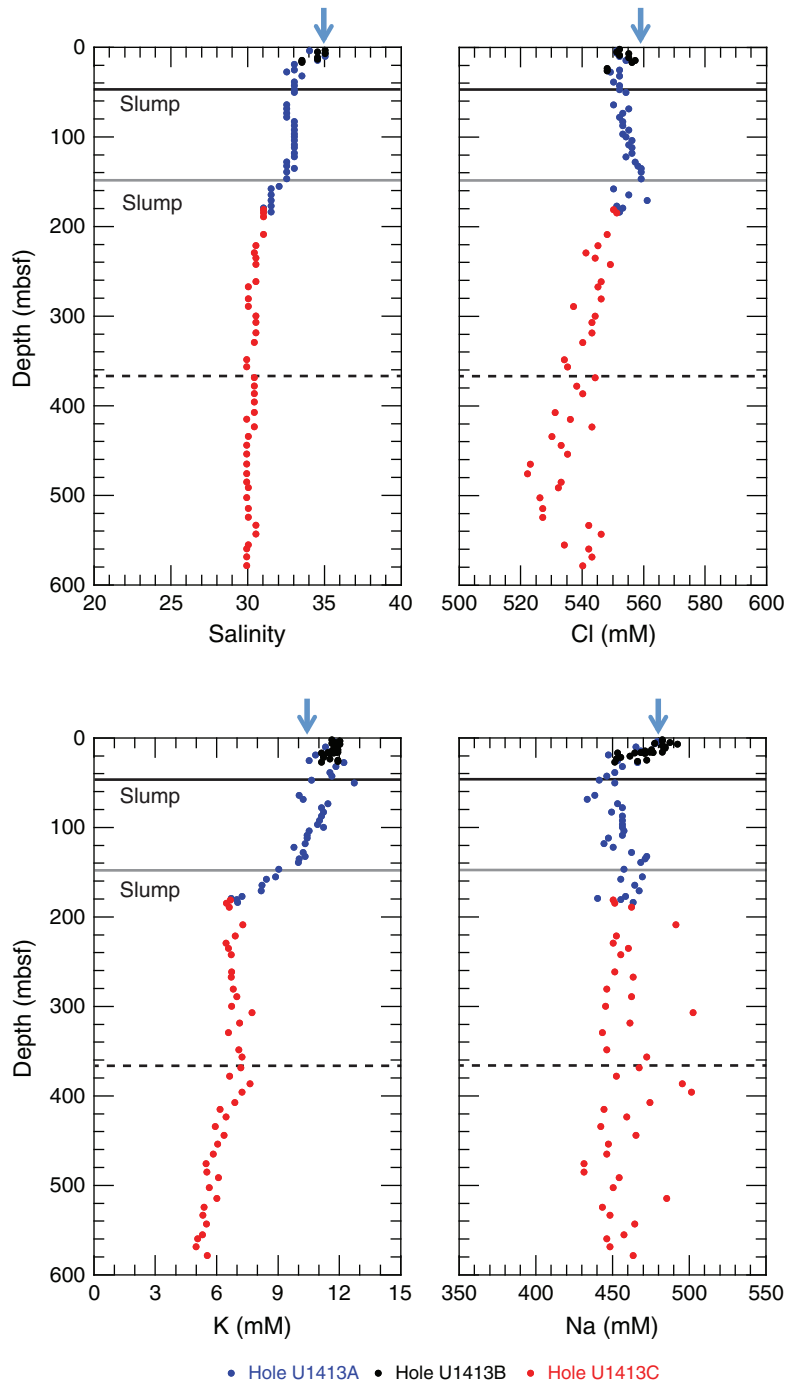


**Figure F19.** Downhole profiles for sulfate, methane, and alkalinity in the uppermost 30 m of Site U1413. Solid line = sulfate–methane transition zone (SMTZ), the horizon where sulfate is consumed and methane begins to increase with depth. Alkalinity increases rapidly below the SMTZ, suggesting a contribution from anaerobic oxidation of methane. Blue arrows = bottom seawater values.

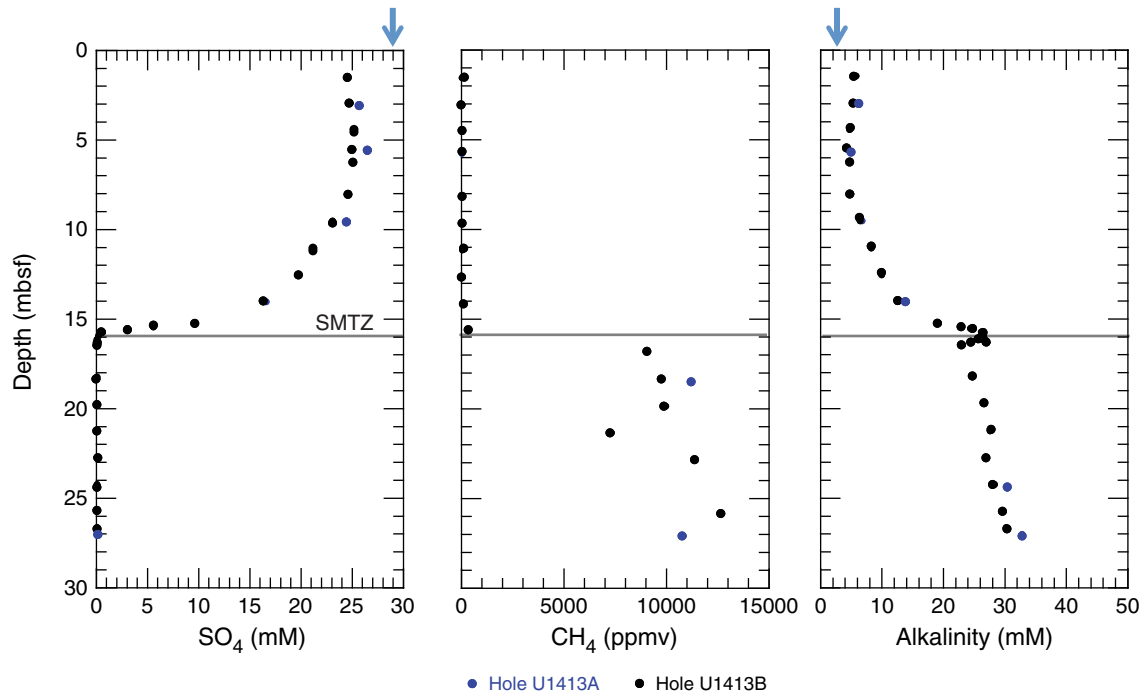


**Figure F20.** Downhole profiles for alkalinity, sulfate, ammonium, calcium, and magnesium, Site U1413. Dashed lines = lithostratigraphic unit boundaries. Solid lines = depths of slumps. Note that the slump at 44.6 mbsf also corresponds to the boundary between lithostratigraphic Units I and II. Blue arrows = bottom seawater values.

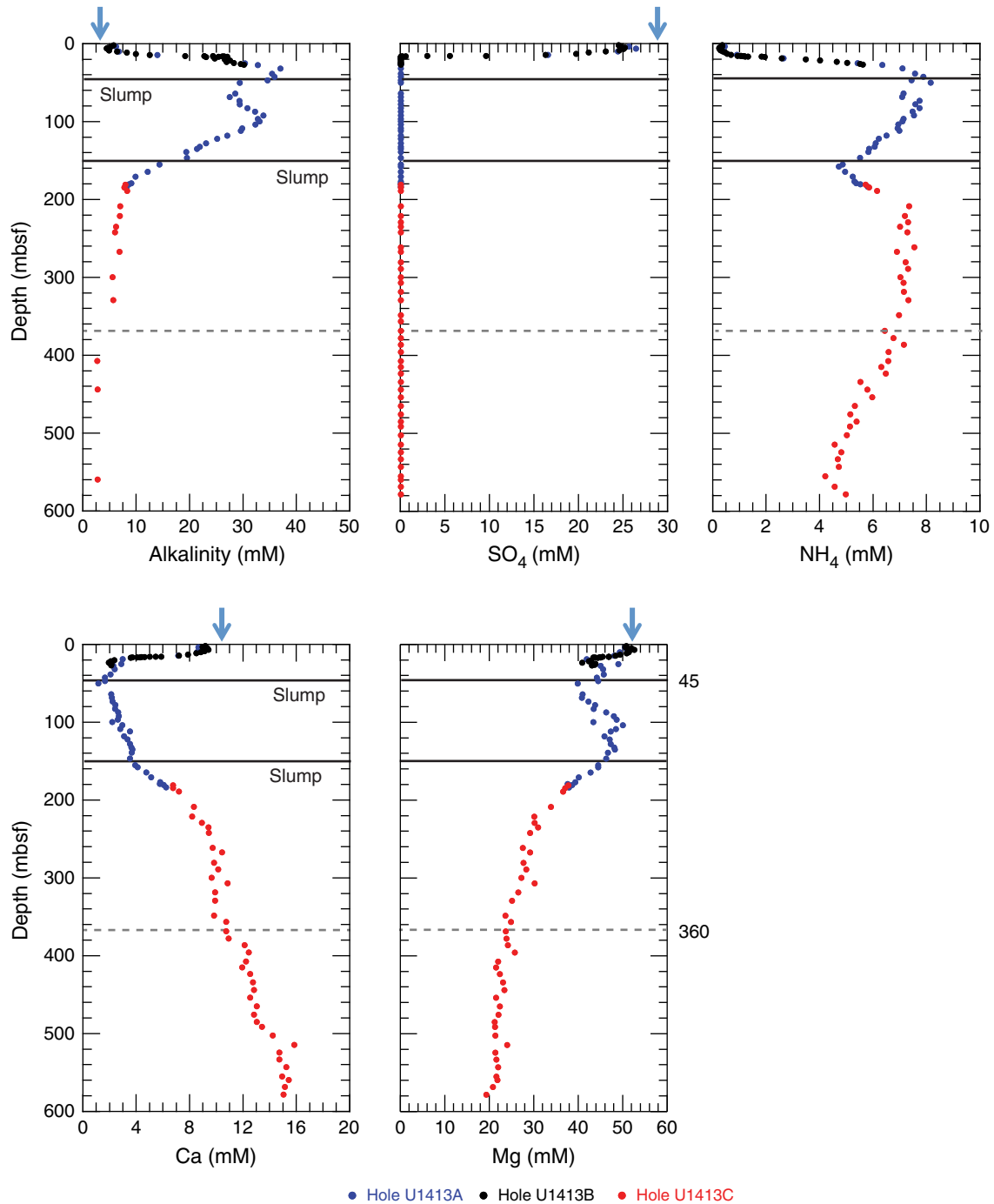


**Figure F21.** Downhole profiles for strontium, lithium, manganese, boron, silica, and barium, Site U1413. Dashed lines = lithostratigraphic unit boundaries. Solid lines = depths of slumps. Note that the slump at 44.6 mbsf also corresponds to the boundary between lithostratigraphic Units I and II. Blue arrows = bottom seawater values.

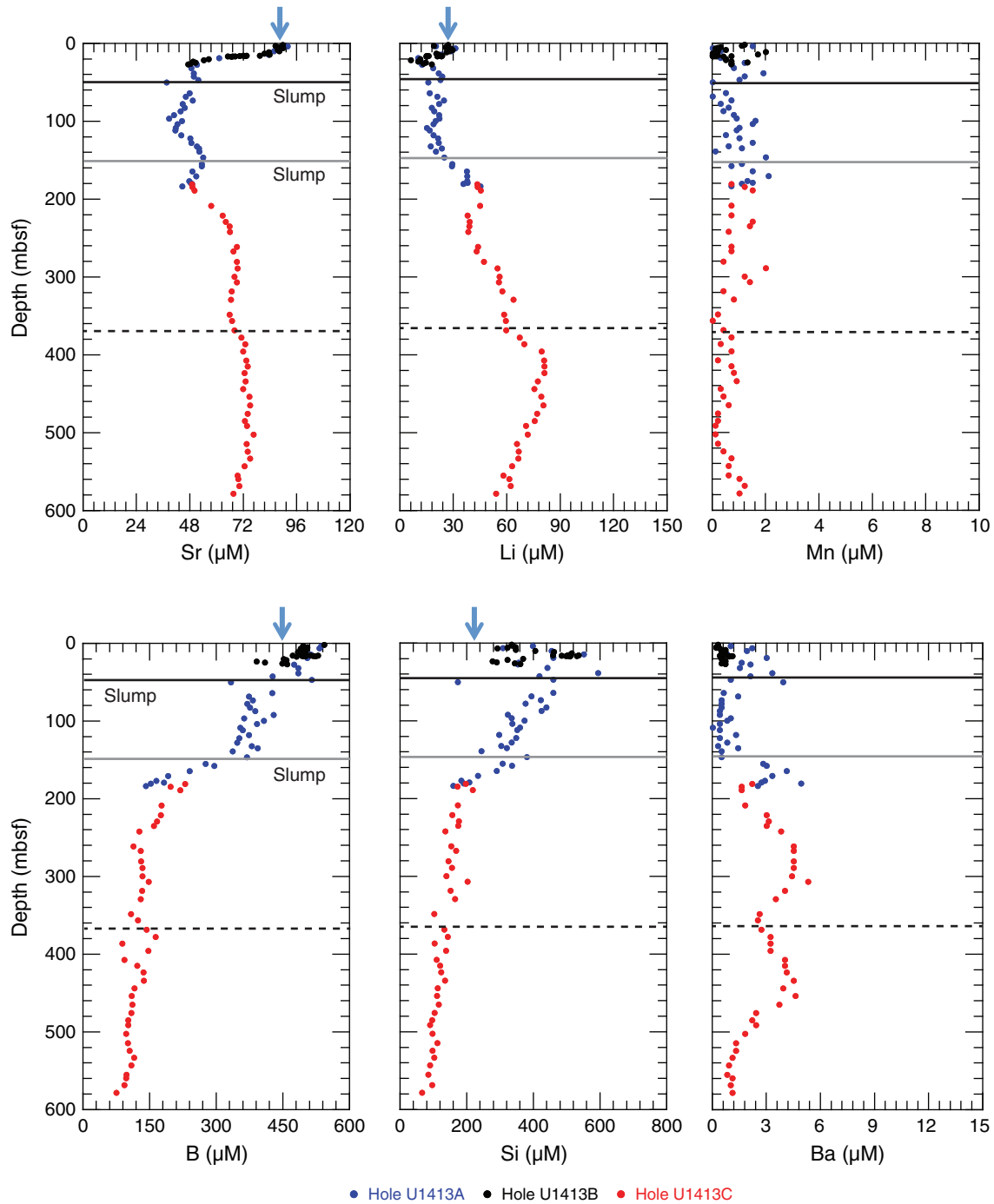


**Figure F22.** Downhole profiles of hydrocarbons and C<sub>1</sub>/C<sub>2+</sub> ratios in headspace gas samples, Site U1413. SMTZ = sulfate-methane transition zone. Dashed lines = lithostratigraphic unit boundaries. Note that the slump at 44.6 mbsf also corresponds to the boundary between lithostratigraphic Units I and II.

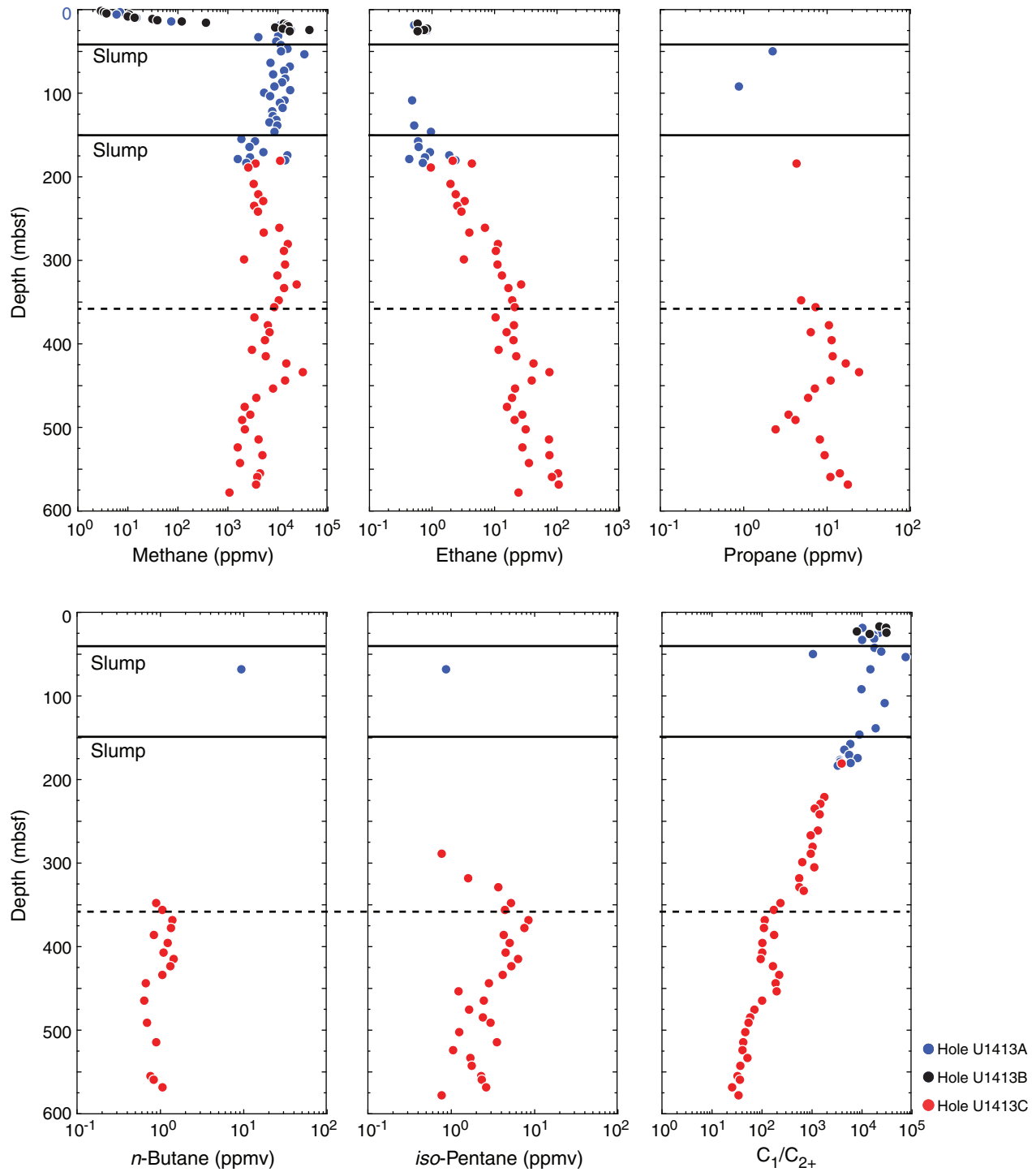




**Figure F23.** Downhole profiles of hydrocarbons, CO<sub>2</sub>, and C<sub>1</sub>/C<sub>2+</sub> ratios in void gas samples, Holes U1413A and U1413B. Solid line = lithostratigraphic unit boundary, which corresponds to the depth of a sediment slump.

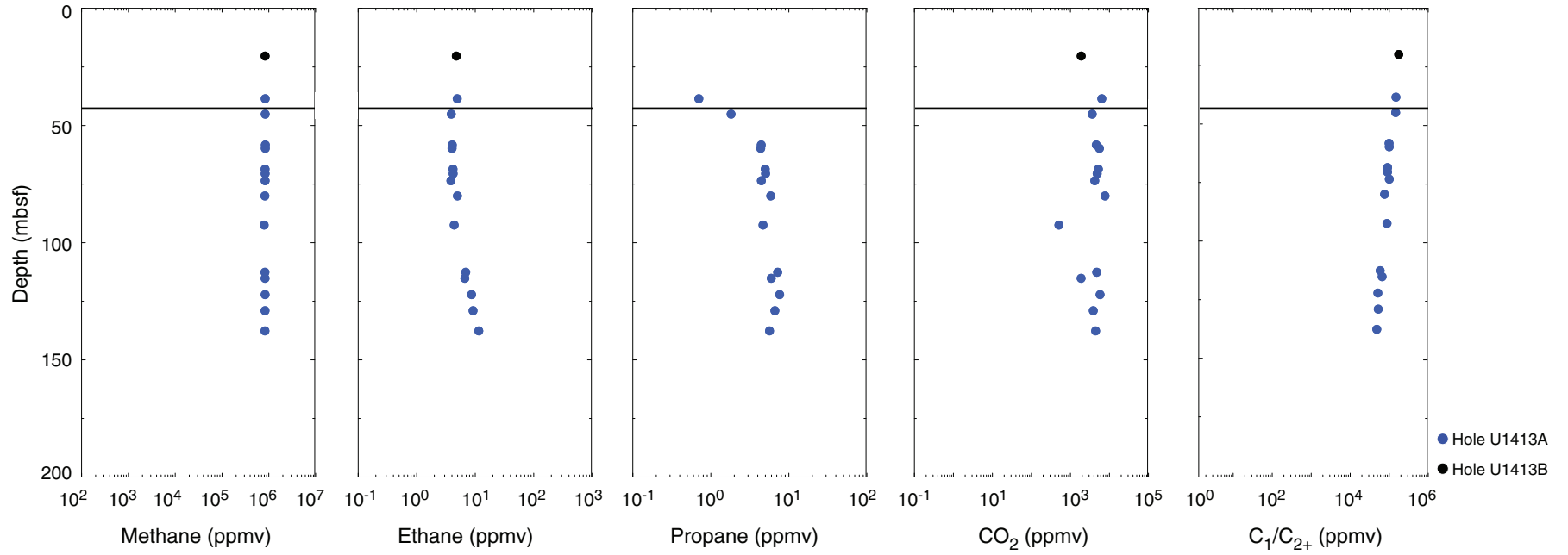


**Figure F24.** Downhole profiles of total carbon, inorganic carbon, total organic carbon, CaCO<sub>3</sub>, total nitrogen, and C/N ratio, Holes U1413A and U1413B. Solid lines denote the depths of sediment slumps. Note that the slump at 44.6 mbsf also corresponds to the boundary between lithostratigraphic Units I and II.

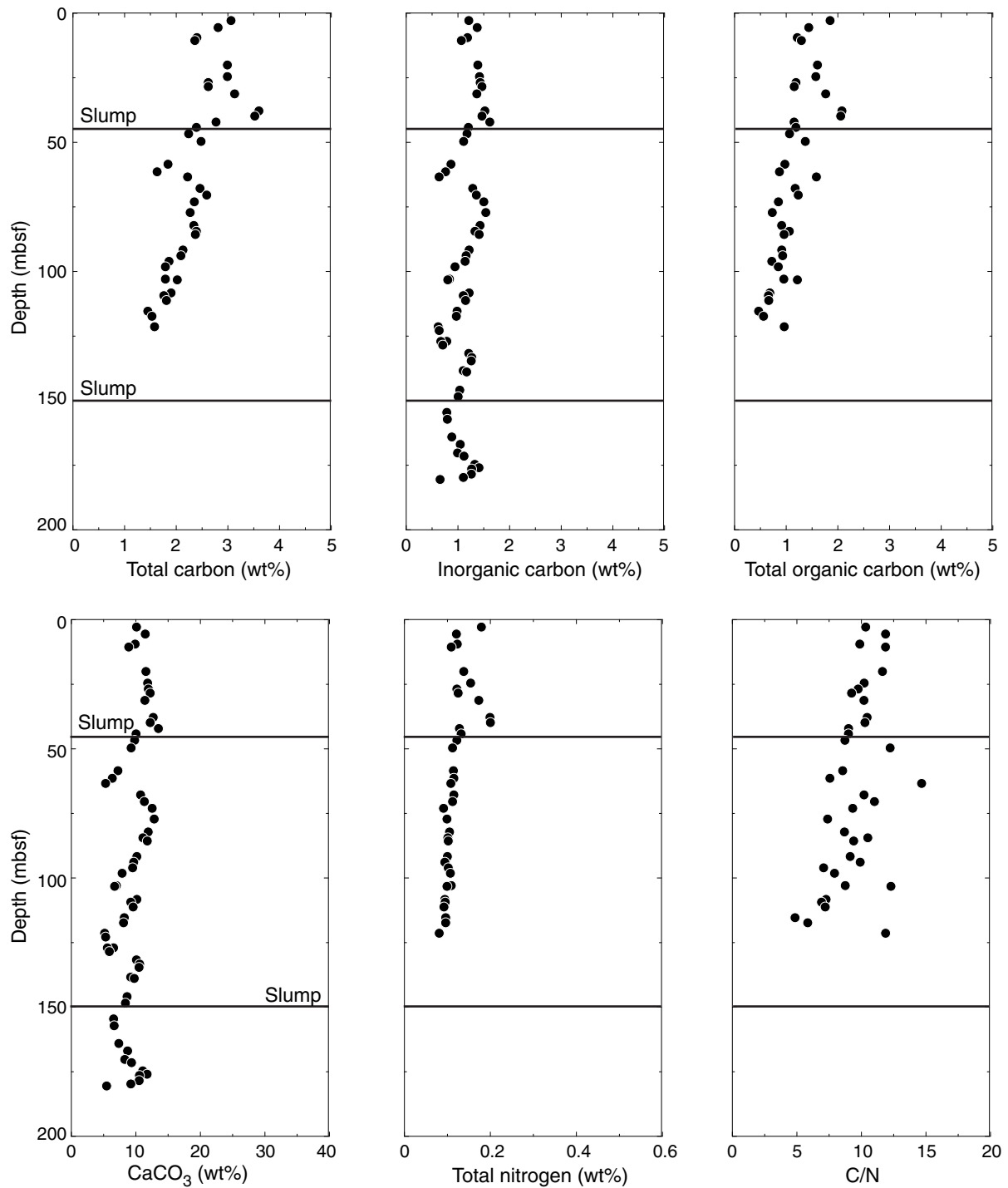


**Figure F25.** Gamma ray attenuation (GRA) density from the WRMSL and wet bulk density measured on discrete samples using moisture and density (MAD) mass/volume Method C, Site U1413. Horizontal lines = lithostratigraphic unit boundaries.

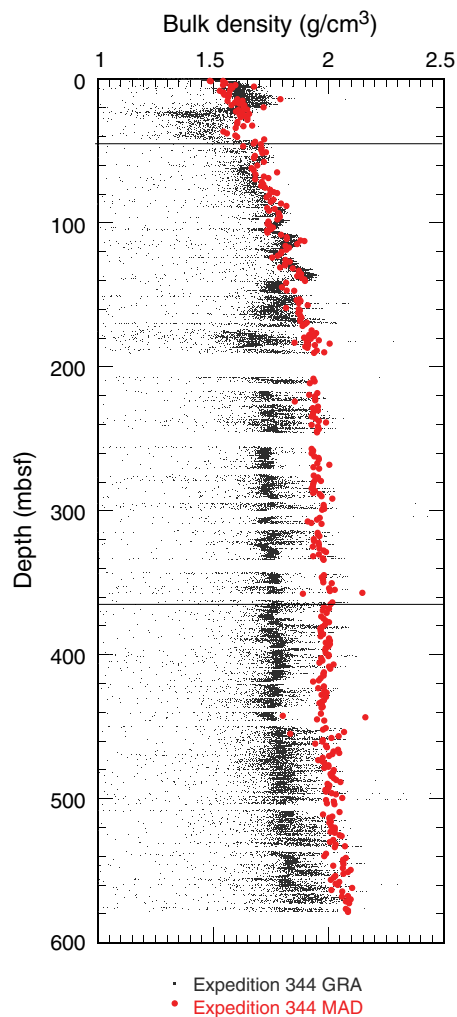
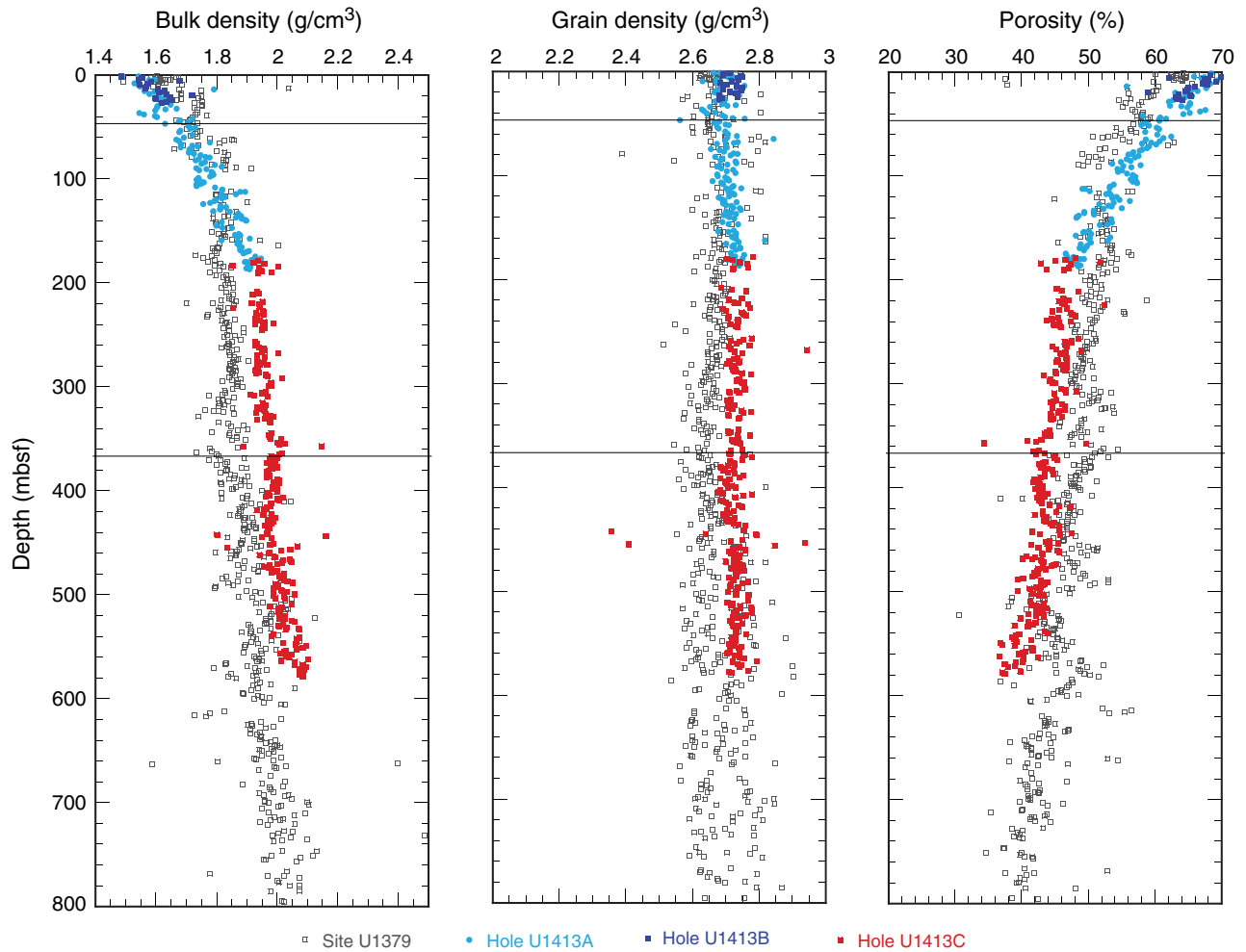
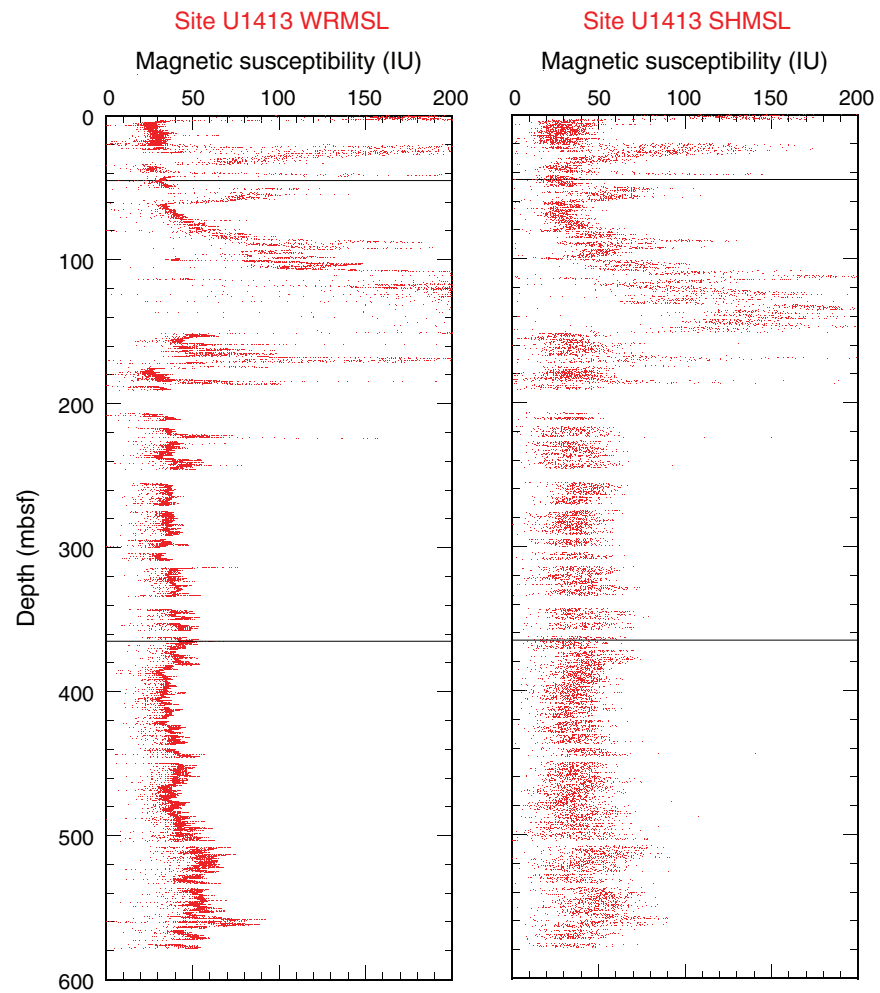


Figure F26. Data from discrete samples using the MAD mass/volume method. Horizontal lines = lithostratigraphic unit boundaries.



**Figure F27.** Magnetic susceptibility profiles for Site U1413. WRMSL = Whole-Round Multisensor Logger, SHMSL = Section Half Multisensor Logger. Horizontal lines = lithostratigraphic unit boundaries.



**Figure F28.** Natural gamma radiation (NGR) profiles, Sites U1413 and U1379. Horizontal lines = lithostratigraphic unit boundaries.

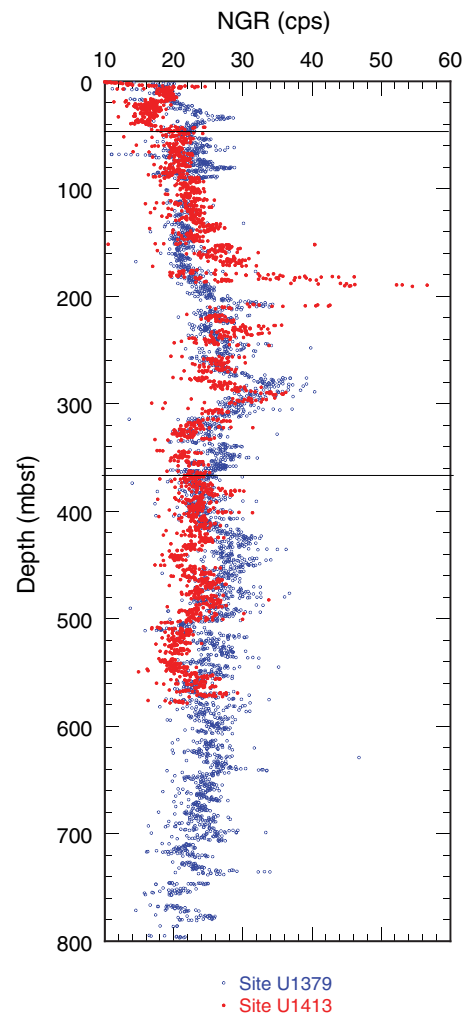


**Figure F29.** *P*-wave velocity measured on split cores, Sites U1413 and U1379. Horizontal lines = lithostratigraphic unit boundaries.

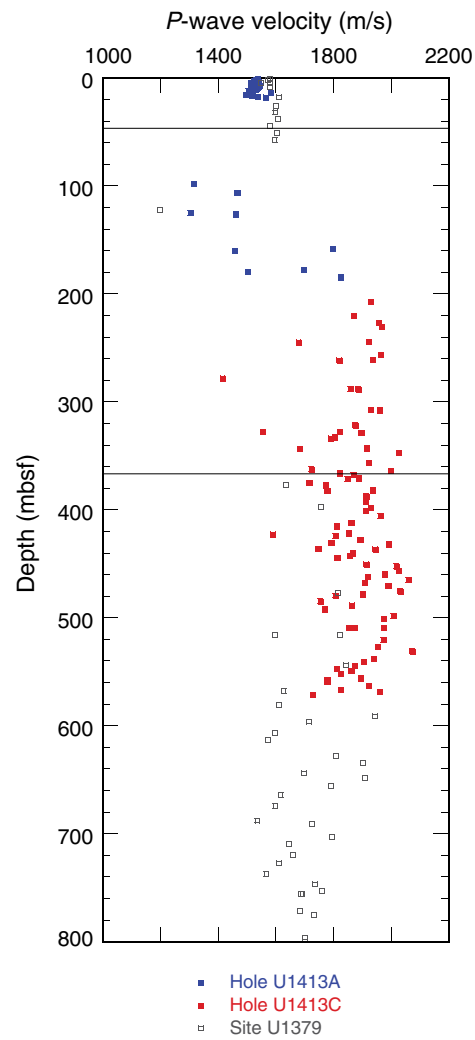


**Figure F30.** Thermal data, Sites U1379 and U1413. **A.** Thermal conductivity values showing best-fit line segments. **B.** Equilibrium temperatures (circles). Model 1 = estimated temperature based on two linear segments fitted to thermal conductivity, Model 2 = estimated temperatures based on measured thermal conductivity values. Horizontal lines = lithostratigraphic unit boundaries.

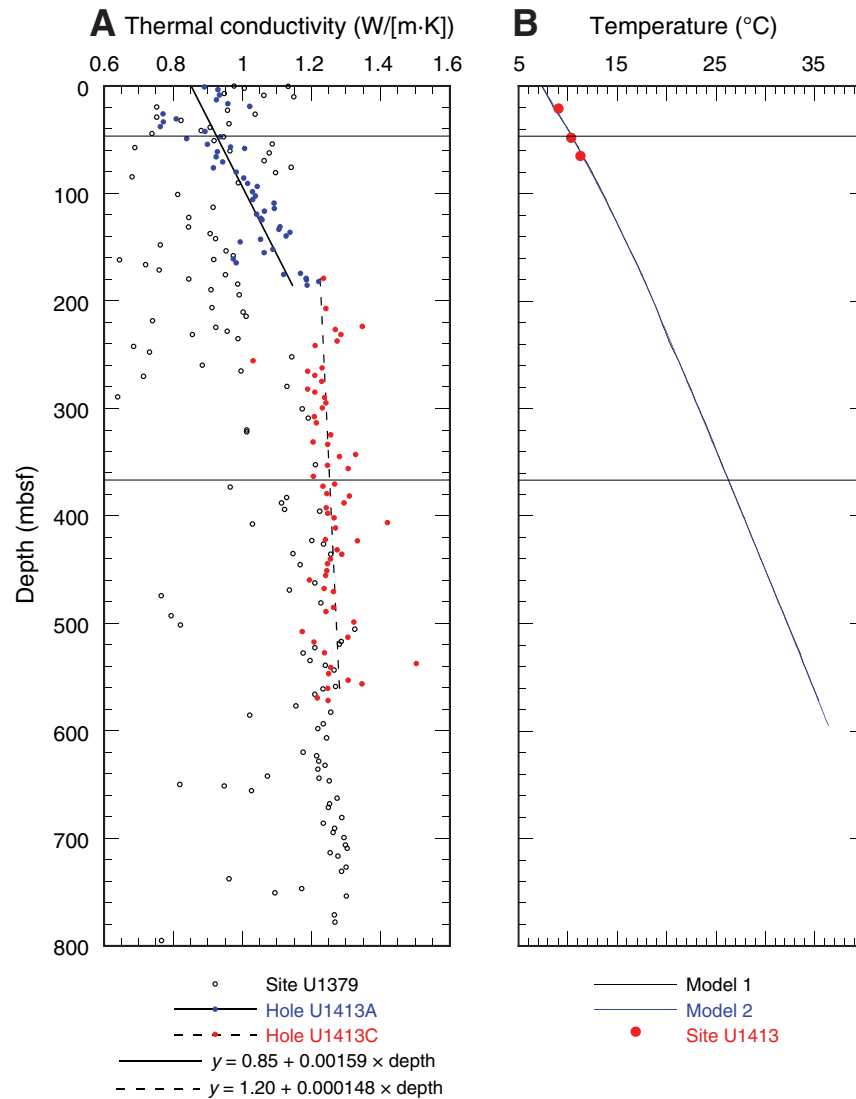


**Figure F31.** Strength data. **A.** Shear strength measured by automated vane shear, Sites U1413 and U1479. **B.** Compressive strength measured using pocket and needle penetrometers, Site U1413. Horizontal lines = lithostratigraphic unit boundaries.

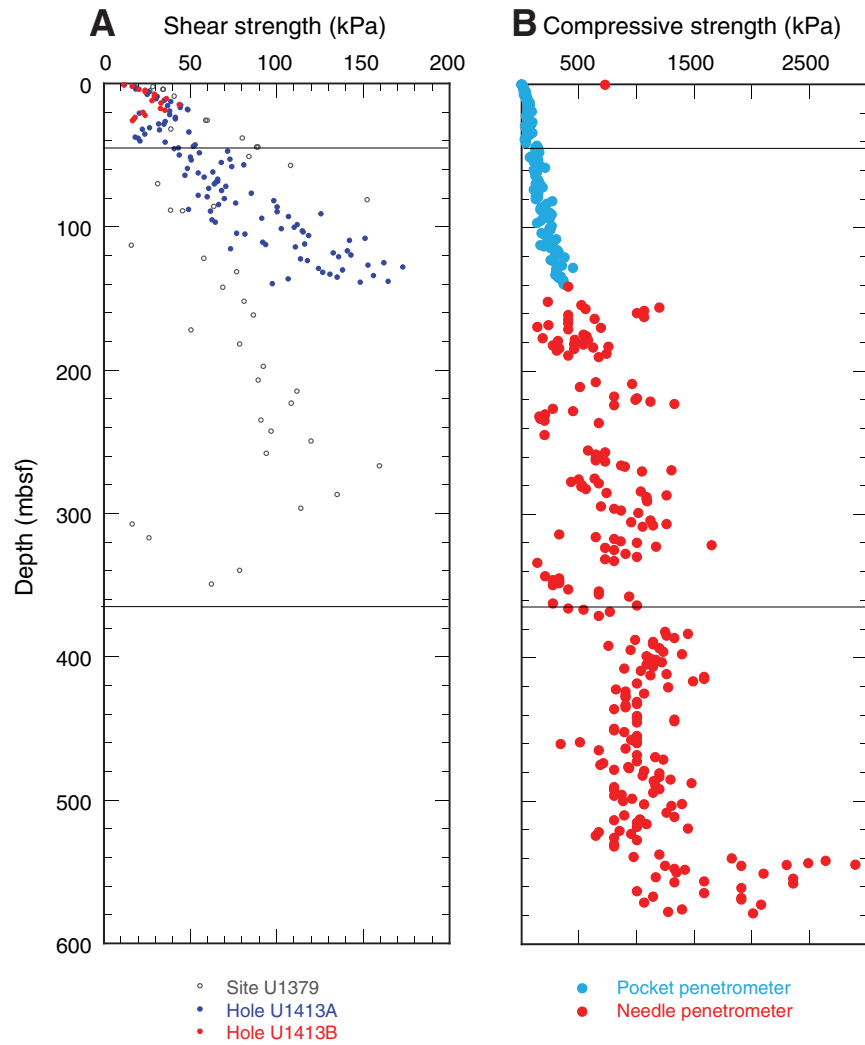
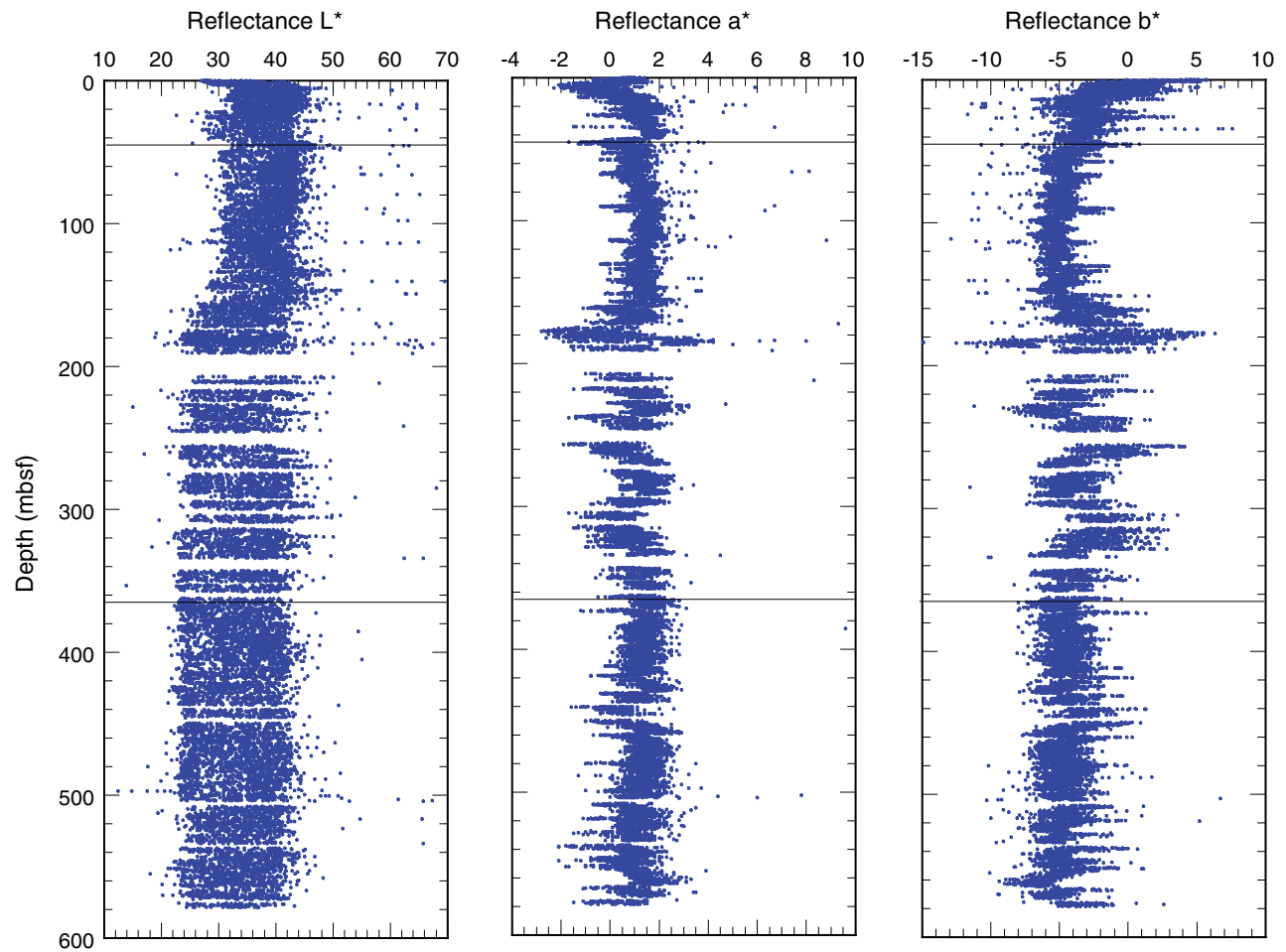


Figure F32. Reflectance  $L^*$ ,  $a^*$ , and  $b^*$  profiles, Site U1413. Horizontal lines = lithostratigraphic unit boundaries.



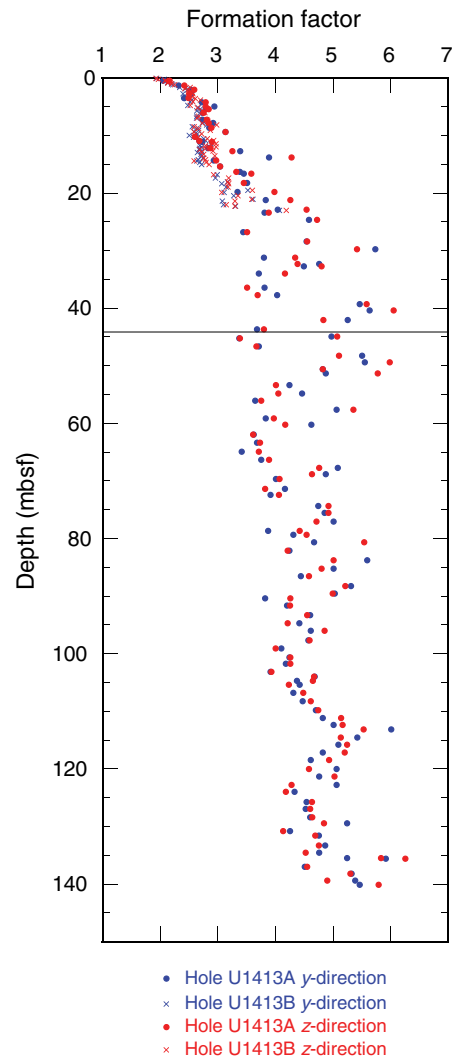
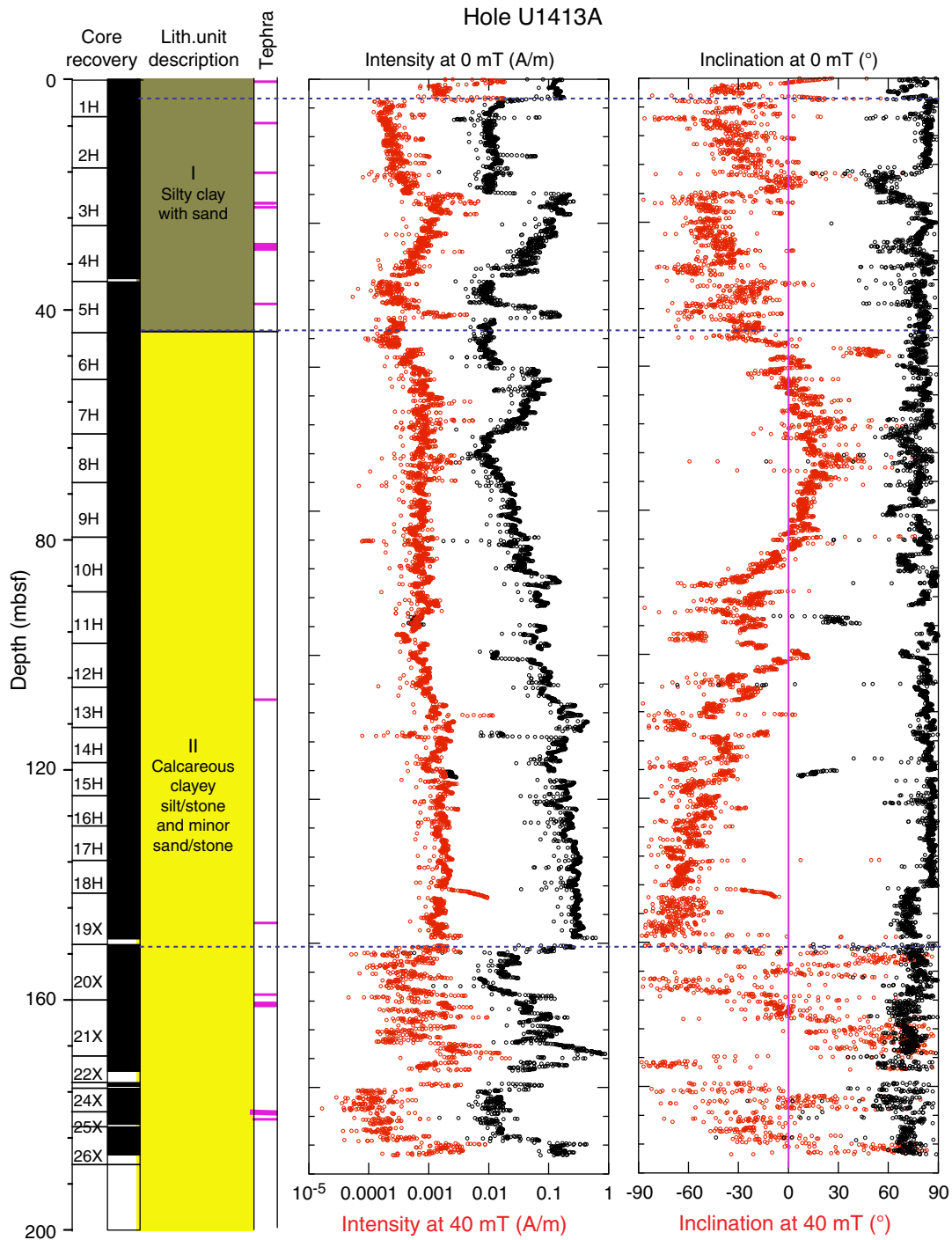
**Figure F33.** Formation factor calculated from electrical conductivity, Site U1413.

Figure F34. Paleomagnetic measurements on sediment archive-half sections, Hole U1413A. NRM intensity and inclination after 0 and 40 mT AF demagnetization.



**Figure F35.** Paleomagnetic measurements on sediment archive-half sections, Hole U1413B. NRM intensity and inclination after 0 and 40 mT AF demagnetization. Circled regions are data affected by the magnetic noise anomalies caused by magnetic flux jumps (see text).

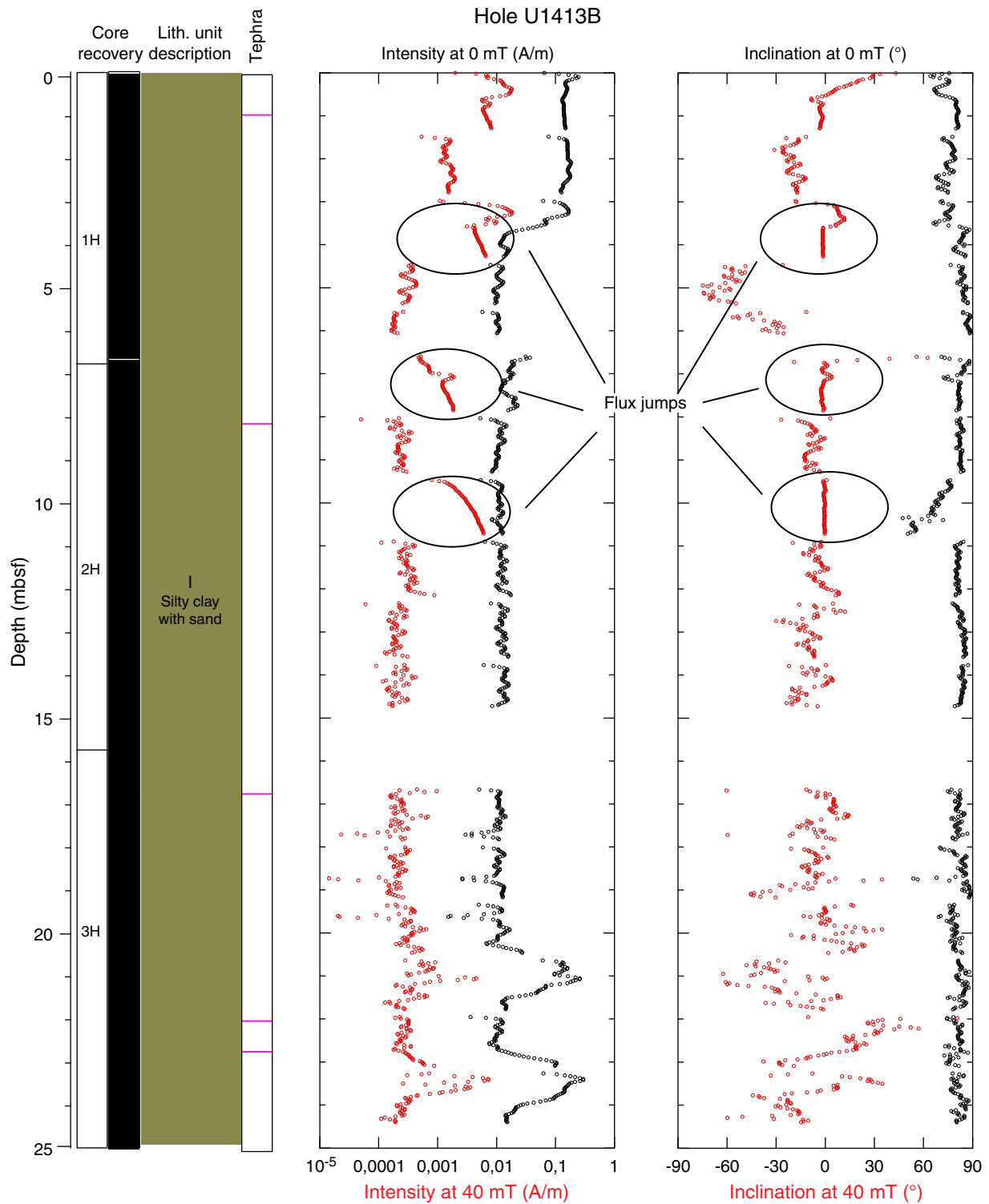
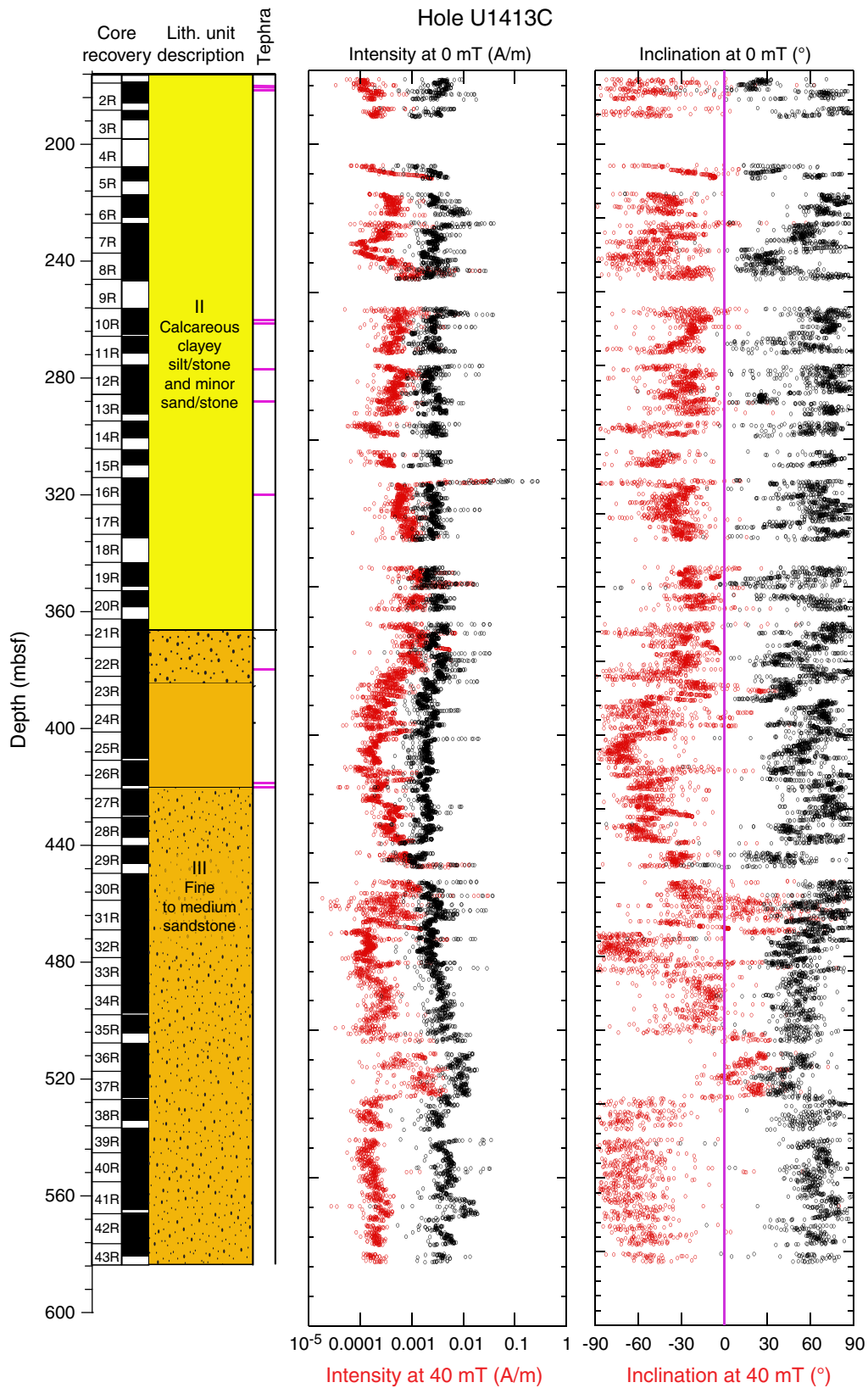
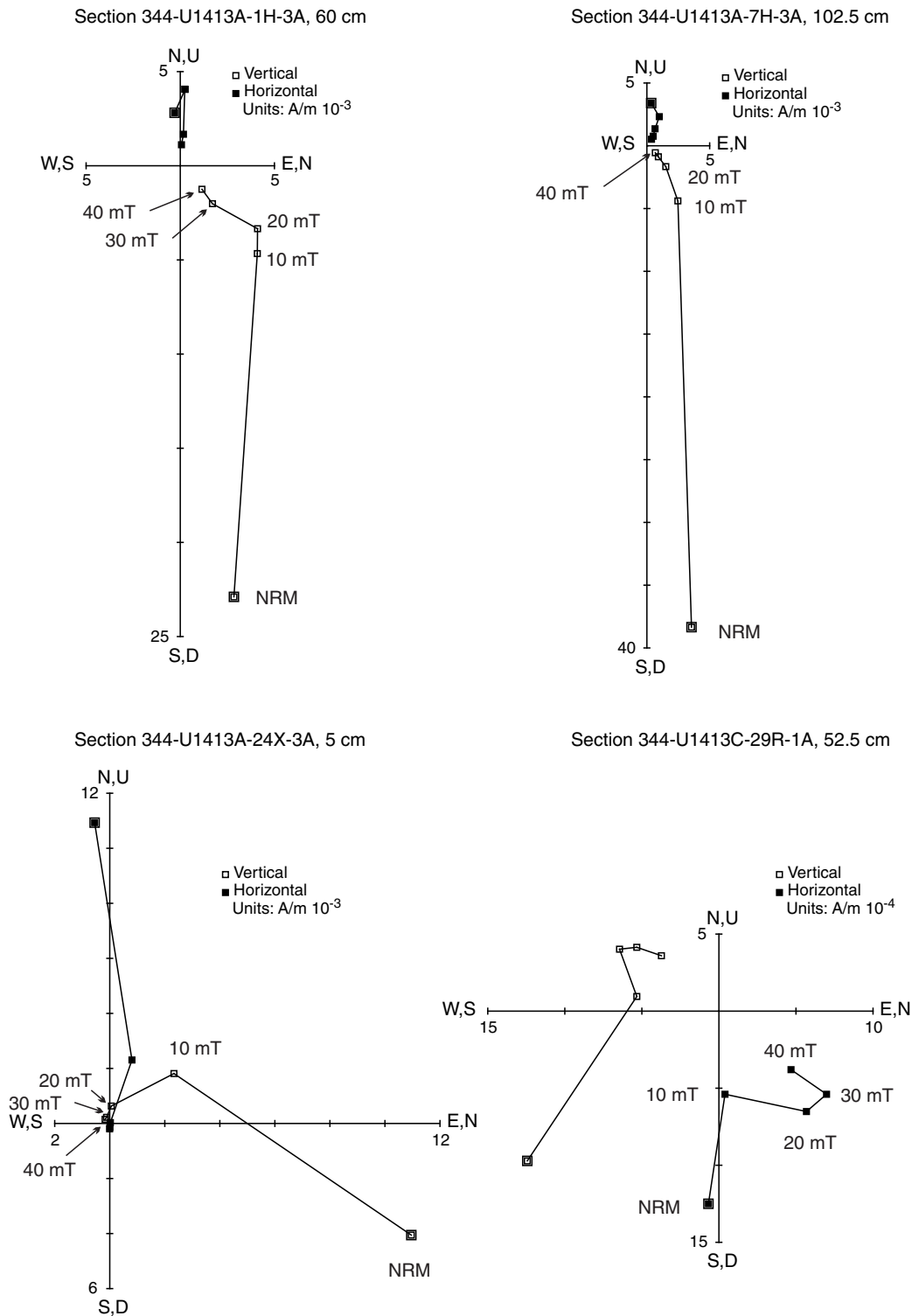


Figure F36. Paleomagnetic measurements on sediment archive-half sections, Hole U1413C. NRM intensity and inclination after 0 and 40 mT AF demagnetization.



**Figure F37.** Representative vector endpoint diagrams (Zijderveld, 1967) of stepwise AF demagnetization from pass-through section measurements. Open and solid squares = projection of the magnetization vector endpoints onto the vertical and horizontal planes, respectively. NRM = natural remanent magnetization.



**Figure F38.** Representative vector end-point diagrams (Zijderveld, 1967) of stepwise AF demagnetization from discrete sample measurements. Open and solid squares = projection of the magnetization vector end-points onto the vertical and horizontal planes, respectively. NRM = natural remanent magnetization. Blue lines = ChRM component derived by principal component analysis (Kirschvink, 1980).

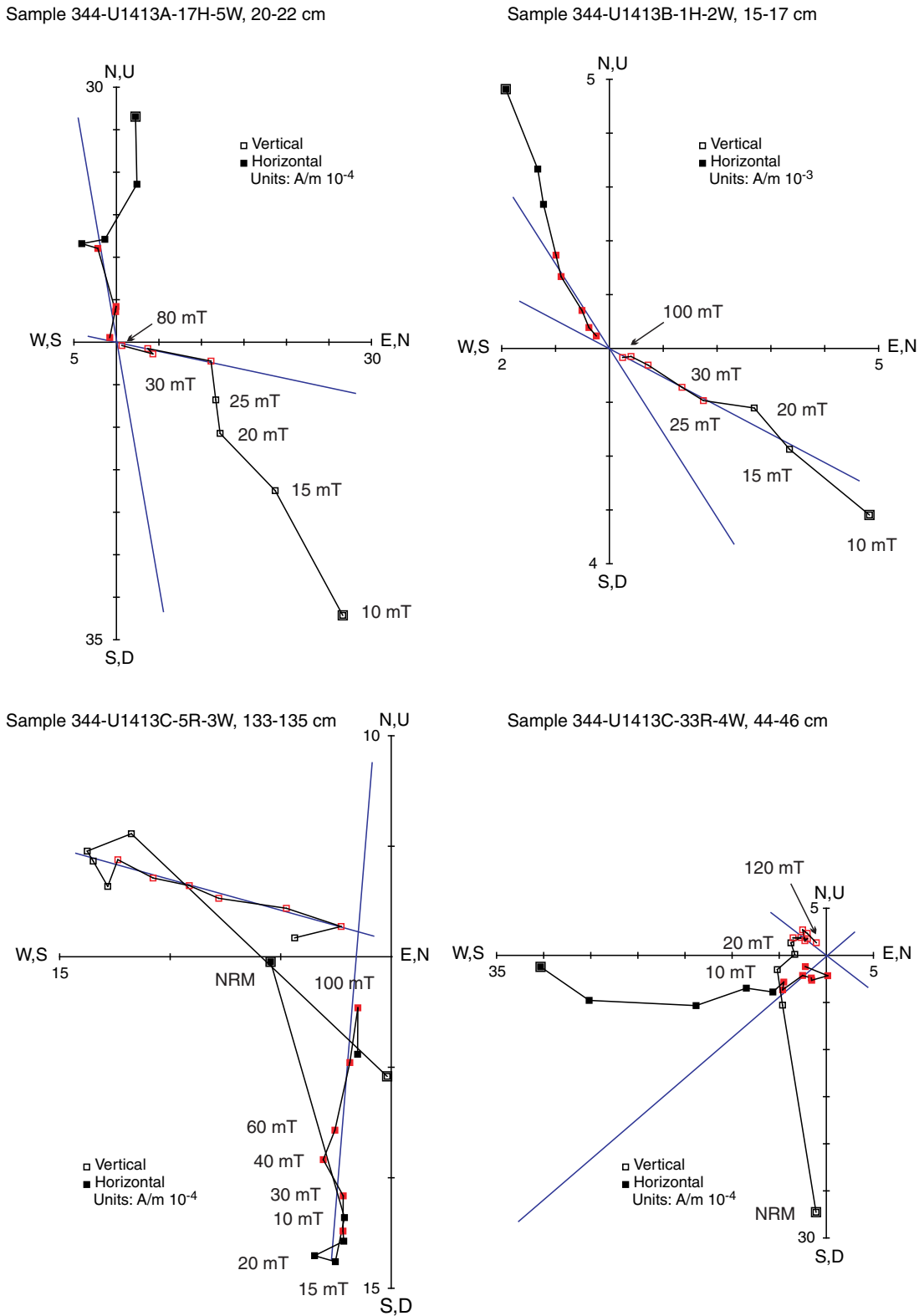




**Figure F40.** Wireline tool strings deployed in Hole U1413C. **A.** Triple combo. **B.** UBI. **C.** FMS. For information on tool acronyms, see the “**Methods**” chapter (Harris et al., 2013). LEH-MT = logging equipment head-mud temperature, EDTC = Enhanced Digital Telemetry Cartridge, HNGS = Hostile Environment Natural Gamma Ray Sonde, HLDS = Hostile Environment Litho-Density Sonde, DIT = Dual Induction Tool, UBI = Ultrasonic Borehole Imager, GPIT = General Purpose Inclinerometry Tool, FMS = Formation MicroScanner.

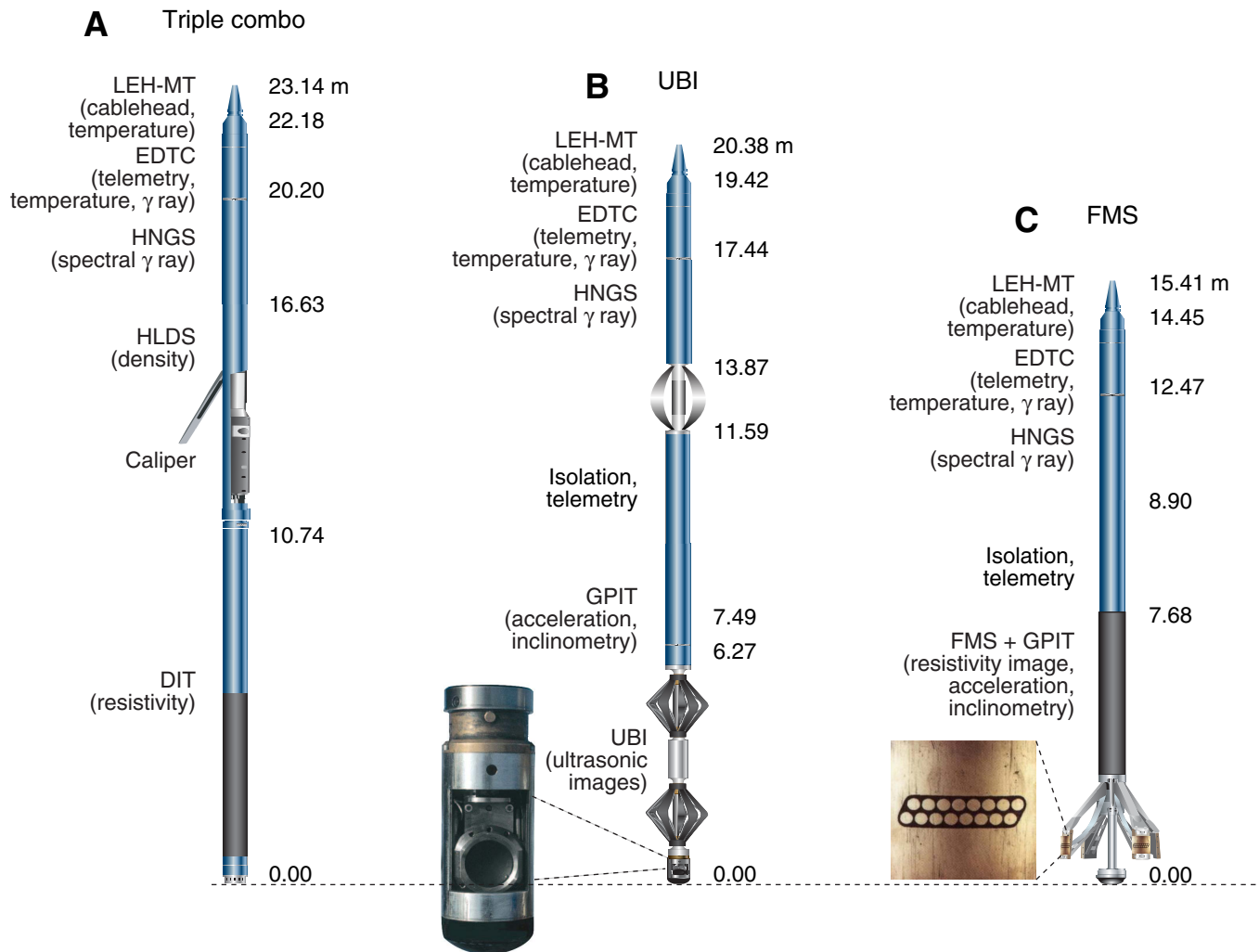


**Figure F41.** Caliper and total gamma ray logs, Hole U1413C. LCAL = hole diameter measured by the Hostile Environment Litho-Density Sonde (HLDS), C1 and C2 = hole diameters measured in orthogonal directions by the Formation MicroScanner (FMS), HSGR = total gamma ray curve measured by the Hostile Environment Natural Gamma Ray Sonde (HNGS) in the FMS and Ultrasonic Borehole Imager (UBI) tool strings, p1 = logging pass 1, p2 = logging pass 2. For more information on tool and curve descriptions, see the “Methods” chapter (Harris et al., 2013).

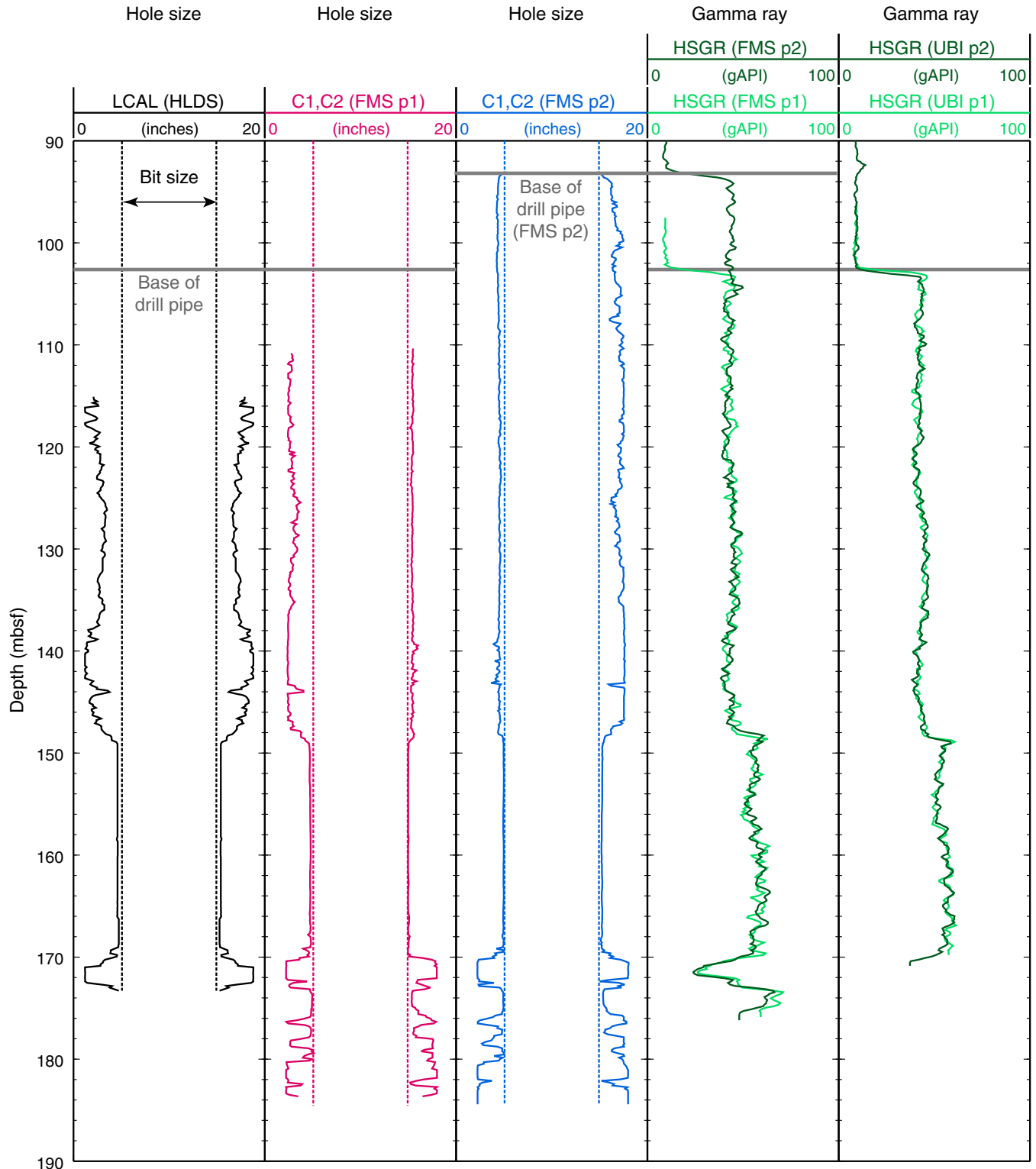


**Figure F42.** Summary of wireline log data, Hole U1413C. HSGR = total gamma ray, HURA = uranium content, NGR = natural gamma radiation from core measurements, HTHO = thorium content, HFK = potassium content, SFLU = spherically focused resistivity, IMPH = medium induction resistivity, UBI = Ultrasonic Borehole Imager tool. For more information on tool and curve descriptions, see the “Methods” chapter (Harris et al., 2013).

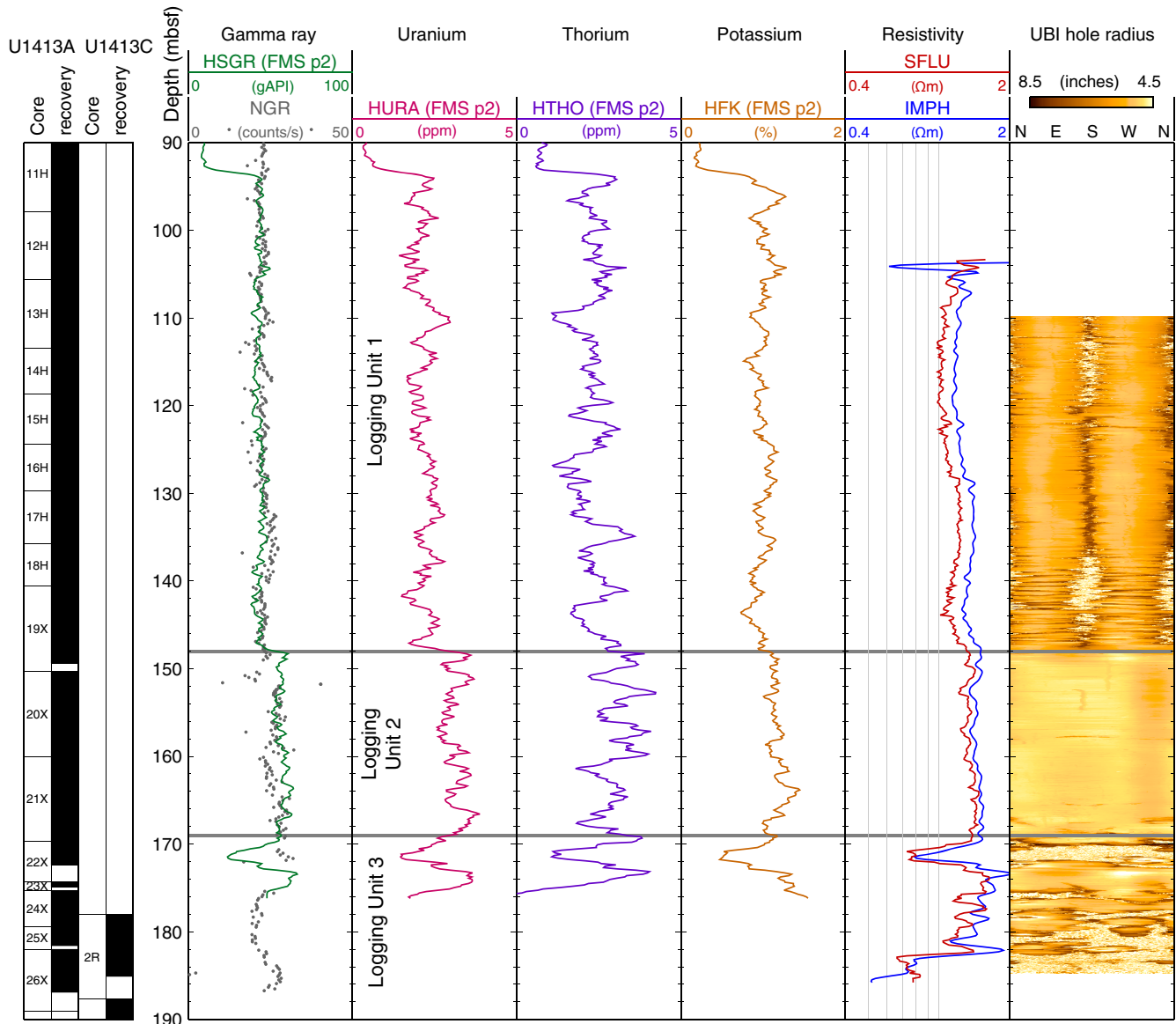


**Figure F43.** Summary of log images, Hole U1413C. The Formation MicroScanner (FMS) pad azimuth curve shows the orientation of the pair of caliper arms that measured the greater borehole diameter in the second pass of the FMS tool string. UBI = Ultrasonic Borehole Imager.

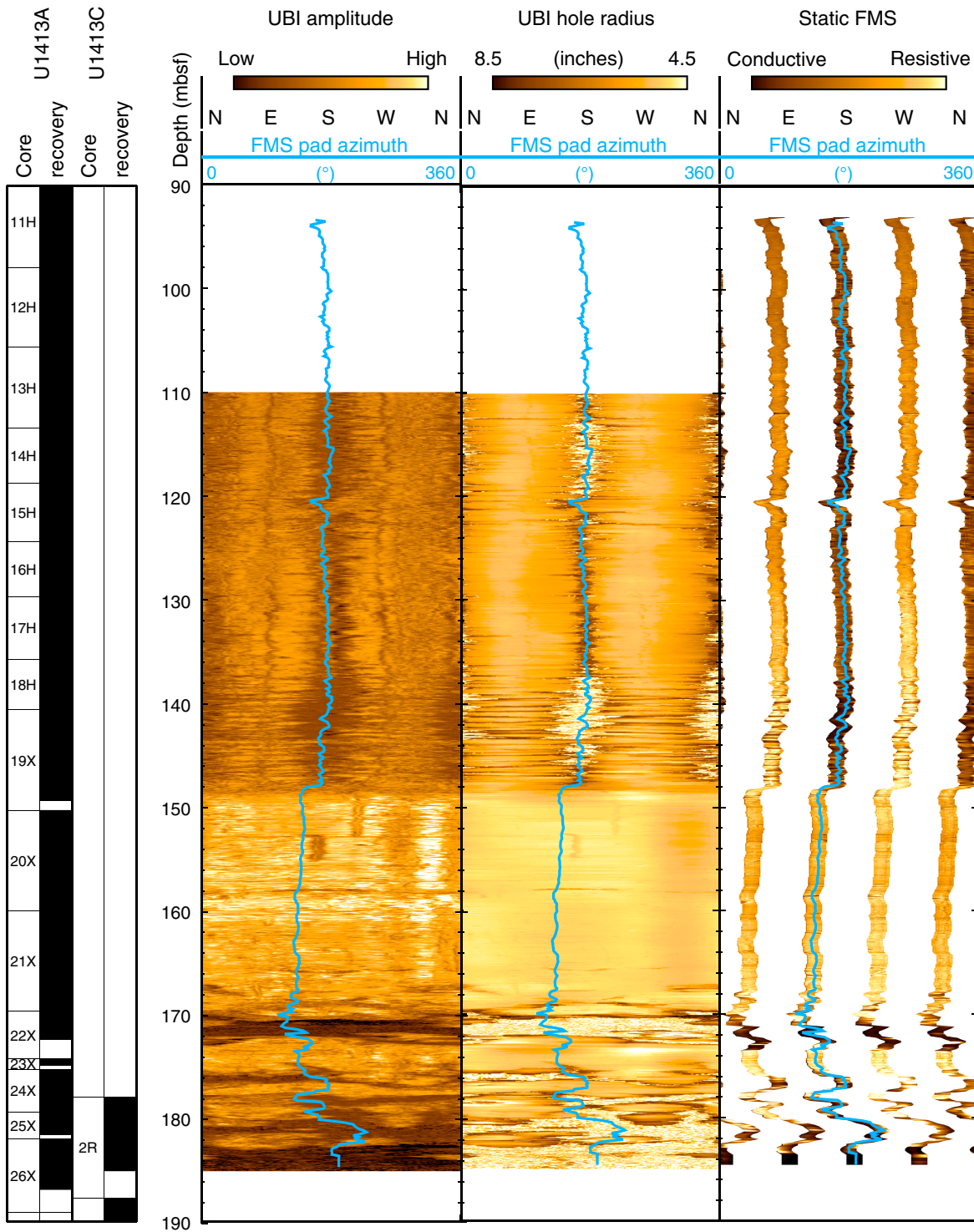


Table T1. Site U1413 coring summary. (Continued on next page.)

**Hole U1413A**

Latitude: 8°44.4593'N  
 Longitude: 84°6.8095'W  
 Time on hole (h): 48.5 (2.02 days)  
 Seafloor (drill pipe measurement from rig floor, m DRF): 550.9  
 Distance between rig floor and sea level (m): 11.0  
 Water depth (drill pipe measurement from sea level, m): 539.9  
 Total penetration (drilling depth below seafloor, m DSF): 189.1  
 Total length of cored section (m): 189.1  
 Total core recovered (m): 187.3  
 Core recovery (%): 99  
 Total number of cores: 26

**Hole U1413B**

Latitude: 8°44.4593'N  
 Longitude: 84°6.7992'W  
 Time on hole (h): 6.0 (0.25 days)  
 Seafloor (drill pipe measurement from rig floor, m DRF): 551.4  
 Distance between rig floor and sea level (m): 11.3  
 Water depth (drill pipe measurement from sea level, m): 540.4  
 Total penetration (drilling depth below seafloor, m DSF): 25.6  
 Total length of cored section (m): 25.6  
 Total core recovered (m): 27.4  
 Core recovery (%): 107  
 Total number of cores: 3

**Hole U1413C**

Latitude: 8°44.4482'N  
 Longitude: 84°6.7993'W  
 Time on hole (h): 115.93 (4.83 days)  
 Seafloor (drill pipe measurement from rig floor, m DRF): 551.4  
 Distance between rig floor and sea level (m): 11.3  
 Water depth (drill pipe measurement from sea level, m): 540.4  
 Total penetration (drilling depth below seafloor, m DSF): 582.2  
 Total length of cored section (m): 404.2  
 Total core recovered (m): 313.9  
 Core recovery (%): 78  
 Total number of cores: 42

Core	Date (2012)	Time UTC (h)	Depth DSF (m)			Depth CSF (m)		Length of core recovered (m)	Recovery (%)	Comments
			Top of cored interval	Bottom of cored interval	Interval advanced (m)	Top of cored interval	Bottom of cored interval			
344-U1413A-										
1H	Nov 24	1245	0.00	6.60	6.6	0.00	6.65	6.65	101	FlexIt
2H	Nov 24	1340	6.60	16.10	9.5	6.60	16.64	10.04	106	FlexIt
3H	Nov 24	1435	16.10	25.60	9.5	16.10	25.94	9.84	104	FlexIt, APCT-3
4H	Nov 24	1520	25.60	35.10	9.5	25.60	34.57	9.05	95	FlexIt
5H	Nov 24	1615	35.10	44.60	9.5	35.10	45.46	10.36	109	FlexIt, APCT-3
6H	Nov 24	1715	44.60	52.00	7.4	44.60	52.06	7.46	101	FlexIt, APCT-3
7H	Nov 24	2220	52.00	60.90	8.9	52.00	60.95	8.95	101	FlexIt, APCT-3
8H	Nov 25	0400	60.90	70.00	9.1	60.90	70.00	9.10	100	FlexIt, APCT-3
9H	Nov 25	0500	70.00	79.50	9.5	70.00	79.71	9.71	102	FlexIt
10H	Nov 25	0605	79.50	89.00	9.5	79.50	89.88	10.38	109	FlexIt
11H	Nov 25	0705	89.00	97.90	8.9	89.00	97.97	8.97	101	FlexIt
12H	Nov 25	0750	97.90	105.60	7.7	97.90	105.67	7.77	101	FlexIt
13H	Nov 25	0845	105.60	113.40	7.8	105.60	113.49	7.89	101	FlexIt
14H	Nov 25	0935	113.40	118.70	5.3	113.40	118.77	5.37	101	FlexIt
15H	Nov 25	1030	118.70	124.40	5.7	118.70	124.44	5.74	101	FlexIt
16H	Nov 25	1110	124.40	129.70	5.3	124.40	129.78	5.38	102	FlexIt
17H	Nov 25	1200	129.70	135.70	6.0	129.70	135.72	6.02	100	FlexIt
18H	Nov 25	1250	135.70	140.60	4.9	135.70	140.60	4.90	100	FlexIt
19X	Nov 25	1510	140.60	150.30	9.7	140.60	149.36	8.76	90	
20X	Nov 25	1640	150.30	160.00	9.7	150.30	160.16	9.86	102	
21X	Nov 25	1840	160.00	169.70	9.7	160.00	169.92	9.92	102	
22X	Nov 25	2030	169.70	174.30	4.6	169.70	172.37	2.67	58	
23X	Nov 25	2200	174.30	175.30	1.0	174.30	174.92	0.62	62	
24X	Nov 26	0010	175.30	179.40	4.1	175.30	180.06	4.76	116	
25X	Nov 26	0205	179.40	182.00	2.6	179.40	181.60	2.20	85	
26X	Nov 26	0405	182.00	189.10	7.1	182.00	186.91	4.91	69	
Hole U1413A totals:					189.1			187.28	99	

Table T1 (continued).

Core	Date (2012)	Time UTC (h)	Depth DSF (m)			Depth CSF (m)		Length of core recovered (m)	Recovery (%)	Comments
			Top of cored interval	Bottom of cored interval	Interval advanced (m)	Top of cored interval	Bottom of cored interval			
344-U1413B-										
1H	Nov 26	0705	0.00	6.60	6.6	0.00	6.65	6.65	101	
2H	Nov 26	0730	6.60	16.10	9.5	6.60	16.54	9.94	105	
3H	Nov 26	0800	16.10	25.60	9.5	16.10	26.95	10.85	114	
Hole U1413B totals:					25.6			27.44	107	
344-U1413C-										
11			*****Drilled from 0.0 to 178.0 m DSF*****							
2R	Nov 27	0520	178.00	187.70	9.7	178.00	185.10	7.10	73	
3R	Nov 27	0650	187.70	197.40	9.7	187.70	190.86	3.16	33	
4R	Nov 27	0840	197.40	207.10	9.7	197.40	197.50	0.10	1	
5R	Nov 27	1025	207.10	216.80	9.7	207.10	211.76	4.66	48	
6R	Nov 27	1130	216.80	226.50	9.7	216.80	224.09	7.29	75	
7R	Nov 27	1250	226.50	236.20	9.7	226.50	236.38	9.88	102	
8R	Nov 27	1415	236.20	245.90	9.7	236.20	246.06	9.86	102	
9R	Nov 27	1540	245.90	255.60	9.7	245.90	255.76	0.00	0	
10R	Nov 27	1640	255.60	265.30	9.7	255.60	264.39	8.79	91	
11R	Nov 27	1745	265.30	275.00	9.7	265.30	270.90	5.60	58	
12R	Nov 27	1905	275.00	284.70	9.7	275.00	285.04	10.04	104	
13R	Nov 27	2020	284.70	294.40	9.7	284.70	291.71	7.01	72	
14R	Nov 27	2205	294.40	304.10	9.7	294.40	299.97	5.57	57	
15R	Nov 27	2340	304.10	313.80	9.7	304.10	309.20	5.10	53	
16R	Nov 28	0125	313.80	323.50	9.7	313.80	323.59	9.79	101	
17R	Nov 28	0245	323.50	333.20	9.7	323.50	333.43	9.93	102	
18R	Nov 28	0355	333.20	342.90	9.7	333.20	334.28	1.08	11	
19R	Nov 28	0530	342.90	352.60	9.7	342.90	350.77	7.87	81	
20R	Nov 28	0725	352.60	362.30	9.7	352.60	357.91	5.31	55	
21R	Nov 28	0905	362.30	372.00	9.7	362.30	371.39	9.09	94	
22R	Nov 28	1020	372.00	381.70	9.7	372.00	381.98	9.98	103	
23R	Nov 28	1150	381.70	391.40	9.7	381.70	391.76	10.06	104	
24R	Nov 28	1315	391.40	401.10	9.7	391.40	401.51	10.11	104	
25R	Nov 28	1455	401.10	410.80	9.7	401.10	409.88	8.78	91	
26R	Nov 28	1610	410.80	420.50	9.7	410.80	419.19	8.39	86	
27R	Nov 28	1730	420.50	430.20	9.7	420.50	429.36	8.86	91	
28R	Nov 28	1845	430.20	439.90	9.7	430.20	437.03	6.83	70	
29R	Nov 28	2020	439.90	449.60	9.7	439.90	445.95	6.05	62	
30R	Nov 28	2230	449.60	459.30	9.7	449.60	459.47	9.87	102	
31R	Nov 29	0015	459.30	469.00	9.7	459.30	469.24	9.94	102	
32R	Nov 29	0150	469.00	478.70	9.7	469.00	478.78	9.78	101	
33R	Nov 29	0310	478.70	488.40	9.7	478.70	488.61	9.91	102	
34R	Nov 29	0440	488.40	498.10	9.7	488.40	497.32	8.92	92	
35R	Nov 29	0555	498.10	507.80	9.7	498.10	504.18	6.08	63	
36R	Nov 29	0735	507.80	517.50	9.7	507.80	516.95	9.15	94	
37R	Nov 29	0900	517.50	527.20	9.7	517.50	526.22	8.72	90	
38R	Nov 29	1035	527.20	536.90	9.7	527.20	533.99	6.79	70	
39R	Nov 29	1210	536.90	546.60	9.7	536.90	546.73	9.83	101	
40R	Nov 29	1350	546.60	556.30	9.7	546.60	556.55	9.95	103	
41R	Nov 29	1535	556.30	566.00	9.7	556.30	564.74	8.44	87	
42R	Nov 29	1725	566.00	575.70	9.7	566.00	573.13	7.13	74	
43R	Nov 29	1945	575.70	582.20	6.5	575.70	578.84	3.14	48	
Hole U1413C totals:					582.2			313.94	78	
Site U1413 totals:					796.90			528.60		

DSF = drilling depth below seafloor, CSF = core depth below seafloor. H = advanced piston corer core, X = extended core barrel core, R = rotary core barrel core, numeric core type = drilled interval. APCT-3 = advanced piston corer temperature tool.

**Table T2.** Summary of Site U1413 lithologic units.

Unit	Top depth (mbsf)	Hole, core, section, interval (cm)	Bottom depth (mbsf)	Hole, core, section, interval (cm)	Unit thickness (m)	Major lithology
I	0	344- U1413A-1H-1, 0	44.60	344- U1413A-6H-1, 0	44.60	Silty clay and sand
II	44.60	U1413A-6H-1, 0	366.45	U1413C-21R-3, 117	321.85	Calcareous clayey silt/stone and minor sand/stone
III	366.45	U1413C-21R-3, 117	578.84	U1413C-43R-CC, 20	212.39	Fine to medium sandstone and siltstone



Table T3. Calcareous nannofossil faunal distribution, Site U1413. (Continued on next page.)

Core, section, interval (cm)	Depth (mbsf)		Preservation	Group abundance	Calcidiscus leptoporus	Calcispheres	Ceratolithus cristatus	Ceratolithus cristatus (rugosus)	Coccolithus pelagicus	Emiliania huxleyi	Cephyrocapsa (<4 µm)	Cephyrocapsa (>4 µm)	Cephyrocapsa caribbeanica	Cephyrocapsa oceanica	Helicosphaera carteri	Helicosphaera hyalina	Helicosphaera inversa	Helicosphaera neogranulata	Helicosphaera pavementum	Helicosphaera sellii	Helicosphaera sp.	Helicosphaera spp.	Pontosphaera discopora	Pontosphaera japonica	Pseudoemiliania lacunosa	Rhabdosphaera clavigera	Syracosphaera pulchra	Umbilicosphaera sibogae	
	Top	Bottom																											
344-U1413A-																													
1H-CC, 0-5	6.59	6.64	G	C	C						C	C	C	C	C	C					C						R	R	
2H-CC, 0-5	16.58	16.63	G	A	C					R	C	A	C	C	C	C					C					R	R	R	
3H-CC, 0-5	25.86	25.91	G	C	Freq	C		R		R	Freq	Freq	Freq	Freq	C	C					A					R			
4H-CC, 0-5	34.18	34.23	G	A	C	C				Freq	C	A	C	C	Freq		R				C		Freq						
5H-CC, 0-5	45.38	45.43	M	F	Freq	Freq	R	R		Freq	Freq	C	Freq	Freq	R		R				C					Freq	R		
6H-CC, 0-5	51.99	52.04	M	F	R		R	R		Freq	C	C	C	C							C								
7H-CC, 0-5	60.90	60.95	G	C	Freq						C	Freq	Freq	Freq							C							R	
8H-CC, 0-5	69.95	70.00	G	C	R						C	C	C	C	R						C					Freq	R		
9H-CC, 0-5	79.66	79.71	M	R						Freq	Freq	C	C	C							C								
10H-CC, 0-5	89.78	89.83	G	C						Freq	C	C	C	C					R		C								
11H-CC, 0-5	97.91	97.96	M	F	R						C	C	C	C	Freq			R	Freq		C					R	R	R	
12H-CC, 0-5	105.55	105.60	G	F						R	C	C	C	C	Freq				R		C					R			
13H-CC, 0-5	113.44	113.49	M	F	Freq						C	C	Freq	C	R						C								
14H-CC, 0-5	118.69	118.74	M	F						R	C	C	Freq	C	Freq						C								
15H-CC, 0-5	124.39	124.44	P	F	Freq						C	C	Freq	C				R			C						R		
16H-CC, 0-5	129.73	129.78	M	F	R						C	C	C	C	R						C	R						R	
17H-CC, 0-5	135.64	135.69	G	F		Freq					C	C	Freq	C	Freq		R				C					R	R		
18H-CC, 0-5	140.48	140.53	M	F		R					C	C	Freq	C	Freq		Freq				C					R			
19X-CC, 0-5	149.28	149.33	M	C	Freq						A	C	C	C	Freq						C	R							
20X-CC, 0-5	160.08	160.13	M	R				R			C										Freq			Freq					
21X-CC, 0-5	169.85	169.90	M	R	Freq						C										C	R							
22X-CC, 0-5	172.32	172.37	M	R	Freq	Freq					C				C						C					R			
23X-CC, 0-5	174.87	174.92	M	R	Freq	Freq					C				R						C					R		R	
24X-CC, 0-5	179.97	180.02	M	R	Freq						C	Freq		Freq							R					C	R		
25X-CC, 0-5	181.51	181.56	M	R	Freq						Freq	Freq		Freq			R				Freq					C			
26X-CC, 0-5	186.86	186.91	M	R	R						Freq										Freq	R				C			
344-U1413B-																													
1H-CC, 0-5	6.30	6.35	G	A	Freq	R					C	C		C							C					Freq	Freq		
2H-CC, 0-5	16.46	16.51	G	C	R					R	A			C							C							Freq	
3H-CC, 0-5	26.77	26.82	G	C	R					Freq	A	C		C	C						C							R	
344-U1413C-																													
2R-CC, 0-5	185.04	185.09	M	R	R						R										R				R				
3R-CC, 0-5	190.81	190.86	M	C	Freq	R		Freq			C	Freq		Freq	R						C				Freq			R	
4R-CC, 0-5	197.40	197.45	B																										
5R-CC, 0-5	211.70	211.75	M	A	Freq			Freq			A	A	C	C	Freq						C	C			A		R		
7R-CC, 0-5	236.29	236.34	G	C	C			Freq			A	C		A	R						Freq	R			R			R	
8R-CC, 0-5	246.00	246.05	P	R	R						R			R							R								
10R-CC, 0-5	264.33	264.38	M	R	C						C		Freq	C	R						C	R			R				
11R-CC, 0-5	270.76	270.81	M	C	R						A			C							C	R			R				
12R-CC, 0-5	284.99	285.04	P	R							C	R		C							C	R			R			R	



Table T3 (continued).

Core, section, interval (cm)	Depth (mbsf)		Preservation	Group abundance	Calcidiscus leptoporus	Calcispheres	Ceratolithus cristatus	Ceratolithus cristatus (rugosus)	Coccolithus pelagicus	Emiliania huxleyi	Gephyrocapsa (<4 µm)	Gephyrocapsa (>4 µm)	Gephyrocapsa caribbeanica	Gephyrocapsa oceanica	Helicosphaera carteri	Helicosphaera hyalina	Helicosphaera inversa	Helicosphaera neogranulata	Helicosphaera pavementum	Helicosphaera sellii	Helicosphaera sp.	Helicosphaera spp.	Pantosphaera discopora	Pantosphaera japonica	Pseudoemiliania lacunosa	Rhabdosphaera clavigera	Syracosphaera pulchra	Umbilicosphaera sibogae
	Top	Bottom																										
13R-CC, 0-5	291.65	291.70	M	F	R				R		C		C		R							C	R			Freq	R	
14R-CC, 0-5	299.92	299.97	M	R		R					Freq		Freq		Freq							Freq				R		
15R-CC, 0-5	309.15	309.20	M	C	R	R					C		C	C	Freq							Freq	C	R		Freq	R	
16R-CC, 0-5	323.51	323.56	M	C	Freq						C		C	C								Freq	C			R		
17R-CC, 0-5	333.38	333.43	M	C	Freq						A		C	C	C							Freq	C			R		
18R-CC, 0-5	334.22	334.27	G	A	Freq				R		C		Freq	C	C	C		Freq				Freq	A	R		R		
19R-CC, 0-3	350.74	350.77	M	R	R						C	R	Freq	C								Freq	C			Freq		
20R-CC, 0-5	357.82	357.87	M	F	Freq						C	R	Freq	C	Freq							Freq	C	Freq		R		
21R-CC, 0-5	371.26	371.31	M	F	Freq						C	R	C	C								Freq	C	R				
22R-CC, 0-5	381.86	381.91	M	F	Freq	R					C	R	C	C								Freq	C			Freq		
23R-CC, 0-5	391.67	391.72	M	F	R						C	R	Freq	Freq								C	C	R		Freq		
24R-CC, 0-5	401.42	401.47	M	C	R						Freq		Freq	Freq								C	C	Freq		Freq		
25R-CC, 0-5	409.81	409.86	M	R							Freq				R							C	C	R		R		
26R-CC, 0-5	419.14	419.19	M	R	R						Freq											Freq	Freq	R		C		
27R-CC, 0-5	429.27	429.32	M	R	R				R		Freq			Freq								Freq	Freq	R		Freq		
28R-CC, 0-5	436.98	437.03	M	R	R						C			Freq	R							R	Freq			Freq		
29R-CC, 0-5	445.90	445.95	M	F	R				R		Freq		Freq					R				Freq	Freq	R		Freq		
30R-CC, 0-5	459.41	459.46	M	R	R				R		Freq			Freq								Freq	C			R		
31R-CC, 0-5	469.17	469.22	M	R	R				R		R	Freq										C	C	R		Freq		
32R-CC, 0-5	478.72	478.77	P	R							R																	
33R-3W, 72-73	482.37	482.38		B																								
33R-CC, 0-5	488.56	488.61	M	R					R		R											R	Freq					
34R-CC, 0-5	497.26	497.31	M	R					R		R							R				R	R					
35R-CC, 0-5	504.04	504.09	M	R	R																	R						
36R-CC, 0-5	516.89	516.94	M	R					R																			
37R-CC, 0-5	526.16	526.21	M	R							R			R										R		R		
38R-CC, 0-5	533.91	533.96	M	R		R					R		R									R	R			R		
39R-CC, 0-5	546.58	546.63	P	R							R											R	R					
40R-CC, 0-5	556.37	556.42	P	R		R					Freq		R										R			R		
41R-CC, 0-5	564.60	564.65	M	R	R						Freq			R									R					
42R-CC, 0-5	573.05	573.10	P	R							R																	
43R-CC, 0-5	578.77	578.82	P	R							Freq	R														R		

Preservation: G = good, M = moderate, P = poor. Abundance: A = abundant, C = common, Freq = frequent, F = few, R = rare, B = barren.



Table T6. Uncorrected pore fluid major element concentrations, Site U1413. (Continued on next page.)

Core, section, interval (cm)	Depth (mbsf)	Volume (mL)	Salinity	pH	Alkalinity (mM)	SO <sub>4</sub> IC (mM)	SO <sub>4</sub> ICP (mM)	Cl IC (mM)	Cl titr. (mM)	Br (mM)	Na (mM)	K (mM)	Ca (mM)	Mg (mM)	NH <sub>4</sub> (mM)
344-U1413A-															
1H-2, 138–150	3.0	56	34	7.75	6.12	25.6	25.0	554	551	0.878	479	11.7	8.64	50.4	0.434
1H-4, 110–122	5.6	55	35	7.59	4.72	26.4	26.3	550	551	0.870	477	11.7	8.98	50.8	0.296
2H-2, 138–150	9.5	50	35	7.96	6.66	24.4	23.3	550	552	0.865	465	11.3	8.53	49.2	0.387
2H-5, 138–150	14.0	60	34.5	8.29	13.9	16.5	24.5	560	554	0.895	468	11.6	7.11	48.0	0.888
3H-2, 100–112	18.3	54	33	—	—	0.05	1.8	553	—	0.927	447	10.8	2.94	41.8	2.63
3H-6, 140–152	24.4	55	33	7.72	30.3	0.00	0.1	552	552	0.988	453	10.5	2.85	48.9	5.40
4H-1, 136–151	27.0	52	32.5	7.84	32.7	0.05	0.3	552	549	1.02	466	12.2	2.25	44.9	6.33
4H-4, 137–152	31.3	60	33.5	7.71	36.9	—	0.2	—	552	—	456	11.8	2.35	45.5	7.08
5H-2, 135–150	37.9	56	33	7.72	35.4	0.05	0.2	553	550	1.12	451	11.5	2.04	45.6	7.55
5H-5, 135–150	42.2	54	33	7.93	35.8	0.05	0.2	553	552	1.14	446	11.6	1.63	44.1	7.87
6H-2, 137–152	46.7	41	33	7.8	33.8	0.56	0.7	552	551	1.17	441	10.6	1.79	44.5	7.26
6H-4, 135–150	49.7	38	33	8.28	29.2	0.10	0.4	552	554	1.19	451	12.7	1.16	39.8	8.11
8H-2, 131–151	63.4	32	32.5	7.65	28.4	0.05	0.2	548	550	1.25	438	10.0	2.12	40.9	7.11
8H-5, 136–156	67.9	—	32.5	7.94	27.4	0.00	0.2	550	555	1.26	433	10.2	2.14	40.7	7.07
9H-2, 132–154	72.8	37	32.5	7.88	28.9	0.36	0.5	564	553	1.31	453	11.4	2.29	42.3	7.61
9H-5, 133–155	77.2	72	32.5	7.84	29.3	0.00	0.0	549	552	1.29	456	11.1	2.40	43.7	7.56
10H-2, 130–152	82.2	40	33	7.9	30.7	0.00	0.1	550	553	1.30	449	11.2	2.38	43.4	7.72
10H-5, 131–153	86.7	41	33	7.83	32.2	0.00	0.2	552	553	1.32	456	11.1	2.61	46.2	7.46
11H-2, 129–151	91.7	5	33	7.78	33.7	0.05	0.0	552	555	1.33	456	11.0	2.68	47.9	7.51
11H-5, 130–152	96.1	37	33	7.86	32.7	0.05	0.1	553	553	1.34	456	10.9	2.60	48.5	7.12
12H-1, 128–150	99.2	31	33	7.82	33.0	0.05	0.0	552	554	1.34	456	11.2	2.17	43.4	7.08
12H-4, 109–131	103.3	31	33	7.83	32.2	0.00	0.2	551	556	1.34	457	10.5	2.91	49.9	6.93
13H-2, 130–152	108.3	44	33	7.82	29.0	0.77	0.8	552	554	1.34	455	10.4	2.97	48.4	6.70
13H-4, 130–152	111.3	45	33	7.82	29.4	0.10	0.2	552	556	1.37	447	10.4	3.53	47.2	6.94
14H-3, 128–150	117.4	39	33	7.75	26.9	0.00	0.1	552	556	1.37	444	10.3	3.05	45.8	6.49
15H-2, 130–152	121.4	40	33	7.72	25.1	0.00	0.2	556	554	1.38	450	9.8	3.32	47.0	6.20
16H-2, 126–150	127.1	39	32.5	7.79	23.0	0.00	0.1	554	557	1.39	462	10.2	3.50	47.2	6.09
17H-2, 80–102	131.7	38	32.5	7.82	21.8	0.00	0.1	554	558	1.40	472	10.3	3.61	48.0	6.04
17H-4, 128–150	134.6	34	33	7.82	21.3	0.00	0.1	555	559	1.40	471	10.0	3.66	48.1	5.83
18H-2, 130–152	138.4	42	32.5	7.93	19.3	0.00	0.1	556	559	1.41	468	10.0	3.64	46.6	5.81
19X-4, 97–122	145.9	38	32.5	7.8	18.5	1.43	0.2	556	556	1.42	456	9.0	3.83	46.4	5.19
20X-4, 65–90	154.6	16	32	7.8	14.0	0.66	0.7	551	—	1.40	468	8.9	4.02	44.6	4.72
20X-6, 109–134	157.2	11	31.5	—	—	0.26	0.5	549	549	1.41	455	8.4	4.13	44.4	4.65
21X-3, 125–150	164.1	13	31.5	7.84	12.0	0.26	0.3	554	555	1.45	464	8.2	4.77	42.8	4.89
22X-1, 56–85	170.3	22	31.5	7.89	9.72	0.20	0.2	555	560	1.46	467	8.2	5.11	40.1	5.18
24X-1, 117–147	176.5	12	31.5	—	—	0.31	0.4	552	550	1.48	457	7.3	5.80	39.3	5.23
24X-3, 63–93	178.5	19	31	7.89	8.98	0.15	0.0	553	553	1.50	440	6.7	5.75	37.6	5.33
25X-1, 48–84	179.9	30	31	8.03	8.48	0.15	0.2	549	551	1.50	455	7.0	6.05	38.6	5.47
26X-1, 105–140	183.1	12	31.5	7.99	8.16	0.00	0.2	551	552	1.52	463	7.0	6.19	37.8	5.78
344-U1413B-															
1H-1, 140–150	1.4	—	—	7.74	5.66	24.5	26.2	554	552	0.864	482	11.6	9.15	50.7	0.347
1H-2, 140–150	2.9	42	35	7.64	5.30	24.7	26.1	556	—	0.877	482	12.0	8.94	50.5	0.341
1H-3, 140–150	4.4	41	34.5	7.61	4.63	25.2	27.3	552	551	0.856	487	11.8	9.31	51.9	0.241
1H-4, 100–110	5.5	—	—	7.66	4.41	25.0	26.9	550	—	0.857	477	11.6	9.18	51.0	0.225
1H-5, 60–70	6.2	25	35	7.9	4.65	25.0	27.5	551	555	0.853	492	12.0	9.39	52.5	0.244
2H-1, 140–150	8.0	—	—	7.8	4.86	24.5	26.5	553	552	0.865	482	11.9	9.09	51.1	0.270
2H-2, 140–150	9.5	—	—	7.92	6.33	23.0	24.9	554	—	0.865	484	11.8	8.81	51.3	0.357
2H-3, 140–150	11.0	49	34.5	7.95	8.16	21.1	23.2	551	555	0.870	484	11.7	8.47	50.8	0.440
2H-4, 140–150	12.5	52	34.5	8.15	9.81	19.7	20.6	560	—	0.887	475	11.9	7.84	49.3	0.524
2H-5, 140–150	14.0	46	33.5	7.87	12.5	16.3	17.1	552	557	0.868	471	11.6	7.17	48.3	0.673
2H-6, 110–115	15.2	—	—	8.01	19.1	9.59	8.8	553	—	0.882	471	11.8	5.83	46.7	0.913
2H-6, 130–135	15.4	—	—	7.95	22.7	5.51	5.3	552	—	0.883	482	11.9	5.41	46.8	1.04
2H-6, 140–150	15.5	38	33.5	8	24.3	2.97	3.7	556	—	0.897	474	11.6	4.99	45.4	1.03
2H-7, 10–15	15.7	—	—	7.94	26.0	0.56	1.1	553	—	0.894	476	11.8	4.60	44.8	1.12
2H-7, 30–35	15.9	—	—	7.96	26.4	0.15	0.2	553	—	0.885	468	11.4	4.36	44.8	1.16
2H-7, 50–55	16.1	—	—	8.02	25.3	0.00	0.4	551	—	0.890	470	11.6	4.25	44.9	1.20
2H-7, 65–75	16.3	41	33.5	7.95	26.9	0.00	0.2	550	—	0.881	453	11.1	4.04	43.3	1.30
3H-1, 10–15	16.2	—	—	8	24.4	0.00	0.4	555	556	0.903	464	11.7	3.66	43.7	1.82
3H-1, 30–35	16.4	—	—	7.83	23.0	0.00	7.2	553	—	0.896	471	11.5	3.55	44.3	1.93
3H-2, 144–154	18.2	—	—	7.9	24.6	0.00	—	551	—	0.912	—	—	—	—	2.56
3H-3, 142–152	19.7	—	—	7.88	26.5	0.00	0.1	550	—	0.929	461	11.2	2.31	42.8	3.47
3H-4, 138–148	21.2	—	—	7.85	27.5	0.00	0.1	550	—	0.938	455	11.2	2.07	42.3	4.00
3H-5, 140–150	22.7	—	—	7.95	26.8	0.00	0.1	546	548	0.953	452	11.5	1.90	40.8	4.63
3H-6, 140–150	24.2	—	—	7.82	28.2	0.00	0.0	546	—	0.963	472	11.9	2.10	43.8	5.02
3H-7, 140–150	25.7	—	—	7.84	29.5	0.00	0.2	547	548	0.969	466	11.9	2.09	43.6	5.50
3H-8, 80–90	26.6	—	—	7.74	30.1	0.00	0.1	545	—	0.984	451	11.1	2.08	43.0	5.60

Table T6 (continued).

Core, section, interval (cm)	Depth (mbsf)	Volume (mL)	Salinity	pH	Alkalinity (mM)	SO <sub>4</sub> IC (mM)	SO <sub>4</sub> ICP (mM)	Cl IC (mM)	Cl titr. (mM)	Br (mM)	Na (mM)	K (mM)	Ca (mM)	Mg (mM)	NH <sub>4</sub> (mM)
344-U1413C-															
2R-2, 119–149	180.5	34	31	7.92	7.86	0.00	0.0	550	550	1.51	450	6.65	6.73	37.7	5.70
2R-5, 53–83	183.9	20	31	8.01	7.72	0.00	0.1	549	551	1.53	451	6.46	6.73	37.0	5.84
3R-1, 90–122	188.6	18	31	7.87	7.93	1.17	1.3	546	—	1.46	461	6.74	7.28	37.2	5.84
5R-1, 116–146	208.3	20	31	7.94	6.75	0.77	0.6	548	547	1.56	489	7.33	8.31	34.3	7.11
6R-3, 99–129	220.7	19	30.5	7.88	6.78	0.36	0.6	546	544	1.63	452	6.92	8.16	30.3	7.07
7R-2, 77–107	228.8	15	30.5	—	—	1.12	1.2	541	540	1.60	450	6.57	8.89	31.0	6.96
7R-6, 101–131	234.5	10	30.5	7.98	6.12	0.20	0.2	545	544	1.69	460	6.57	9.38	31.1	6.94
8R-4, 87–117	241.4	21	30.5	8.05	5.85	0.51	0.5	549	549	1.71	454	6.74	9.41	29.5	7.11
10R-4, 116–150	260.7	19	30.5	—	—	0.61	0.3	544	545	1.71	451	6.78	9.68	28.0	7.35
11R-1, 114–151	266.4	19	30	7.83	6.72	0.41	0.2	543	544	1.73	463	6.74	10.4	29.5	6.77
12R-5, 80–119	280.1	22	30	—	—	0.20	0.7	541	545	1.76	446	6.81	9.80	27.8	7.15
13R-3, 93–128	288.4	13	30	—	—	0.36	0.5	536	537	1.73	462	7.00	10.1	28.5	7.20
14R-4, 16–61	299.0	15	30.5	8	5.42	0.46	0.5	542	543	1.75	445	6.76	9.61	27.5	6.88
15R-2, 77–107	306.1	23	30.5	—	—	0.71	0.9	540	542	1.72	501	7.75	10.8	30.6	6.93
16R-3, 114–150	317.8	15	30.5	—	—	0.77	0.8	542	543	1.72	460	7.17	9.87	27.1	6.93
17R-4, 92–122	328.6	17	30.5	8.07	5.35	2.14	2.1	536	538	1.64	443	6.82	9.83	27.1	6.69
19R-5, 66–96	347.9	8	30	—	—	0.66	0.7	532	534	1.68	446	7.12	9.78	24.2	6.77
20R-3, 80–110	355.8	8	30	—	—	1.07	1.3	534	535	1.66	471	7.32	10.6	25.9	—
21R-4, 123–153	368.0	7	30.5	—	—	0.92	1.0	541	543	1.69	466	7.24	10.6	24.5	6.19
22R-4, 89–119	377.4	9	30.5	—	—	0.87	0.9	536	537	1.67	452	6.72	10.8	24.7	6.51
23R-3, 122–152	385.7	6	30.5	—	—	1.07	1.1	538	539	1.65	492	7.68	12.0	25.2	6.83
24R-3, 112–142	395.3	13	30.5	—	—	1.33	1.6	535	—	1.63	498	7.34	12.2	26.9	6.22
25R-4, 122–152	406.8	11	30.5	8.22	2.58	2.04	2.1	529	530	1.57	472	7.09	12.0	24.2	6.02
26R-3, 118–148	414.5	8	30	—	—	1.17	1.0	534	535	1.59	444	6.31	11.8	22.7	6.00
27R-2, 120–150	423.1	13	30.5	—	—	1.12	1.0	542	542	1.64	458	6.59	12.3	23.6	6.17
28R-3, 88–123	433.5	11	30	—	—	0.61	0.4	—	530	—	442	6.00	12.6	23.6	5.37
29R-3, 100–135	443.5	13	30	8.17	2.69	0.77	0.9	535	533	1.60	465	6.43	12.7	24.1	5.60
30R-3, 96–131	453.1	12	30	—	—	1.68	1.7	535	533	1.55	447	6.27	12.3	23.3	5.56
31R-4, 83–118	464.3	7	30	—	—	1.07	1.3	524	523	1.52	446	5.96	12.9	23.5	5.07
32R-5, 66–101	475.1	10	30	—	—	0.87	1.0	522	522	1.59	431	5.61	12.7	22.9	4.97
33R-5, 0–30	484.4	9	30	—	—	1.12	1.1	530	533	1.56	431	5.68	12.9	22.4	5.13
34R-2, 87–122	490.8	5.5	30	—	—	0.31	0.4	532	532	1.62	454	6.11	13.4	21.5	5.06
35R-3, 94–129	502.0	10	30	8.29	—	0.77	0.8	522	525	1.52	450	5.74	14.1	22.2	4.85
36R-5, 62–97	514.1	12	30	—	—	0.36	0.5	520	527	1.21	485	6.04	15.7	24.2	4.48
37R-5, 61–96	523.6	14	30	—	—	0.46	0.7	532	527	1.34	443	5.43	14.6	21.8	4.71
38R-4, 117–152	532.9	6	30.5	—	—	0.56	0.9	543	542	1.57	448	5.39	14.6	22.1	4.56
39R-4, 116–151	542.3	17	30.5	—	—	0.61	0.7	548	545	1.61	463	5.58	15.1	22.6	4.59
40R-6, 97–132	554.6	8	30	—	—	0.51	0.5	530	534	1.55	456	5.36	14.8	22.1	4.11
41R-2, 116–151	559.0	11	30	8.45	2.66	1.12	1.0	544	541	1.56	446	5.26	15.1	23.0	—
42R-2, 56–91	568.1	12	30	—	—	1.43	1.6	543	541	1.53	448	5.23	14.8	22.3	4.28
43R-2, 73–105	577.7	7.5	30	—	—	1.33	1.4	540	539	1.52	462	5.74	14.7	20.9	4.70
Drill fluid			32	8	2.36	25.1	27.0	518	516	0.81	446	9.74	9.39	49.9	0.108

IC = ion chromatograph, ICP = inductively coupled plasma–atomic emission spectroscopy, titr. = titration, — = not measured.

Table T7. Sulfate-corrected pore fluid major element concentrations, Site U1413. (Continued on next page.)

Core, section, interval (cm)	Depth (mbsf)	Salinity	Alkalinity (mM)	Cl IC (mM)	Cl titr. (mM)	Br (mM)	Na (mM)	K (mM)	Ca (mM)	Mg (mM)	NH <sub>4</sub> (mM)
344-U1413A-											
1H-2, 138–150	3.0	34.0	6.12	554	551	0.878	479	11.7	8.64	50.4	0.434
1H-4, 110–122	5.6	35.0	4.72	550	551	0.870	477	11.7	8.98	50.8	0.296
2H-2, 138–150	9.5	35.0	6.66	550	552	0.865	465	11.3	8.53	49.2	0.387
2H-5, 138–150	14.0	34.5	13.88	560	554	0.895	468	11.6	7.11	48.0	0.888
3H-2, 100–112	18.3	33.0	—	553	—	0.927	447	10.8	2.94	41.8	2.63
3H-6, 140–152	24.4	33.0	30.27	552	552	0.988	453	10.5	2.85	48.9	5.40
4H-1, 136–151	27.0	32.5	32.71	552	549	1.02	466	12.2	2.25	44.9	6.33
4H-4, 137–152	31.3	33.5	36.92	—	552	—	456	11.8	2.35	45.5	7.08
5H-2, 135–150	37.9	33.0	35.38	553	550	1.12	451	11.5	2.04	45.6	7.55
5H-5, 135–150	42.2	33.0	35.82	553	552	1.14	446	11.6	1.63	44.1	7.87
6H-2, 137–152	46.7	33.0	34.50	552	552	1.18	441	10.6	1.62	44.4	7.43
6H-4, 135–150	49.7	33.0	29.31	553	554	1.19	451	12.7	1.13	39.8	8.14
8H-2, 131–151	63.4	32.5	28.44	548	550	1.25	438	10.0	2.10	40.9	7.13
8H-5, 136–156	67.9	32.5	27.42	550	555	1.26	433	10.2	2.14	40.7	7.07
9H-2, 132–154	72.8	32.5	29.24	565	553	1.31	453	11.4	2.19	42.2	7.72
9H-5, 133–155	77.2	32.5	29.28	549	552	1.29	456	11.1	2.40	43.7	7.56
10H-2, 130–152	82.2	33.0	30.71	550	553	1.30	449	11.2	2.38	43.4	7.72
10H-5, 131–153	86.7	33.0	32.17	552	553	1.32	456	11.1	2.61	46.2	7.46
11H-2, 129–151	91.7	33.0	33.74	552	555	1.34	456	11.0	2.66	47.9	7.52
11H-5, 130–152	96.1	33.0	32.72	553	553	1.34	456	10.9	2.59	48.5	7.13
12H-1, 128–150	99.2	33.0	33.02	552	554	1.34	456	11.2	2.16	43.3	7.09
12H-4, 109–131	103.3	33.0	32.23	551	556	1.34	457	10.5	2.91	49.9	6.93
13H-2, 130–152	108.3	33.0	29.79	553	555	1.36	456	10.4	2.77	48.4	6.91
13H-4, 130–152	111.3	33.0	29.49	552	556	1.37	447	10.4	3.50	47.2	6.97
14H-3, 128–150	117.4	33.0	26.94	552	556	1.37	444	10.3	3.05	45.8	6.49
15H-2, 130–152	121.4	33.0	25.05	556	554	1.38	450	9.76	3.32	47.0	6.20
16H-2, 126–150	127.1	32.5	23.02	554	557	1.39	462	10.2	3.50	47.2	6.09
17H-2, 80–102	131.7	32.5	21.80	554	558	1.40	472	10.3	3.61	48.0	6.04
17H-4, 128–150	134.6	33.0	21.28	555	559	1.40	471	10.0	3.66	48.1	5.83
18H-2, 130–152	138.4	32.5	19.27	556	559	1.41	468	9.96	3.64	46.6	5.81
19X-4, 97–122	145.9	32.5	19.43	558	559	1.46	457	9.00	3.50	46.2	5.50
20X-4, 65–90	154.6	32.0	14.29	552	—	1.42	469	8.84	3.88	44.4	4.85
20X-6, 109–134	157.2	31.5	—	549	550	1.41	455	8.41	4.07	44.4	4.70
21X-3, 125–150	164.1	31.5	12.09	554	555	1.45	464	8.19	4.72	42.7	4.94
22X-1, 56–85	170.3	31.5	9.78	555	561	1.47	467	8.15	5.08	40.0	5.22
24X-1, 117–147	176.5	31.5	—	552	551	1.49	458	7.22	5.75	39.2	5.29
24X-3, 63–93	178.5	31.0	9.02	554	553	1.50	440	6.69	5.73	37.5	5.36
25X-1, 48–84	179.9	31.0	8.52	550	552	1.50	455	6.96	6.03	38.5	5.51
26X-1, 105–140	183.1	31.5	8.16	551	552	1.52	463	7.00	6.19	37.8	5.78
344-U1413B-											
1H-1, 140–150	1.4	—	5.66	554	552	0.864	482	11.6	9.15	50.7	0.347
1H-2, 140–150	2.9	35.0	5.30	556	—	0.877	482	12.0	8.94	50.5	0.341
1H-3, 140–150	4.4	34.5	4.63	552	551	0.856	487	11.8	9.31	51.9	0.241
1H-4, 100–110	5.5	—	4.41	550	—	0.857	477	11.6	9.18	51.0	0.225
1H-5, 60–70	6.2	35.0	4.65	551	555	0.853	492	12.0	9.39	52.5	0.244
2H-1, 140–150	8.0	—	4.86	553	552	0.865	482	11.9	9.09	51.1	0.270
2H-2, 140–150	9.5	—	6.33	554	—	0.865	484	11.8	8.81	51.3	0.357
2H-3, 140–150	11.0	34.50	8.16	551	555	0.870	484	11.7	8.47	50.8	0.440
2H-4, 140–150	12.5	34.50	9.81	560	—	0.887	475	11.9	7.84	49.3	0.524
2H-5, 140–150	14.0	33.50	12.47	552	557	0.868	471	11.6	7.17	48.3	0.673
2H-6, 110–115	15.2	—	19.06	553	—	0.882	471	11.8	5.83	46.7	0.913
2H-6, 130–135	15.4	—	22.67	552	—	0.883	482	11.9	5.41	46.8	1.04
2H-6, 140–150	15.5	33.50	24.27	556	—	0.897	474	11.6	4.99	45.4	1.03
2H-7, 10–15	15.7	—	26.02	553	—	0.894	476	11.8	4.60	44.8	1.12
2H-7, 30–35	15.9	—	26.37	553	—	0.885	468	11.4	4.36	44.8	1.16
2H-7, 50–55	16.1	—	25.30	551	—	0.890	470	11.6	4.25	44.9	1.20
2H-7, 65–75	16.3	33.50	26.94	550	—	0.881	453	11.1	4.04	43.3	1.30
3H-1, 10–15	16.2	—	24.35	555	556	0.903	464	11.7	3.66	43.7	1.82
3H-1, 30–35	16.4	—	23.02	553	—	0.896	471	11.5	3.55	44.3	1.93
3H-2, 144–154	18.2	—	24.61	551	—	0.912	—	—	—	—	2.56
3H-3, 142–152	19.7	—	26.48	550	—	0.929	461	11.2	2.31	42.8	3.47
3H-4, 138–148	21.2	—	27.46	550	—	0.938	455	11.2	2.07	42.3	4.00
3H-5, 140–150	22.7	—	26.82	546	548	0.953	452	11.5	1.90	40.8	4.63
3H-6, 140–150	24.2	—	28.20	546	—	0.963	472	11.9	2.10	43.8	5.02
3H-7, 140–150	25.7	—	29.51	547	548	0.969	466	11.9	2.09	43.6	5.50
3H-8, 80–90	26.6	—	30.05	545	—	0.984	451	11.1	2.08	43.0	5.60

Table T7 (continued).

Core, section, interval (cm)	Depth (mbsf)	Salinity	Alkalinity (mM)	Cl IC (mM)	Cl titr. (mM)	Br (mM)	Na (mM)	K (mM)	Ca (mM)	Mg (mM)	NH <sub>4</sub> (mM)
344-U1413C-											
2R-2, 119-149	180.5	31.0	7.86	550	550	1.51	450	6.65	6.73	37.7	5.70
2R-5, 53-83	183.9	31.0	7.72	549	551	1.53	451	6.46	6.73	37.0	5.84
3R-1, 90-122	188.6	31.0	8.20	547	—	1.49	462	6.59	7.18	36.5	6.13
5R-1, 116-146	208.3	31.0	6.89	549	548	1.59	491	7.26	8.28	33.8	7.33
6R-3, 99-129	220.7	30.5	6.84	547	545	1.64	452	6.88	8.15	30.0	7.17
7R-2, 77-107	228.8	30.4	—	542	541	1.64	450	6.42	8.87	30.1	7.29
7R-6, 101-131	234.5	30.5	6.15	545	544	1.69	460	6.54	9.38	30.9	6.99
8R-4, 87-117	241.4	30.5	5.92	550	549	1.73	455	6.68	9.41	29.1	7.26
10R-4, 116-150	260.7	30.5	—	545	546	1.74	451	6.70	9.69	27.4	7.53
11R-1, 114-151	266.4	30.0	6.79	543	545	1.75	463	6.69	10.4	29.1	6.88
12R-5, 80-119	280.1	30.0	—	542	546	1.76	446	6.79	9.80	27.6	7.21
13R-3, 93-128	288.4	30.0	—	536	537	1.74	462	6.96	10.1	28.2	7.30
14R-4, 16-61	299.0	30.5	5.48	543	544	1.77	445	6.70	9.62	27.1	7.01
15R-2, 103-135	306.1	30.5	—	541	543	1.74	502	7.70	10.8	30.1	7.13
16R-3, 114-150	317.8	30.5	—	543	543	1.75	461	7.09	9.88	26.4	7.14
17R-4, 92-122	328.6	30.4	5.63	537	540	1.71	443	6.54	9.87	25.0	7.31
19R-5, 66-96	347.9	29.9	—	532	534	1.71	446	7.05	9.79	23.5	6.95
20R-3, 80-110	355.8	29.9	—	535	535	1.70	472	7.22	10.7	24.8	—
21R-4, 123-153	368.0	30.4	—	542	544	1.73	467	7.14	10.7	23.6	6.42
22R-4, 89-119	377.4	30.4	—	536	538	1.70	452	6.61	10.9	23.8	6.74
23R-3, 122-152	385.7	30.4	—	539	540	1.68	495	7.59	12.1	24.1	7.14
24R-3, 112-142	395.3	30.4	—	536	—	1.67	501	7.21	12.4	25.6	6.57
25R-4, 122-152	406.8	30.4	2.59	530	531	1.63	474	6.86	12.2	21.9	6.55
26R-3, 118-148	414.5	29.9	—	534	536	1.63	444	6.14	11.9	21.4	6.29
27R-2, 120-150	423.1	30.4	—	543	543	1.67	459	6.44	12.5	22.3	6.46
28R-3, 88-123	433.5	30.0	—	—	530	—	442	5.91	12.7	23.0	5.51
29R-3, 100-135	443.5	29.9	2.70	535	533	1.63	465	6.33	12.8	23.3	5.77
30R-3, 96-131	453.1	29.9	—	536	535	1.61	447	6.02	12.5	21.4	5.95
31R-4, 83-118	464.3	29.9	—	524	523	1.55	446	5.80	13.0	22.3	5.30
32R-5, 66-101	475.1	29.9	—	522	522	1.61	431	5.46	12.8	22.0	5.14
33R-5, 0-30	484.4	29.9	—	531	533	1.59	431	5.49	13.0	21.1	5.37
34R-2, 87-122	490.8	30.0	—	532	532	1.63	454	6.06	13.4	21.2	5.12
35R-3, 94-129	502.0	29.9	—	522	526	1.54	450	5.61	14.2	21.3	5.00
36R-5, 62-97	514.1	30.0	—	520	527	1.22	485	5.98	15.8	23.9	4.55
37R-5, 61-96	523.6	30.0	—	532	527	1.35	443	5.35	14.7	21.3	4.79
38R-4, 117-152	532.9	30.5	—	544	542	1.59	448	5.29	14.7	21.5	4.66
39R-4, 116-151	542.3	30.5	—	549	546	1.63	464	5.48	15.2	21.9	4.70
40R-6, 97-132	554.6	30.0	—	530	534	1.57	457	5.27	14.9	21.5	4.19
41R-2, 116-151	559.0	29.9	2.68	545	542	1.60	446	5.05	15.4	21.7	—
42R-2, 56-91	568.1	29.9	—	545	543	1.58	448	4.96	15.1	20.7	4.54
43R-2, 73-105	577.7	29.9	—	542	540	1.56	463	5.52	15.0	19.2	4.96

IC = ion chromatograph, titr. = titration, — = not measured.

Table T8. Uncorrected pore fluid minor element concentrations, Site U1413. (Continued on next page.)

Core, section, interval (cm)	Depth (mbsf)	B ( $\mu\text{M}$ )	Li ( $\mu\text{M}$ )	Sr ( $\mu\text{M}$ )	Ba ( $\mu\text{M}$ )	Mn ( $\mu\text{M}$ )	Si ( $\mu\text{M}$ )
344-U1413A-							
1H-2, 138–150	3.0	535	19.9	91.7	1.0	1.5	397
1H-4, 110–122	5.6	531	30.9	88.0	2.2	ND	307
2H-2, 138–150	9.5	497	28.7	85.6	1.9	0.3	453
2H-5, 138–150	14.0	512	23.1	83.2	0.8	ND	550
3H-2, 100–112	18.3	504	10.1	61.0	3.0	0.3	458
3H-6, 140–152	24.4	452	12.1	50.5	1.6	1.2	354
4H-1, 136–151	27.0	474	12.2	51.0	2.1	0.7	352
4H-4, 137–152	31.3	484	18.3	48.5	1.5	0.8	441
5H-2, 135–150	37.9	484	21.5	49.6	3.3	1.9	593
5H-5, 135–150	42.2	426	23.4	49.5	2.1	1.2	417
6H-2, 137–152	46.7	510	22.5	52.3	0.9	1.0	448
6H-4, 135–150	49.7	332	15.7	37.6	3.9	ND	171
8H-2, 131–151	63.4	425	16.6	47.7	0.6	0.5	457
8H-5, 136–156	67.9	373	20.7	46.0	1.4	ND	393
9H-2, 132–154	72.8	381	24.4	49.6	0.5	0.7	415
9H-5, 133–155	77.2	369	21.8	44.6	0.5	0.3	375
10H-2, 130–152	82.2	375	17.7	45.5	0.5	0.6	438
10H-5, 131–153	86.7	387	19.0	43.6	0.4	0.4	423
11H-2, 129–151	91.7	428	21.8	40.8	0.3	0.8	321
11H-5, 130–152	96.1	362	22.0	38.6	1.0	0.9	333
12H-1, 128–150	99.2	406	19.7	44.3	0.8	1.6	371
12H-4, 109–131	103.3	391	18.5	42.2	0.4	1.5	336
13H-2, 130–152	108.3	353	15.2	42.8	0.0	1.0	348
13H-4, 130–152	111.3	359	16.5	41.3	0.4	0.9	349
14H-3, 128–150	117.4	373	18.6	44.0	1.3	0.5	296
15H-2, 130–152	121.4	351	21.1	48.0	0.4	1.0	347
16H-2, 126–150	127.1	346	21.5	48.5	0.8	1.5	334
17H-2, 80–102	131.7	379	17.0	50.9	0.3	0.6	302
17H-4, 128–150	134.6	392	23.2	51.9	1.4	1.1	319
18H-2, 130–152	138.4	336	19.9	52.0	0.5	0.1	243
19X-4, 97–122	145.9	368	24.6	55.3	0.4	1.9	358
20X-4, 65–90	154.6	277	29.0	53.9	2.7	1.1	298
20X-6, 109–134	157.2	296	29.0	53.5	3.0	0.7	332
21X-3, 125–150	164.1	241	37.2	49.3	4.0	1.5	286
22X-1, 56–85	170.3	192	37.5	51.0	3.2	2.1	230
24X-1, 117–147	176.5	166	37.3	47.9	2.8	1.3	180
24X-3, 63–93	178.5	182	37.7	48.4	2.7	1.5	204
25X-1, 48–84	179.9	153	35.2	48.9	4.8	1.1	189
26X-1, 105–140	183.1	141	44.9	44.4	2.5	0.7	158
344-U1413B-							
1H-1, 140–150	1.4	542	26.7	89.6	0.3	1.2	333
1H-2, 140–150	2.9	495	18.8	86.3	0.3	1.1	336
1H-3, 140–150	4.4	504	25.5	87.9	0.2	0.3	345
1H-4, 100–110	5.5	504	27.3	89.7	0.2	0.2	321
1H-5, 60–70	6.2	489	28.5	87.3	0.4	0.1	291
2H-1, 140–150	8.0	494	29.3	87.3	0.7	0.5	346
2H-2, 140–150	9.5	501	27.8	88.0	0.5	0.2	404
2H-3, 140–150	11.0	483	25.9	83.3	0.7	2.0	461
2H-4, 140–150	12.5	486	20.2	81.2	0.5	ND	514
2H-5, 140–150	14.0	502	21.4	83.6	0.6	1.7	511
2H-6, 110–115	15.2	528	23.5	79.3	0.5	0.1	535
2H-6, 130–135	15.4	512	21.8	73.3	0.5	0.2	501
2H-6, 140–150	15.5	471	20.7	71.7	0.5	0.0	457
2H-7, 10–15	15.7	517	15.9	72.8	0.4	ND	484
2H-7, 30–35	15.9	492	14.8	70.2	0.6	ND	511
2H-7, 50–55	16.1	500	20.8	67.0	1.1	ND	497
2H-7, 65–75	16.3	523	23.1	68.1	1.0	ND	529
3H-1, 10–15	16.2	496	14.7	64.8	0.9	0.7	505
3H-1, 30–35	16.4	480	14.8	66.5	0.9	0.4	508
3H-2, 144–154	18.2						
3H-3, 142–152	19.7	451	11.1	56.2	0.5	0.5	368
3H-4, 138–148	21.2	457	5.8	54.1	0.6	0.5	321
3H-5, 140–150	22.7	390	10.0	49.2	0.7	0.7	276
3H-6, 140–150	24.2	409	14.4	50.4	0.6	1.3	289
3H-7, 140–150	25.7	448	12.9	48.2	0.5	0.7	343
3H-8, 80–90	26.6	459	17.7	47.1	0.7	0.7	360

Table T8 (continued).

Core, section, interval (cm)	Depth (mbsf)	B ( $\mu\text{M}$ )	Li ( $\mu\text{M}$ )	Sr ( $\mu\text{M}$ )	Ba ( $\mu\text{M}$ )	Mn ( $\mu\text{M}$ )	Si ( $\mu\text{M}$ )
344-U1413C-							
2R-2, 119–149	180.5	229	43.2	48.7	2.2	0.7	196
2R-5, 53–83	183.9	196	43.3	48.9	1.6	1.2	171
3R-1, 90–122	188.6	225	44.2	51.3	1.5	1.4	207
5R-1, 116–146	208.3	182	44.0	58.2	1.8	0.7	167
6R-3, 99–129	220.7	177	37.6	62.8	3.0	0.7	152
7R-2, 77–107	228.8	175	38.1	64.8	3.0	1.4	167
7R-6, 101–131	234.5	161	38.6	65.8	3.0	1.4	172
8R-4, 87–117	241.4	131	37.8	66.2	3.7	0.6	132
10R-4, 116–150	260.7	119	43.1	69.3	4.4	0.7	148
11R-1, 114–151	266.4	133	42.6	67.6	4.4	0.7	165
12R-5, 80–119	280.1	132	46.8	69.1	4.5	0.4	143
13R-3, 93–128	288.4	136	54.1	69.4	4.5	1.9	152
14R-4, 16–61	299.0	137	55.0	68.2	4.3	1.1	135
15R-2, 103–135	306.1	154	54.4	69.3	5.1	1.4	195
16R-3, 114–150	317.8	139	56.3	67.1	3.9	0.4	145
17R-4, 92–122	328.6	148	60.0	67.7	3.2	0.8	150
19R-5, 66–96	347.9	114	57.3	66.1	2.6	0.2	99
20R-3, 80–110	355.8	134	57.7	67.4	2.4	0.0	108
21R-4, 123–153	368.0	150	58.1	68.4	2.6	0.4	126
22R-4, 89–119	377.4	170	65.5	71.4	3.1	0.7	137
23R-3, 122–152	385.7	100	67.6	73.2	3.1	0.3	98
24R-3, 112–142	395.3	158	76.3	72.4	3.0	0.7	130
25R-4, 122–152	406.8	114	75.9	73.9	3.6	0.2	99
26R-3, 118–148	414.5	132	78.2	74.1	3.8	0.7	113
27R-2, 120–150	423.1	145	78.2	72.8	3.9	0.8	117
28R-3, 88–123	433.5	142	75.9	73.1	4.4	0.9	131
29R-3, 100–135	443.5	122	73.7	72.0	3.7	0.3	108
30R-3, 96–131	453.1	126	75.4	75.2	4.3	0.3	103
31R-4, 83–118	464.3	121	77.8	75.1	3.5	0.6	111
32R-5, 66–101	475.1	117	74.9	74.1	2.3	0.2	98
33R-5, 0–30	484.4	113	73.0	73.1	2.1	0.2	91
34R-2, 87–122	490.8	105	69.9	73.6	2.4	0.1	88
35R-3, 94–129	502.0	104	69.9	76.6	1.7	0.1	93
36R-5, 62–97	514.1	104	64.8	73.4	1.3	0.2	109
37R-5, 61–96	523.6	109	65.7	73.9	1.3	0.4	94
38R-4, 117–152	532.9	119	65.2	75.1	1.0	0.7	99
39R-4, 116–151	542.3	114	61.9	72.6	0.9	0.6	87
40R-6, 97–132	554.6	102	57.1	69.6	0.8	0.6	82
41R-2, 116–151	559.0	107	59.4	70.2	1.0	1.0	93
42R-2, 56–91	568.1	108	59.7	70.8	0.9	1.1	90
43R-2, 73–105	577.7	89	52.1	68.1	1.1	1.0	61
Drill fluid		362	23.0	83.0	0.0	0.0	4

ND = not detected.

**Table T9.** Pore fluid minor element concentrations corrected for drill fluid contamination, Site U1413. (Continued on next page.)

Core, section, interval (cm)	Depth (mbsf)	B ( $\mu\text{M}$ )	Li ( $\mu\text{M}$ )	Sr ( $\mu\text{M}$ )	Ba ( $\mu\text{M}$ )	Mn ( $\mu\text{M}$ )	Si ( $\mu\text{M}$ )
344-U1413A-							
1H-2, 138–150	3.0	535	19.9	91.7	1.0	1.5	397
1H-4, 110–122	5.6	531	30.9	88.0	2.2	ND	307
2H-2, 138–150	9.5	497	28.7	85.6	1.9	0.3	453
2H-5, 138–150	14.0	512	23.1	83.2	0.8	ND	550
3H-2, 100–112	18.3	504	10.1	61.0	3.0	0.3	458
3H-6, 140–152	24.4	452	12.1	50.5	1.6	1.2	354
4H-1, 136–151	27.0	474	12.2	51.0	2.1	0.7	352
4H-4, 137–152	31.3	484	18.3	48.5	1.5	0.8	441
5H-2, 135–150	37.9	484	21.5	49.6	3.3	1.9	593
5H-5, 135–150	42.2	426	23.4	49.5	2.1	1.2	417
6H-2, 137–152	46.7	514	22.5	51.6	1.0	1.0	458
6H-4, 135–150	49.7	332	15.7	37.4	3.9	ND	172
8H-2, 131–151	63.4	425	16.5	47.7	0.6	0.5	458
8H-5, 136–156	67.9	373	20.7	46.0	1.4	ND	393
9H-2, 132–154	72.8	381	24.4	49.1	0.5	0.7	421
9H-5, 133–155	77.2	369	21.8	44.6	0.5	0.3	375
10H-2, 130–152	82.2	375	17.7	45.5	0.5	0.6	438
10H-5, 131–153	86.7	387	19.0	43.6	0.4	0.4	423
11H-2, 129–151	91.7	428	21.8	40.7	0.4	0.8	322
11H-5, 130–152	96.1	362	22.0	38.5	1.0	0.9	334
12H-1, 128–150	99.2	406	19.7	44.3	0.8	1.6	372
12H-4, 109–131	103.3	391	18.5	42.2	0.4	1.5	336
13H-2, 130–152	108.3	353	14.9	41.5	0.0	1.0	359
13H-4, 130–152	111.3	359	16.5	41.2	0.4	0.9	350
14H-3, 128–150	117.4	373	18.6	44.0	1.3	0.5	296
15H-2, 130–152	121.4	351	21.1	48.0	0.4	1.0	347
16H-2, 126–150	127.1	346	21.5	48.5	0.8	1.5	334
17H-2, 80–102	131.7	379	17.0	50.9	0.3	0.6	302
17H-4, 128–150	134.6	392	23.2	51.9	1.4	1.1	319
18H-2, 130–152	138.4	336	19.9	52.0	0.5	0.1	243
19X-4, 97–122	145.9	368	24.7	53.7	0.5	2.0	379
20X-4, 65–90	154.6	275	29.2	53.1	2.8	1.1	306
20X-6, 109–134	157.2	295	29.0	53.2	3.0	0.7	335
21X-3, 125–150	164.1	239	37.3	48.9	4.1	1.5	289
22X-1, 56–85	170.3	191	37.6	50.7	3.3	2.1	232
24X-1, 117–147	176.5	164	37.5	47.5	2.9	1.3	182
24X-3, 63–93	178.5	181	37.8	48.2	2.7	1.5	206
25X-1, 48–84	179.9	152	35.3	48.7	4.9	1.1	190
26X-1, 105–140	183.1	141	44.9	44.4	2.5	0.7	158
344-U1413B-							
1H-1, 140–150	1.4	542	26.7	89.6	0.3	1.2	333
1H-2, 140–150	2.9	495	18.8	86.3	0.3	1.1	336
1H-3, 140–150	4.4	504	25.5	87.9	0.2	0.3	345
1H-4, 100–110	5.5	504	27.3	89.7	0.2	0.2	321
1H-5, 60–70	6.2	489	28.5	87.3	0.4	0.1	291
2H-1, 140–150	8.0	494	29.3	87.3	0.7	0.5	346
2H-2, 140–150	9.5	501	27.8	88.0	0.5	0.2	404
2H-3, 140–150	11.0	483	25.9	83.3	0.7	2.0	461
2H-4, 140–150	12.5	486	20.2	81.2	0.5	ND	514
2H-5, 140–150	14.0	502	21.4	83.6	0.6	1.7	511
2H-6, 110–115	15.2	528	23.5	79.3	0.5	0.1	535
2H-6, 130–135	15.4	512	21.8	73.3	0.5	0.2	501
2H-6, 140–150	15.5	471	20.7	71.7	0.5	0.0	457
2H-7, 10–15	15.7	517	15.9	72.8	0.4	ND	484
2H-7, 30–35	15.9	492	14.8	70.2	0.6	ND	511
2H-7, 50–55	16.1	500	20.8	67.0	1.1	ND	497
2H-7, 65–75	16.3	523	23.1	68.1	1.0	ND	529
3H-1, 10–15	16.2	496	14.7	64.8	0.9	0.7	505
3H-1, 30–35	16.4	480	14.8	66.5	0.9	0.4	508
3H-2, 144–154	18.2						
3H-3, 142–152	19.7	451	11.1	56.2	0.5	0.5	368
3H-4, 138–148	21.2	457	5.8	54.1	0.6	0.5	321
3H-5, 140–150	22.7	390	10.0	49.2	0.7	0.7	276
3H-6, 140–150	24.2	409	14.4	50.4	0.6	1.3	289
3H-7, 140–150	25.7	448	12.9	48.2	0.5	0.7	343
3H-8, 80–90	26.6	459	17.7	47.1	0.7	0.7	360

Table T9 (continued).

Core, section, interval (cm)	Depth (mbsf)	B ( $\mu\text{M}$ )	Li ( $\mu\text{M}$ )	Sr ( $\mu\text{M}$ )	Ba ( $\mu\text{M}$ )	Mn ( $\mu\text{M}$ )	Si ( $\mu\text{M}$ )
344-U1413C-							
2R-2, 119–149	180.5	229	43.2	48.7	2.2	0.7	196
2R-5, 53–83	183.9	196	43.3	48.9	1.6	1.2	171
3R-1, 90–122	188.6	218	45.2	49.8	1.6	1.5	217
5R-1, 116–146	208.3	176	44.7	57.4	1.8	0.7	172
6R-3, 99–129	220.7	174	37.8	62.5	3.0	0.7	155
7R-2, 77–107	228.8	166	38.8	64.0	3.1	1.5	175
7R-6, 101–131	234.5	159	38.7	65.6	3.0	1.4	173
8R-4, 87–117	241.4	126	38.1	65.8	3.8	0.6	135
10R-4, 116–150	260.7	113	43.6	69.0	4.5	0.7	152
11R-1, 114–151	266.4	129	42.9	67.3	4.5	0.7	167
12R-5, 80–119	280.1	130	47.0	69.0	4.5	0.4	144
13R-3, 93–128	288.4	133	54.5	69.2	4.5	2.0	154
14R-4, 16–61	299.0	133	55.6	67.9	4.4	1.2	138
15R-2, 103–135	306.1	147	55.3	68.9	5.3	1.4	201
16R-3, 114–150	317.8	132	57.3	66.6	4.0	0.4	150
17R-4, 92–122	328.6	129	63.4	66.3	3.5	0.8	164
19R-5, 66–96	347.9	107	58.2	65.7	2.6	0.2	101
20R-3, 80–110	355.8	123	59.3	66.7	2.5	0.0	—
21R-4, 123–153	368.0	142	59.4	67.8	2.7	0.4	131
22R-4, 89–119	377.4	163	67.0	70.9	3.2	0.7	142
23R-3, 122–152	385.7	88	69.5	72.7	3.2	0.3	102
24R-3, 112–142	395.3	146	79.3	71.8	3.2	0.7	137
25R-4, 122–152	406.8	92	80.6	73.1	4.0	0.2	108
26R-3, 118–148	414.5	121	80.9	73.7	4.0	0.7	119
27R-2, 120–150	423.1	135	80.8	72.3	4.1	0.8	122
28R-3, 88–123	433.5	136	77.2	72.9	4.5	0.9	134
29R-3, 100–135	443.5	115	75.3	71.7	3.9	0.3	112
30R-3, 96–131	453.1	109	79.1	74.6	4.6	0.4	110
31R-4, 83–118	464.3	110	80.3	74.8	3.7	0.6	115
32R-5, 66–101	475.1	108	76.8	73.8	2.4	0.2	102
33R-5, 0–30	484.4	101	75.4	72.6	2.2	0.2	95
34R-2, 87–122	490.8	101	70.5	73.5	2.4	0.1	89
35R-3, 94–129	502.0	96	71.4	76.4	1.8	0.1	96
36R-5, 62–97	514.1	100	65.4	73.3	1.3	0.2	111
37R-5, 61–96	523.6	104	66.5	73.7	1.3	0.4	96
38R-4, 117–152	532.9	114	66.2	74.9	1.1	0.7	101
39R-4, 116–151	542.3	108	62.8	72.4	0.9	0.6	89
40R-6, 97–132	554.6	97	57.8	69.3	0.8	0.6	84
41R-2, 116–151	559.0	96	61.1	69.6	1.1	1.0	—
42R-2, 56–91	568.1	92	61.9	70.1	1.0	1.2	95
43R-2, 73–105	577.7	74	53.7	67.3	1.1	1.0	65

ND = not detected, — = not measured.

Table T10. Concentrations of hydrocarbon gases in headspace gas samples, Site U1413. (Continued on next page.)

Core, section, interval (cm)	Depth (mbsf)	Methane (ppmv)	Ethane (ppmv)	Propane (ppmv)	<i>n</i> -Butane (ppmv)	<i>iso</i> -Pentane (ppmv)	C <sub>1</sub> /C <sub>2+</sub>
344-U1413A-							
1H-3, 0-5	3.00	6.95	ND	ND	ND	ND	—
1H-5, 0-5	5.72	5.94	ND	ND	ND	ND	—
2H-3, 0-5	9.60	14.8	ND	ND	ND	ND	—
2H-6, 0-5	14.10	73.5	ND	ND	ND	ND	—
3H-3, 0-5	18.44	11,100	0.518	ND	ND	ND	10,200
3H-7, 0-5	24.53	18,100	0.840	ND	ND	ND	21,600
4H-2, 0-5	27.03	10,800	ND	ND	ND	ND	17,000
4H-5, 0-5	31.43	10,100	ND	ND	ND	ND	17,500
4H-7, 0-5	32.90	4,060	ND	ND	ND	ND	10,000
5H-3, 0-5	38.01	9,240	ND	ND	ND	ND	—
5H-6, 0-5	42.33	11,400	ND	ND	ND	ND	17,800
6H-3, 0-5	46.86	15,500	ND	ND	ND	ND	24,300
6H-5, 0-5	49.82	11,500	ND	2.22	ND	ND	1,040
7H-2, 0-5	53.41	33,900	ND	ND	ND	ND	74,600
8H-3, 0-5	63.61	7,090	ND	ND	ND	ND	—
9H-3, 0-5	73.02	13,300	ND	ND	ND	ND	—
9H-6, 0-5	77.43	8,030	ND	ND	ND	ND	—
10H-3, 0-5	82.43	14,000	ND	ND	ND	ND	—
10H-6, 0-5	86.92	12,100	ND	ND	ND	ND	—
11H-3, 0-5	91.93	8,520	ND	0.875	ND	ND	9,730
11H-6, 0-5	96.30	17,600	ND	ND	ND	ND	—
12H-2, 0-5	99.40	5,290	ND	ND	ND	ND	—
12H-5, 0-5	103.50	6,980	ND	ND	ND	ND	—
13H-3, 0-5	108.53	13,600	0.480	ND	ND	ND	28,300
13H-5, 0-5	111.47	10,900	ND	ND	ND	ND	—
14H-4, 0-5	117.57	12,400	ND	ND	ND	ND	—
15H-3, 0-5	121.63	7,700	ND	ND	ND	ND	—
16H-3, 0-5	127.31	7,890	ND	ND	ND	ND	—
17H-3, 0-5	131.93	9,300	ND	ND	ND	ND	—
17H-5, 0-5	134.85	6,740	ND	ND	ND	ND	—
18H-3, 0-5	138.64	9,700	0.518	ND	ND	ND	18,700
19X-5, 0-5	146.19	8,530	0.961	ND	ND	ND	8,880
20X-5, 0-5	154.80	1,860	ND	ND	ND	ND	—
20X-7, 0-5	157.47	3,480	0.597	ND	ND	ND	5,830
21X-4, 0-5	164.32	2,700	0.611	ND	ND	ND	4,410
22X-2, 0-5	170.55	5,120	0.926	ND	ND	ND	5,530
23X-1, 0-5	174.30	15,400	1.889	ND	ND	ND	8,180
24X-2, 0-5	176.77	2,770	0.772	ND	ND	ND	3,590
24X-4, 0-5	178.77	1,580	0.433	ND	ND	ND	3,650
25X-2, 0-5	180.24	14,000	2.370	ND	ND	ND	5,910
26X-2, 0-5	183.40	2,330	0.713	ND	ND	ND	3,270
344-U1413B-							
1H-2, 0-5	1.50	2.90	ND	ND	ND	ND	—
1H-3, 0-5	3.00	3.31	ND	ND	ND	ND	—
1H-4, 0-5	4.50	3.73	ND	ND	ND	ND	—
1H-5, 0-5	5.60	10.6	ND	ND	ND	ND	—
2H-2, 0-5	8.10	9.95	ND	ND	ND	ND	—
2H-3, 0-5	9.60	13.7	ND	ND	ND	ND	—
2H-4, 0-5	11.10	30.8	ND	ND	ND	ND	—
2H-5, 0-5	12.60	38.8	ND	ND	ND	ND	—
2H-6, 0-5	14.10	119	ND	ND	ND	ND	—
2H-7, 0-5	15.60	364	ND	ND	ND	ND	—
3H-2, 0-5	16.74	13,100	0.588	ND	ND	ND	22,300
3H-3, 0-5	18.28	15,200	ND	ND	ND	ND	30,300
3H-4, 0-5	19.80	16,200	ND	ND	ND	ND	—
3H-5, 0-5	21.28	8,790	ND	ND	ND	ND	—
3H-6, 0-5	22.78	12,500	0.834	ND	ND	ND	7,880
3H-7, 0-5	24.28	42,600	0.748	ND	ND	ND	30,800
3H-8, 0-5	25.78	17,200	0.588	ND	ND	ND	14,200
344-U1413C-							
2R-3, 0-5	180.83	11,100	2.14	ND	ND	ND	3,920
2R-6, 0-5	184.18	3,570	4.34	4.31	ND	ND	—
3R-2, 0-5	188.92	2,550	0.957	ND	ND	ND	—
5R-2, 0-5	208.56	3,280	1.97	ND	ND	ND	—
6R-4, 0-5	220.97	4,040	2.39	ND	ND	ND	1,760
7R-3, 0-5	229.07	5,080	3.33	ND	ND	ND	1,470

Table T10 (continued).

Core, section, interval (cm)	Depth (mbsf)	Methane (ppmv)	Ethane (ppmv)	Propane (ppmv)	<i>n</i> -Butane (ppmv)	<i>iso</i> -Pentane (ppmv)	C <sub>1</sub> /C <sub>2+</sub>
7R-7, 0-5	234.78	3,340	2.54	ND	ND	ND	1,130
8R-5, 0-5	241.69	3,990	2.95	ND	ND	ND	1,420
10R-5, 0-5	261.06	10,700	7.02	ND	ND	ND	1,310
11R-2, 0-5	266.81	5,200	3.95	ND	ND	ND	940
12R-6, 0-5	280.49	15,800	11.3	ND	ND	ND	1,030
13R-4, 0-5	288.75	13,200	10.5	ND	ND	0.768	945
14R-4, 11-16	298.90	2,100	3.23	ND	ND	ND	638
15R-2, 0-5	305.05	13,900	11.1	ND	ND	ND	1,110
16R-4, 0-5	318.16	9,760	13.1	ND	ND	1.59	555
17R-5, 0-5	328.91	23,700	26.6	ND	ND	3.67	559
18R-1, 0-5	333.20	13,300	16.6	ND	ND	ND	684
19R-5, 65-66	347.86	10,400	19.1	4.89	0.889	5.20	234
20R-4, 0-5	356.07	8,450	21.0	7.28	1.05	4.40	172
21R-5, 0-5	368.30	3,390	10.4	ND	1.39	8.43	114
22R-5, 0-5	377.69	6,290	20.4	10.5	1.34	7.54	110
23R-4, 0-5	386.04	6,800	15.6	6.38	0.835	4.25	175
24R-4, 0-5	395.60	5,500	20.1	11.3	1.22	5.02	102
25R-5, 0-5	407.12	3,020	11.6	ND	1.09	4.49	101
26R-4, 0-5	414.81	5,710	22.3	11.7	1.44	6.33	94.0
27R-3, 0-5	423.43	14,700	41.9	16.8	1.31	5.25	165
28R-4, 0-5	433.86	31,500	75.5	24.2	1.05	4.14	221
29R-4, 0-5	443.82	13,900	39.3	11.0	0.667	2.83	187
30R-4, 0-5	453.49	7,990	21.3	7.14	ND	1.22	196
31R-5, 0-5	464.61	3,690	19.1	5.92	0.640	2.46	101
32R-6, 0-5	475.44	2,160	15.8	ND	ND	1.64	70.5
33R-6, 0-5	484.73	2,800	27.8	3.45	ND	2.40	58.0
34R-3, 0-5	491.11	1,920	21.0	4.18	0.691	2.96	53.8
35R-4, 0-5	502.34	2,180	31.5	2.41	ND	1.25	46.3
36R-6, 0-5	514.43	4,100	74.2	8.19	0.891	3.53	42.2
37R-6, 0-5	523.92	1,570	27.9	ND	ND	1.05	40.7
38R-5, 0-5	533.25	4,900	75.5	9.34	ND	1.69	51.2
39R-5, 0-5	542.64	1,740	35.5	ND	ND	1.76	36.8
40R-7, 0-5	554.94	4,390	104	14.2	0.759	2.28	32.4
41R-3, 0-5	559.31	3,860	82.8	11.0	0.831	2.32	36.2
42R-3, 0-5	568.41	3,660	106	17.7	1.06	2.62	25.3
43R-3, 0-5	577.97	1,070	24.2	ND	ND	0.767	33.9

ND = not detected, — = incalculable.

Table T11. Concentrations of hydrocarbon and CO<sub>2</sub> gases in the void gas, Holes U1413A and U1413B.

Core, section, interval (cm)	Depth (mbsf)	Methane (ppmv)	Ethane (ppmv)	Propane (ppmv)	CO <sub>2</sub> (ppmv)	C <sub>1</sub> /C <sub>2+</sub>
344-U1413A-						
5H-3, 50-51	38.51	837,000	4.9	0.7	6,350	149,000
6H-1, 50-51	45.10	837,000	3.9	1.8	3,610	146,000
7H-5, 50-51	58.24	841,000	4.0	4.4	4,600	99,300
7H-6, 50-51	59.70	840,000	4.0	4.4	5,540	100,000
8H-6, 50-51	68.56	831,000	4.2	5.0	5,180	90,900
9H-1, 50-51	70.50	833,000	4.2	5.0	4,840	90,400
9H-3, 50-51	73.52	833,000	3.8	4.4	4,200	100,600
10H-1, 50-51	80.00	822,000	5.0	5.9	7,680	76,000
11H-3, 50-51	92.43	792,000	4.4	4.7	506.0	87,700
13H-6, 50-51	112.59	825,000	6.9	7.2	4,720	58,700
14H-2, 50-51	115.16	830,000	6.6	5.9	1,870	65,900
15H-3, 50-51	122.13	832,000	8.7	7.6	5,740	51,100
16H-4, 50-51	128.99	828,000	9.2	6.6	3,850	52,400
18H-2, 50-51	137.62	825,000	11.5	5.6	4,410	48,100
344-U1413B-						
3H-4, 50-51	20.30	832,000	4.7	0.0	1,880	175,000

**Table T12.** Total carbon (TC), inorganic carbon (IC), total organic carbon (TOC), calcium carbonate, total nitrogen (TN), and C/N ratios, Site U1413.

Core, section, interval (cm)	Depth (mbsf)	TC (wt%)	IC (wt%)	TOC (wt%)	CaCO <sub>3</sub> (wt%)	TN (wt%)	C/N ratio
344-U1413A-							
1H-2W, 136–137	2.86	3.06	1.21	1.85	10.1	0.179	10.3
1H-4W, 107–108	5.57	2.81	1.37	1.44	11.5	0.121	11.9
2H-2W, 136–137	9.46	2.40	1.19	1.21	9.89	0.123	9.87
2H-3W, 99–101	10.59	2.36	1.07	1.29	8.89	0.109	11.9
3H-4W, 9–10	20.06	2.99	1.39	1.61	11.6	0.138	11.6
3H-7W, 2–3	24.55	2.99	1.42	1.57	11.8	0.154	10.2
4H-1W, 125–126	26.85	2.62	1.43	1.19	11.9	0.122	9.74
4H-2W, 140–141	28.43	2.62	1.47	1.16	12.2	0.125	9.24
4H-4W, 133–134	31.24	3.13	1.37	1.76	11.4	0.173	10.2
5H-2W, 132–133	37.83	3.60	1.52	2.08	12.7	0.199	10.4
5H-4W, 42–43	39.84	3.52	1.47	2.05	12.2	0.200	10.3
5H-5W, 132–133	42.15	2.77	1.62	1.15	13.5	0.128	9.00
5H-7W, 47–48	44.21	2.39	1.20	1.19	10.0	0.132	9.00
6H-2W, 135–136	46.69	2.24	1.18	1.06	9.81	0.122	8.72
6H-4W, 133–134	49.65	2.48	1.11	1.37	9.26	0.112	12.2
7H-5W, 73–74	58.47	1.84	0.866	0.974	7.22	0.114	8.55
8H-1W, 50–51	61.40	1.63	0.761	0.869	6.35	0.115	7.56
8H-2W, 129–130	63.39	2.22	0.636	1.58	5.31	0.108	14.7
8H-5W, 133–134	67.83	2.46	1.29	1.17	10.7	0.115	10.2
9H-1W, 42–43	70.42	2.59	1.36	1.23	11.3	0.112	11.0
9H-3W, 1–2	73.03	2.35	1.50	0.849	12.5	0.0910	9.33
9H-5W, 130–131	77.18	2.27	1.54	0.730	12.8	0.0990	7.38
10H-2W, 127–128	82.18	2.34	1.43	0.912	11.9	0.105	8.69
10H-4W, 57–58	84.44	2.39	1.33	1.06	11.1	0.101	10.5
10H-5W, 28–29	85.67	2.37	1.41	0.959	11.8	0.102	9.40
11H-2W, 126–127	91.68	2.13	1.22	0.913	10.2	0.100	9.13
11H-4W, 52–53	93.88	2.09	1.16	0.931	9.67	0.0940	9.90
11H-5W, 128–129	96.06	1.86	1.14	0.721	9.50	0.102	7.07
12H-1W, 27–28	98.17	1.79	0.943	0.847	7.87	0.107	7.91
12H-4W, 75–76	102.94	1.79	0.836	0.954	6.98	0.109	8.75
12H-4W, 104–105	103.23	2.02	0.804	1.22	6.70	0.0990	12.3
13H-2W, 127–128	108.28	1.90	1.22	0.682	10.2	0.0940	7.26
13H-3W, 81–82	109.34	1.76	1.10	0.656	9.21	0.0950	6.91
13H-4W, 127–128	111.22	1.81	1.15	0.662	9.58	0.0920	7.19
14H-2W, 70–72	115.36	1.45	0.984	0.466	8.21	0.0960	4.86
14H-3W, 126–127	117.33	1.53	0.969	0.561	8.09	0.0960	5.84
15H-2W, 127–128	121.38	1.58	0.618	0.962	5.16	0.0810	11.9
15H-3W, 122–123	122.85		0.637		5.31		
16H-2W, 122–123	127.03		0.784		6.54		
16H-2W, 125–126	127.06		0.669		5.58		
16H-3, 117–118	128.48		0.707		5.89		
17H-2W, 78–79	131.69		1.21		10.1		
17H-3W, 140–141	133.33		1.27		10.6		
17H-4W, 125–126	134.60		1.26		10.5		
18H-2W, 126–128	138.38		1.10		9.20		
18H-3W, 24–26	138.88		1.17		9.75		
19X-4, 95–96	145.92		1.04		8.64		
19X-6W, 75–76	148.44		1.01		8.38		
20X-4W, 64–65	154.54		0.785		6.55		
20X-6W, 107–108	157.20		0.795		6.63		
21X-3W, 123–124	164.05		0.881		7.35		
21X-5W, 113–114	166.93		1.05		8.72		
22X-1W, 54–55	170.24		0.993		8.28		
22X-2W, 93–94	171.48		1.12		9.33		
23X-1, 36–37	174.66		1.33		11.1		
24X-1W, 65–66	175.95		1.41		11.7		
24X-1W, 115–116	176.45		1.27		10.6		
24X-3W, 60–61	178.43		1.26		10.5		
25X-1, 32–33	179.72		1.11		9.22		
25X-2, 26–28	180.50		0.655		5.46		